GA-A24555

Inertial Confinement Fusion Annual Report

October 1, 2002 through September 30, 2003

Capsules — Glass and Polymer

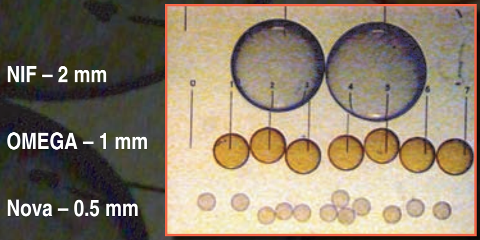

Typical Capsules

Foam Shells

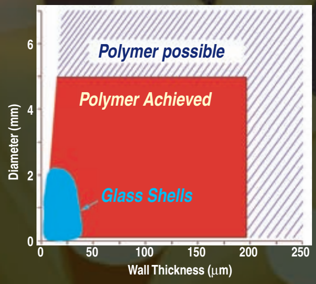

Range of Capsules

Micromachined Components

Witness Plates

NIF Cryo Hohlraum

Coatings

GDP Coater

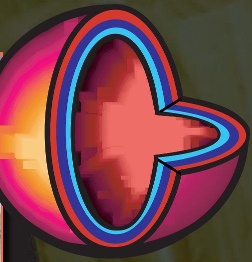

Multiple GDP (Glow Discharge Polymer) Layers Doped with Si, Ge, Ti, Cl, Cu, or D

Targets

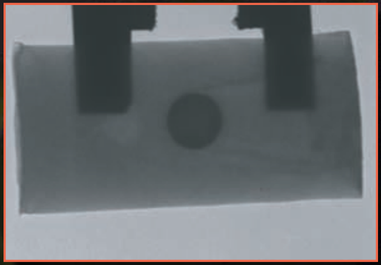

Target for Z (Radiograph of Shell Embedded in Foam)

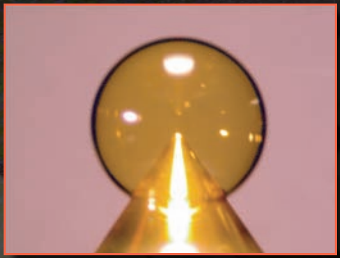

Fast Ignition Target

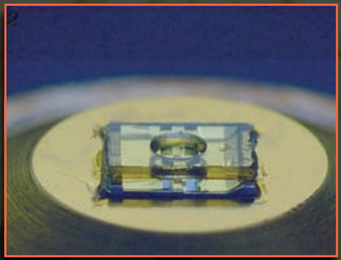

NRL EOS Target

Target Characterization

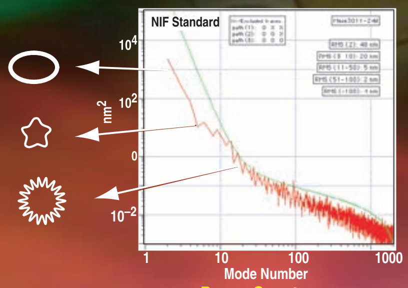

Power Spectrum

Spheremapper/Wallmapper

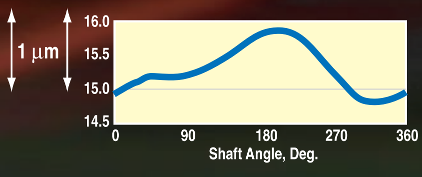

Wallmapper

Schafer

GENERAL ATOMICS

DISCLAIMER

GA–A24555

INERTIAL CONFINEMENT FUSION TARGET COMPONENT FABRICATION AND TECHNOLOGY DEVELOPMENT SUPPORT

ANNUAL REPORT TO THE U.S. DEPARTMENT OF ENERGY

OCTOBER 1, 2002 THROUGH SEPTEMBER 30, 2003

by
PROJECT STAFF

W.J. Miller, Technical Editor

Work prepared under
Department of Energy
Contract No. DE-AC03-01SF22260

GENERAL ATOMICS PROJECT 30095
DATE PUBLISHED: JULY 2005

GENERAL ATOMICS

ACRONYMS

AFM	atomic force microscope
CDR	Conceptual Design Report
CPL	cryogenic pressure loader
CTM	cryogenic target mount
CW	continuous wave
D_2TS	deuterium test system
D-GDP	deuterated polymer
DT	deuterium-tritium
DTRA	Defense Threat Reduction Agency
DVB	divinylbenzene
EDAX	energy dispersive x-ray analysis
EOS	equation of state
FI	fast ignition
GA	General Atomics
GDP	glow discharge polymer
HD	hydrogen deuteride
HEDP	high energy density plasma
ICF	Inertial Confinement Fusion
IDL™	Interactive Data Language
IFE	Inertial Fusion Energy
IFT	Inertial Fusion Technology
ILE	Institute of Laser Engineering, Japan
IPA	isopropanol
IR	infrared
LANL	Los Alamos National Laboratory
LEH	laser entrance hole
LLNL	Lawrence Livermore National Laboratory

NCTS	NIF Cryogenic Target System
NIF	National Ignition Facility
NNSA	National Nuclear Security Administration
NRL	Naval Research Laboratory
PAMS	poly(α-methylstyrene)
PCHMS	polycyclohexyl-methylsilylene $C_7H_{14}Si$
PVA	polyvinyl alcohol
RF	radio frequency
RT	Rayleigh-Taylor
SEM	scanning electron microscopy
Si-GDP	silicon-doped glow discharge polymer
SM	spheremapper
SM/WM	spheremapper/wallmapper
SNL	Sandia National Laboratory
TARPOS	TARget POSitioner
TGA	thermogravimetric analysis
TIC	target insertion cryostat
TPX	commercial designation of the polymer produced by the polymerization of 4-methylpentene-1
UR/LLE	University of Rochester/Laboratory for Laser Energetics
UV	ultraviolet
WBS	work breakdown structure
WETF	Weapons Engineering Tritium Facility
WM	wallmapper
XRF	x-ray fluorescence

TABLE OF CONTENTS

1. EXECUTIVE SUMMARY **1–1**

2. INTRODUCTION **2–1**

3. PROGRAM ACCOMPLISHMENTS **3–1**

3.1. Program Overview 3–1
3.2. Center for Advanced and Cryogenic Technology (G. Besenbruch, GA) 3–3
3.2.1. The Mark-I Cryogenic Target System (J. Stewart, R. Fraze, Schafer) 3–3
3.2.2. The Beryllium Fill Systems (N. Alexander and R. Gallix, GA) 3–5
3.3. Center for Advanced Cryogenic Layering (D. Bittner, Schafer) 3–13
3.3.1. Layering Fundamentals 3–13
3.3.2. IR Layering 3–15
3.3.3. Enhanced Cryogenic Layering 3–16
3.4. Center for Target Component Fabrication and Fabrication Development (J. Kaae, GA) 3–23
3.4.1. LLNL, LANL, SNL, and UR/LLE Deliveries 3–23
3.4.2. Fabrication of Epoxy Hohlraums 3–26
3.4.3. Fabrication of Thin-Walled Aluminum Tubes 3–27
3.4.4. Fabrication of Window Saddles for NIF Cryogenic Hohlraums 3–29
3.5. Center for Polymer and Coatings and Foam Capsule Development (A. Nikroo, GA) 3–31
3.5.1. UR/LLE Deliveries 3–32
3.5.2. Foam Shell Fabrication 3–34
3.5.3. NIF Mandrel Fabrication 3–38
3.6. Center for Foam Development and Production (D. Schroen, Schafer) 3–42
3.7. Inertial Fusion Capsule Production (D. Steinman, GA) 3–43
3.7.1. Fabrication of a New Type of Double-Shell Target with a PVA Inner Layer 3–43
3.7.2. Glass Shells from Doped GDP 3–47
3.7.3. PVA-Coating of Multimillimeter Polymer ICF Capsules 3–48
3.8. Advanced Planar Targets (T. Walsh, Schafer) 3–51
3.8.1. NRL and UR/LLE Deliveries 3–52
3.8.2. Flat CH Films 3–52

3.8.3. Patterned CH Films 3–54
3.8.4. Coatings 3–55
3.8.5. NRL Foams 3–57
3.8.6. NIKE EOS Targets 3–58
3.8.7. Characterization 3–59
3.9. GA/Schafer Characterization Innovation and Development Office (R. Stephens, GA) 3–62
3.9.1. Data Logging for Production Control 3–62
3.9.2. Spheremapper Coverage Improvement 3–62
3.9.3. Spheremapper Noise Reduction 3–65
3.9.4. Automicroscope Capability 3–66
3.10. Operations Office for Schafer Division of Inertial Fusion Technology (K. Shillito, Schafer) 3–69
3.10.1. On-Site Support at LANL 3–69
3.10.2. On-Site Support at SNL 3–71
3.10.3. Aerogel Technology Transfer to LANL 3–72
3.11. Operations (W. Miller, GA) 3–73
3.11.1. On-Site Support at LLNL (W. Miller; writing contributed by J. Ruppe) 3–73

4. PUBLICATIONS 4–1

5. ACKNOWLEDGMENT 5–1

LIST OF FIGURES

3–1. GA/Schafer organizational chart 3–2
3–2. The Mark-I cryostat was redesigned around a cryocooler 3–4
3–3. This prototype test setup was designed to test cryocooler performance 3–5
3–4. This test setup is designed to test vibration 3–6
3–5. Low-pressure cryocondensation concept 3–7
3–6. Cryocondensation cell design concept 3–8
3–7. Assembly sequence of the cryocondensation cell 3–8
3–8. Laser sealing scheme 3–10
3–9. Filling and bonding cell 3–11
3–10. Two views of a typical cylinder pair 3–11

3–11. Bonding cell component temperatures 3–12

3–12. Radial distribution of temperature from the cell axis to the vessel o.d. 3–12

3–13. Shadowgraph of a 125 μm layer inside of a 2 mm diameter 40 μm thick polymer capsule 3–14

3–14. Shadowgraph images of a layer where (a) is a uniform 50 μm thick HD layer formed near the triple point and (b) is the same layer cooled to 1.5 K 3–16

3–15. Drawing of a NIF-scale hohlraum with six optical fibers attached 3–17

3–16. Cut-away drawing of the vacuum can showing the NIF-scale hohlraum inside 3–17

3–17. Picture of a roughened hohlraum in the copper support 3–17

3–18. View of the hohlraum through one of the windows in the vacuum can 3–17

3–19. Component layout for splitting the laser output into six beams 3–18

3–20. Three images showing the slow layer degradation occurring during a slow cooldown at ~4 Q_{DT} 3–20

3–21. Power spectral plots 3–20

3–22. Raytrace diagram of a parallel ray through the shell and ice layer 3–20

3–23. Shadowgraph radial lineouts for both a collimated source and a diffuse source raytrace through a 2 mm o.d. by 1.92 mm i.d. shell containing a 100 μm ice layer 3–21

3–24. Shadowgraph radial lineouts for both a collimated source and a diffuse source raytrace 3–22

3–25. Raytrace model lineout showing the reduction in “background” rays by using a pinhole in an image collection system 3–22

3–26. Hohlraum with 25 μm wall 3–23

3–27. Copper hohlraum mandrel 3–23

3–28. One-half of a cryogenic hohlraum 3–24

3–29. Square cylinder with copper leached out 3–24

3–30. Half-round cylinder with gold leached out 3–24

3–31. A small gold truncated cone 3–24

3–32. A set of gold cups in varying sizes 3–25

3–33. A disk with a precisely defined thickness and diameter 3–25

3–34. A gold cylinder with a conical flange on one end 3–25

3–35. A gold disk with tabs produced for SNL 3–26

3–36. A gold trapezoidal shield 3–26

3–37. An epoxy hohlraum 3–27

3–38. The copper mandrel and holder used for making epoxy hohlraums 3–27
3–39. The first shaping step on the copper mandrel 3–27
3–40. Machining of the barrel of the holder for centering of the component 3–27
3–41. Machining of a face on a holder to obtain an axial reference position 3–28
3–42. Shaping the front of a copper mandrel 3–28
3–43. Drawing of foil tube with dimensions 3–28
3–44. An acrylic mandrel 3–28
3–45. The acrylic mandrel in a sputtering chamber 3–28
3–46. A defective aluminum coating showing wrinkles and cracks 3–29
3–47. An acrylic mandrel with a successful aluminum coating 3–29
3–48. An aluminum coated mandrel after the final machining step 3–29
3–49. A completed aluminum foil tube 3–29
3–50. CAD rendering of a window saddle 3–30
3–51. Segments that make up the window saddle mandrel 3–30
3–52. Window saddle mandrel assembly 3–30
3–53. A photograph of the window saddle copper mandrel 3–30
3–54. The electroformed window saddle 3–30
3–55. New GDP coater and new sputter coater assembled using EQU-03 tasks 3–32
3–56. Summary of capsule deliveries to UR/LLE in FY03 3–33
3–57. Depolymerizable mandrel technique is used extensively in capsule fabrication for LLE 3–34
3–58. A new inventory of PAMS shells was fabricated in FY03 for the new UR/LLE diameter size of ~860 μm 3–35
3–59. Diameter shrinkage of GDP-coated PAMS shells during the pyrolysis step in the depolymerizable mandrel process 3–35
3–60. Histograms of the wall concentricity of four different batches of low density foam shells 3–36
3–61. Argon permeation out of ~3 to 4 μm thick GDP coated RF foam shells 3–37
3–62. PVP coated RF foam shells shrink by as much as 20% 3–37
3–63. Intact high density RF shells with a soccer ball-like surface 3–38
3–64. View of a planar cryogenic target cell filled with RF foam 3–38
3–65. A sample of 19 AFM power spectra of shells 3–40
3–66. The left radiograph is the length view of the foam with shim and capsule 3–42

3–67. This SEM micrograph shows the gold nanopowder 3–42

3–68. The foam in this SEM is composed of an organometallic Si dopant coating the TPX foam structure 3–42

3–69. Double-shell target containing an inner lining of PVA 3–44

3–70. GDP/PVA/PAMS shells were held in place with hardened Aunt Jemima® syrup on a coverslip 3–45

3–71. Process used for removing the PAMS mandrel from the final GDP/PVA shell and freeing it from the glass coverslip 3–46

3–72. LLNL fabricated numerous 250 μm disks 3–46

3–73. Double-shell target containing an inner lining of PVA 3–47

3–74. The Hoppe glass shell Parr oven is designed to operate at up to 1100°C 3–48

3–75. Droplet of PVA resulting from the original spin-coating technique 3–48

3–76. The capsule is mounted on a piece of Post-it® sticky paper 3–49

3–77. The capsules are lined up on a Post-it® note affixed to a flat glass block 3–50

3–78. FY03 target mix 3–52

3–79. Nike target frame with gold-coated polymer film target 3–53

3–80. Aluminum CTMs have a film of 1.5 μm thick Schafer-made polyimide stretched over them and sealed 3–53

3–81. For an NRL experiment, the ridges on a patterned polystyrene film had to be mounted parallel to the edges of the Nike target holder 3–54

3–82. March Instruments PX 250 Plasma Asher 3–54

3–83. This filament-heated crucible is part of a salt coater 3–55

3–84. The evaporative coater is used primarily for aluminum or gold coatings with thickness greater than 1000 Å 3–56

3–85. Sputter coating facility at Schafer 3–56

3–86. Rippled surface on RF foam 3–57

3–87. This SEM micrograph shows the cell size and structure of DVB foam 3–58

3–88. This AFM trace of a DVB foam cast at 70 mg/cm^3 shows an average feature size of approximately 1.5 to 2.5 μm 3–58

3–89. A new type of EOS target for NRL 3–58

3–90. Glass cover slip with a hole drilled in the center supports the aluminum witness stripes 3–58

3–91. EOS target consisting of a five-level aluminum plate 3–59

3–92. By positioning the fringes from this white light interferometer, focus position and therefore film thickness can be measured precisely 3–60

3–93. Our Veeco RST–500 scanning surface profilometer is used to measure the surface of complex objects 3–60
3–94. The scanning surface profilometer measures the heights of points over a surface and reports the data in a variety of formats 3–61
3–95. Vibration isolation system 3–61
3–96. A Nike target is examined by imaging transmitted UV light 3–61
3–97. Probability of detecting a single lump versus the mode number of that lump for two different trace patterns 3–63
3–98. New control arrangement for spheremapper 3–63
3–99. Surface profile with low (<5) modes eliminated 3–64
3–100. Set of complete coverage profiles combined into bands and wrapped around a sphere and merged into a continuous surface 3–64
3–101. Three consecutive noise tests 3–65
3–102. Digital Instruments’ in-house reference noise spectrum 3–66
3–103. The Trident laser can launch 1-D flyer plates of various thickness and velocity 3–70
3–104. Trident experiments will use laser-launched flyer plates to collect spall data .. 3–70
3–105. A typical EOS panel assembled in FY01 3–71
3–106. An example of an alignment aid target for initial NIF shots 3–73
3–107. The difference in size is here demonstrated between a NIF-sized gas pipe target and two standard-sized OMEGA targets 3–74
3–108. A gas pipe target is a transparent epoxy hohlraum with thin polyimide windows 3–74
3–109. A target from FY02 3–75
3–110. The dislodged-in-shipping inner shell of this assembly is repaired 3–76
3–111. The formvar-tented capsule 3–77
3–112. The disassembled components of a “core-imaging” target 3–77
3–113. The counterclockwise rotation of the pinhole array with an LEH view 3–78
3–114. A reverse-scalloping border has been machined into the LEH pinhole array’s plastic holder 3–78
3–115. A “hot hohlraum” target rejected for the dent in its top surface 3–78
3–116. A side and a top view of the most recent target 3–79
3–117. Top and side views of a plastic hohlraum 3–79
3–118. Top and side views of foam-jet target 3–80

LIST OF TABLES

3–1. Summary of spheremap results using pre-baked PAMS shells 3–39
3–2. Total number of targets shipped 3–52
3–3. List of the patterned substrates currently available at Schafer for casting 3–56
3–4. Repeatability of measurements for NIF, OMEGA, and Nova shell sizes 3–67

1. EXECUTIVE SUMMARY

This report documents fiscal year 2003 activity on the U.S. Department of Energy (DOE) National Nuclear Security Administration (NNSA) task order contract for Inertial Confinement Fusion (ICF) Target Component Fabrication and Technology Development Support with General Atomics (GA) and partner/subcontractor Schafer Corporation. Work performed spans development, production, and engineering of planar and spherical targets, target components, and cryogenic systems for the NNSA ICF Laboratories: Lawrence Livermore National Laboratory; Los Alamos National Laboratory; Sandia National Laboratory; the University of Rochester Laboratory for Laser Energetics; and the Naval Research Laboratory in Washington, D.C.

For more than ten years, the GA/Schafer Inertial Confinement Technology team has partnered with the NNSA ICF Laboratories developing and providing targets and related technologies for ongoing and future driver target interaction laboratory experiments. The team expertise is broad with interests and capabilities in all of the relevant areas of polymer and metal component fabrication, gas filling (including tritium), machining, characterization, and handling as diagrammed in Fig. 1–1.

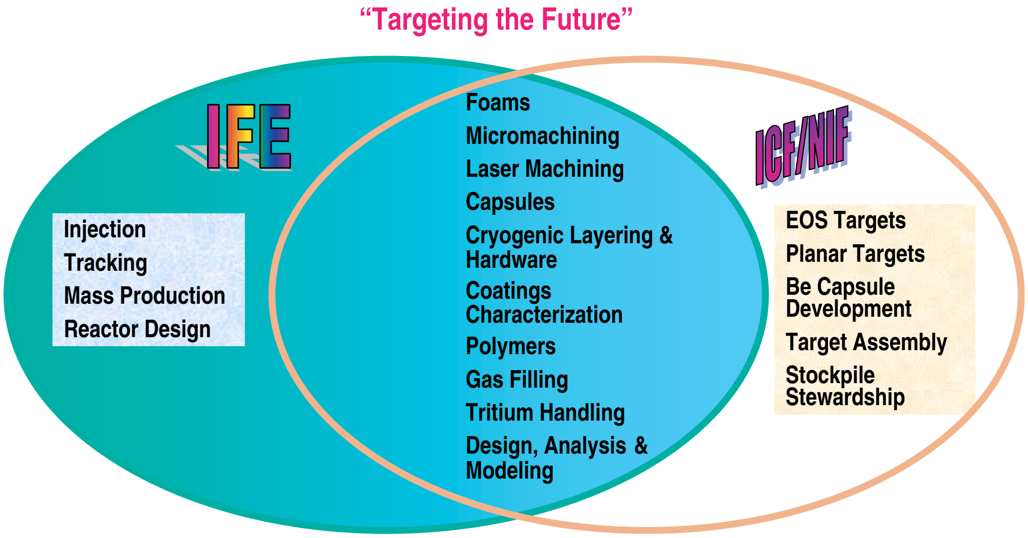

Fig. 1–1. The GA/Schafer Inertial Confinement Technology team expertise supports the NNSA national security missions as well as derivative missions such as Inertial Fusion Energy.

Highlights of the GA/Schafer ICF technology work performed under DOE Contract No. DE-AC03-01SF22260 in FY03 comprise the subject of this report. Comments and requests for further information may be directed to the GA Inertial Fusion Technology Program Manager, Joe.Kilkenny@gat.com, (858) 455–3571.

2. INTRODUCTION

Inertial Confinement Fusion (ICF) is a research and development activity supported under the auspices of the U.S. Department of Energy (DOE) National Nuclear Security Administration (NNSA). The goal of ICF research is controlled laboratory implosion of fusionable material to a condition of ignition and propagating burn.

ICF relies on inertia to confine fusionable material, usually a mixture of deuterium and tritium (DT), for the time required to create a fusion reaction. Matter, which reaches this inertially confined state by means of compression from lasers or x-rays, can be considered to be a high energy density plasma (HEDP) for essentially all phases of the process from earliest compression through energy production through replete, extinguishing burn.

The canonical implosion scenario is that of central hot spot ignition in which a hollow, impermeable DT sphere is symmetrically imploded to a density (ρ), radius (R) product of 0.3 g/cc and a temperature (T) of order 10 keV. In the limit of radial symmetry, success (propagating burn) is predicted for a wide range of driver-capsule configurations.

The two most commonly envisioned central hot spot systems are direct and indirect drive ICF. In direct drive, the driving beams, usually high intensity lasers (a few × 10^{14} W/cm^2) of short wavelength light (0.33 to 0.25 μm) directly irradiate a spherical capsule surface. As the surface is heated, matter boils off and the capsule implodes. For shaped pulse driving beams, in which the intensity is controlled so as to drive well-timed shocks in the shell and accelerate the compressed hollow sphere walls inward to high final velocities (3×10^7 cm/s), a design space has been found where fusion conditions are predicted to occur. For indirect drive, the process is similar, with laser light replaced by a spatially uniform bath of x-rays (wavelength ~0.1 μm). The x-rays are produced and contained in a spherical or cylindrical can, a hohlraum, that is fabricated of metals of high atomic number. NNSA drivers used to generate the hohlraum x-rays include lasers and z-pinches.

It is generally agreed that five criteria determine a successful ICF implosion, each with outstanding issues and active research. First, a sufficient amount of driver energy must be transferred to the shell. Plasma instabilities in the shell corona can inhibit successful coupling of driver energy into the target. This continues to be an area of ongoing research with regimes identified that minimize plasma instabilities and allow for up to 80% driver energy absorption. Second, the capsule must be imploded on a sufficiently low adiabat for fusion conditions to be achievable with laboratory-scale drivers. Adverse preheat mechanisms include shock mistimings (5% or greater), radiation effects, and mixing from very short wavelength instabilities. Considerable research in equation of state and opacity results from this criterion. Third, the implosion must be sufficiently symmetric at length scales long relative to the shell thicknesses for the generation of a well-formed hot spot. This criterion, which sets a shell uniformity requirement of a few percent and also limits time independent drive asymmetry at long perturbation wavelengths ($l < 32$) to a few percent, is achievable with existing technologies. Fourth, the shell must be sufficiently stable to the short wavelength Rayleigh-Taylor (RT) instability to confine the core gas to full implosion in order for ignition conditions to be achieved. This instability, which is seeded by all of the small-scale imperfections of real-world driving beams and shell surface and mass, is the subject of intense ongoing research. Because the RT instability is vortical in nature, mitigation is sought primarily in a tailoring of the ICF pellet gradients to reduce the vorticity source term (a function of the cross product of gradients of ρ and T) at both the outer and inner shell surfaces and to increasing the ablation velocity at the shell surfaces in order to pull away as much as possible the vorticity generated. Fifth, the pellet must reach a condition of sufficient ρR and T for alpha-particle-driven ignition and propagating burn to occur.

As with many systems with well-defined postulates, the relaxation of one criterion can sometimes lead to the most interesting alternate systems. A classic example is the birth of complex variable theory which came about when parallel lines were allowed to meet at infinity in an otherwise Euclidean space. In the case of ICF, relaxing completely the fourth criterion has led to the idea of fast ignition (FI). In FI, the ρR for ignition is first achieved with standard drivers and capsules that range from spherical shells to hemispheres of webbed foams. The ignition beam is then envisioned to be generated from high intensity, collimated electrons or ions that result from petawatt laser matter interaction. While compression is relatively easy and has, to some level, already been demonstrated in the laboratory, coupling the ignitor “match” to the compressed fuel is far from determined. The introduction of this concept in the early 1990s, along with the development of very high intensity (order 10^{18} W/cm^2 or higher) laser drivers, has resulted in significant active research in very high intensity laser matter and laser plasma interactions.

The GA/Schafer team fabricates components and complete target assemblies for the NNSA ICF laboratories (Lawrence Livermore National Laboratory, Los Alamos National Laboratory, Sandia National Laboratory, the University of Rochester Laboratory for Laser Energetics, and the Naval Research Laboratory) to address a wide range of experimental criteria that are relevant to ICF and HEDP physics. These components include: gasbags for plasma instability studies, doped planar and shaped targets for radiation preheat and shock timing investigations, well-characterized spheres with a variety of gas fills for low-mode asymmetry studies under a range of conditions, targets that enable investigation of the Richtmyer-Meshkov and RT instabilities, and we are assisting in the development of National Ignition Facility ignition targets and cryogenic systems.

The work of target and target component fabrication is fundamentally cross-disciplinary in nature. Most new target types and developments are research results from proactive teams of chemists, material scientists, physicists, and characterization and fabrication engineers, who, together, produce new target systems and capabilities.

3. PROGRAM ACCOMPLISHMENTS

3.1. PROGRAM OVERVIEW

Under the U.S. Department of Energy (DOE) National Nuclear Security Administration (NNSA) Inertial Confinement Fusion (ICF) Target Component Fabrication and Technology Development Support contract, General Atomics (GA) and its partner/subcontractor Schafer Corporation are responsible for NNSA target and target component fabrication and production as well as design, development, and fielding of associated technologies that range from large-scale cryogenic systems to precision hohlraum assembly stations. GA/Schafer supplies components to the five ICF laboratories: Lawrence Livermore National Laboratory (LLNL), Los Alamos National Laboratory (LANL), Sandia National Laboratory (SNL), the University of Rochester Laboratory for Laser Energetics (UR/LLE), and the Naval Research Laboratory (NRL). In order to continue to meet the needs of the developing NNSA ICF program, the GA/Schafer team is structured as a capabilities-based organization under the direction of the GA/Schafer team Program Manager, Joe Kilkenny, with Keith Shillito, Associate Program Manager for Schafer Activities and Gottfried Besenbruch, Associate Program Manager for GA Activities. This organization is comprised of ten centers with contract task responsibilities divided among the centers as appropriate: the Center for Advanced Cryogenic Layering, headed by Donald Bittner; the Center for Foam Target Development and Production, headed by Diana Schroen; the Center for Advanced Planar Targets, headed by Tom Walsh; the Operations Office, headed by Wayne Miller; the GA/Schafer Characterization Innovation and Development Office, headed by Richard Stephens; the GA/Schafer Supercenter for High Energy Density Plasma (HEDP) Targets, headed by Dan Goodin; the Center for Advanced Cryogenic Technology, headed by Gottfried Besenbruch; the Center for Target Component Fabrication and Fabrication Development, headed by James Kaae; the Center for Polymer and Coatings and Foam Capsule Development, headed by Abbas Nikroo; and the Center for Capsule Production, headed by David Steinman. The organizational chart in Fig. 3–1 provides contact information.

Highlights of some of this year’s GA/Schafer Inertial Fusion Technology (IFT) accomplishments include: fabrication of foam shells for use on experiments on OMEGA, confinement of noble diagnostic gasses inside glass shells, fabrication of large diameter thin-walled aluminum hohlraums, deposition of tungsten metal on glass shells for novel HEDP targets, updating of the design concept of the target insertion cryostat for the National Ignition Facility (NIF) cryogenic target system for a rear loading cryogenic target positioner, and a vibration analysis of the clamshell shroud opening of Mark-I NIF cryostat. These and other IFT program accomplishments reported in the sections following are detailed as task activities from the perspectives of the GA/Schafer team capabilities structure.

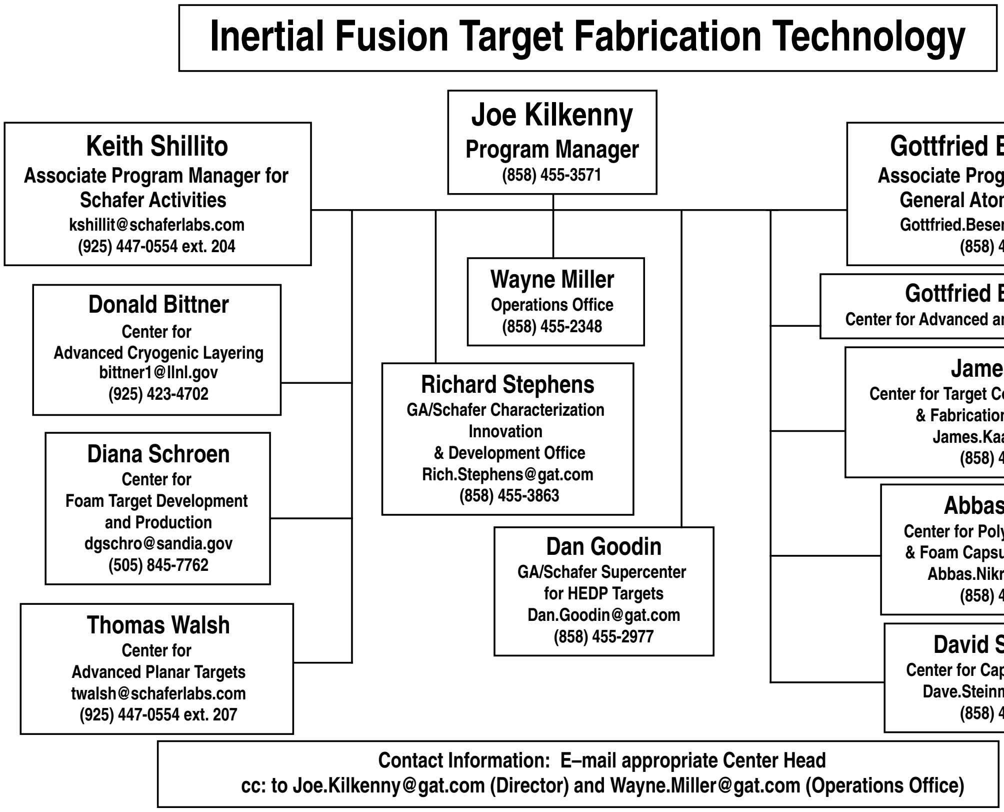

Fig. 3–1. GA/Schafer organizational chart.

Among the program accomplishments for this year are:

- Development of a Mark I cryogenic system (Section 3.2).
- Injection of infrared hohlraum cryogenic targets to enhance β layer (Section 3.3).
- Production and delivery of ~1400 ICF target components (Section 3.4).
- Delivery of gas retentive fast ignition targets for OMEGA. Production and delivery of 100 mg/cm^3 foam shells with relatively high yield, a high yield of GDP mandrels with a surface finish close to the NIF smoothness requirements (Section 3.5).
- Produce ~130 highly precise foams to fit targets for Z (Section 3.6).
- Production and delivery of 2400 characterized and target quality capsules (Section 3.7).
- Production and characteristics of 500 planar and configured targets for direct drive experiments (Section 3.8).
- Focus on automating process control and characterization (Section 3.9).
- On-site support at LANL, LLNL and SNL (Sections 3.10).

3.2. CENTER FOR ADVANCED AND CRYOGENIC TECHNOLOGY

Center Head: Gottfried Besenbruch

Scientists and Engineers: Neil Alexander, Rémy Gallix, and Chuck Gibson (GA)

Designers: Tom Drake (GA); Jerry Stewart, and Bud Fraze (Schafer)

Technician: Bob Stemke (GA)

Overview

The Center for Advanced and Cryogenic Technology focuses on the design, assembly, and testing of cryogenic target systems for ICF, Inertial Fusion Energy (IFE), and Z-Pinch. We are an integral part of the design team for the NIF Cryogenic Target System (NCTS). The NCTS is the system that fills ignition targets with deuterium-tritium (DT) or other fuels, cools the targets to cryogenic temperatures, layers the fuel in the targets, inserts the targets into the NIF target chamber, and exposes the target just before it is shot by the NIF lasers. The NCTS is being designed to deliver direct and indirect drive ignition targets using capsules made from polymers or beryllium alloys. Another cryogenic target system is being developed for the NIF, the Mark-I Cryogenic Target System. This is a system for delivery of nonignition cryogenic targets to NIF target chamber. This year, funding for the NCTS and the Mark-I was scaled back. The GA/Schafer team worked on the Mark-I and on DT fill systems for beryllium capsules for the NCTS.

3.2.1. The Mark-I Cryogenic Target System (Jerry Stewart, Bud Fraze, Schafer)

From the first NIF shots, the Mark-I Cryosystem will allow the fielding of a wide range of nonignition targets on the NIF. These include hohlraums, gas bags, planar targets, and equation of state (EOS) targets. The Mark-I will be capable of controlling the target attachment point temperature between ~8 K and 300 K and of filling targets with up to three different gasses. It will also be capable of filling and fielding DT targets. The Mark-I Cryosystem is designed to minimize operational complexity. It will attach to the Target Positioner (TARPOS) mounted on the NIF target chamber.

3.2.1.1. Design of the Mark-I Cryosystem. The Mark-I cryostat was completely redesigned this year. The new design is based around a small cryocooler (ARS DE-204S) rather than the flow cryostat and liquid helium tank of the previous design. This was done to reduce the cost of the system. It was made possible be relaxing the requirements on the system. In particular, the minimum base temperature was raised to ~8 K, and the cycle time between shots was increased. This made possible the switch to a cryocooler based system. An initial baseline design, based on the cryocooler, was modeled in CAD and a number of fabrication drawings produced. LLNL procured a number of Mark-I parts, particularly in the front end (target end) and shroud areas, for prototype testing.

The Mark-I design still utilizes the clamshell shrouds to protect the target from condensation and thermal radiation (Fig. 3–2). The liquid helium tank has been replaced by a space-frame. The pneumatic pistons have been replaced by linear electric motors. This was made possible by the space-frame, which allows for more space for other components than was possible with the liquid helium tank.

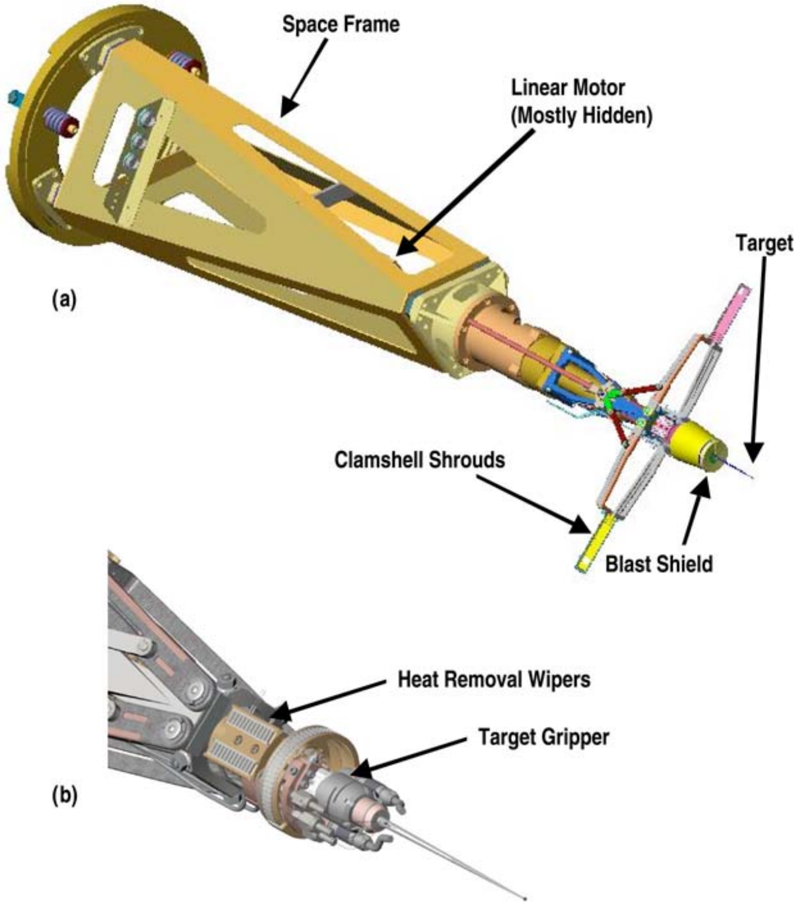

Fig. 3–2. The Mark-I cryostat was redesigned around a cryocooler. (a) Shows the whole cryostat with the shrouds half open. (b) Shows a detail at the tip of the cryostat with the shrouds fully opened and the blast shield removed.

3.2.1.2. Prototype Testing Design for Mark-I Cryosystem. Two prototype testing setups were designed, modeled in CAD, and fabrication drawings made. One was a thermal prototype test setup. The other was a setup to test the clamshell shroud opening mechanism. Additionally, fabrication drawings were produced from last year's CAD models for a prototype test setup to test the performance of a flow cryostat. These parts were not fabricated due to the switch in concept to a cryocooler.

The thermal prototype setup was designed to test the thermal capacity of the cryocooler, the vibration levels of the cryocooler, and to test the thermal performance of the target gripper. The design is shown in Fig. 3–3. LLNL procured and assembled the test setup from the fabrication drawings that we produced. They found that the cryocooler, an ARS DE-204S, had sufficient thermal capacity for the Mark-I. They also found that the tip of the cold assembly returned to a repeatable position when the cryocooler compressor was turned off.

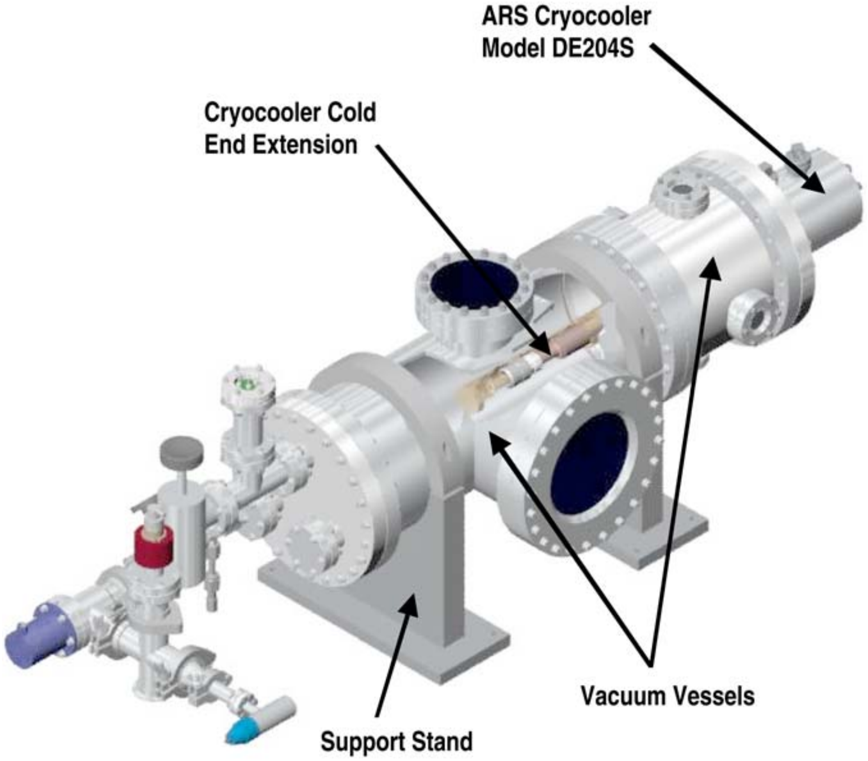

Fig. 3–3. This prototype test setup was designed to test cryocooler performance.

The shroud prototype set was designed to test the thermal efficiency of shroud cooldown. The design is shown in Fig. 3–4. The shroud arms are made with a composite structure. There is a metal layer on the inside for thermal conduction, and the outer layer is light-weight G-10 fiberglass to reduce retraction forces. Heat is removed from the shroud through louvered spring wipers. The effectiveness of the wipers and the design of the shroud need to be verified. The test setup was also designed to examine the vibrations that are induced by opening the clamshell shrouds to expose the target. Parts are being procured and assembled from the fabrication drawings produced.

3.2.2. The Beryllium Fill Systems (Neil Alexander and Rémy Gallix, GA)

To facilitate ignition target fielding, a hollow, spherical, beryllium-alloy capsule is desired that is strong enough to contain high-pressure DT gas at ambient conditions. The capsule could then be assembled into a hohlraum and placed into the Target Insertion Cryostat at room temperature. This would eliminate the complexity of permeation filling capsules inside the hohlraum and cryogenically transferring them to the Target Insertion Cryostat.

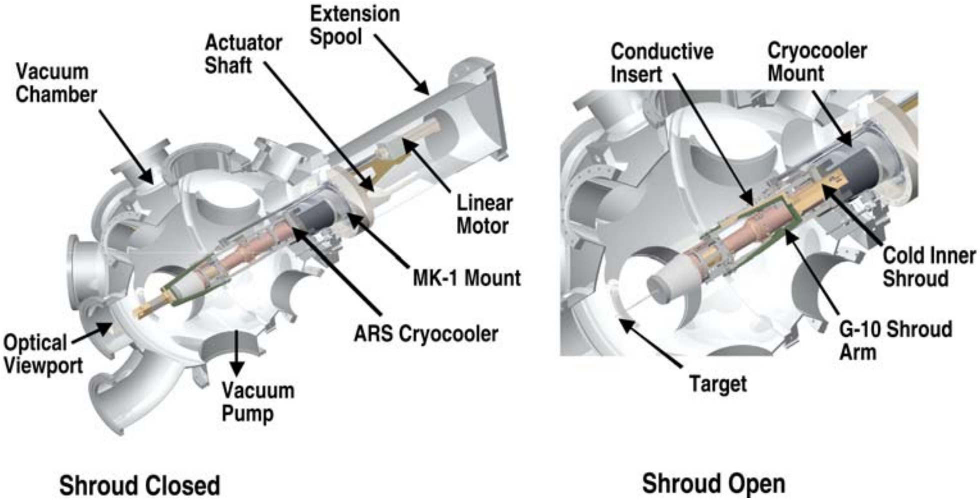

Fig. 3–4. This test setup is designed to test vibration induced from shroud opening and the thermal and mechanical performance of the clamshell shrouds.

Two principal approaches are being investigated to produce such capsules. In the first approach, a small hole is drilled through the wall of a spherical capsule, the capsule is filled with DT through the hole, and the hole is sealed, trapping the DT. In the second approach, two Be-alloy cylinders, each with a hemispherical cavity, are placed in a vessel and then filled with pressurized DT gas; they are pressed and bonded together at elevated temperatures to form a single cylinder containing a spherical cavity filled with high-pressure DT gas. After removal from the vessel, the outer surface of the cylinder is machined into the desired spherical shape.

During this fiscal year, GA has continued to develop the designs for the fill equipment for both approaches.

3.2.2.1. Drilled and Sealed Capsules. GA proposed an improved concept for filling a capsule by cryocondensation of DT gas at low pressure in a small filling chamber, then laser-sealing the fill hole at the top of the capsule through a window in the chamber as illustrated in Fig. 3–5.

A "funnel" and the capsule, sealed with vacuum grease, separate the chamber into a vacuum space and a DT space. This minimizes the volume of DT and prevents DT from condensing on the cryocooler. A commercial cryocooler and a small local heater impose a thermal gradient between the top and the bottom of the capsule to condense the gas at the bottom of the capsule and keep the fill hole clear of condensate. Using a fill pressure between 200 and 300 Torr allows rapid filling of the capsule through the fill hole. While the gas condenses in the bottom half of the capsule, the room, cell, and capsule temperatures are controlled and maintained constant, and the dropping DT pressure is monitored. The DT fill of the capsule is determined from ΔPVT measurement of the DT space. With a total DT volume of 10 cm^3, the DT fill can be determined with 1% accuracy by (1) limiting the volume of DT gas with unknown density at the tip of the "funnel" to ~<5.2 mm^3,

(2) maintaining the ambient temperature stable to ±1 K, and (3) using a high-accuracy pressure gauge (accurate to 0.15% of 10 psia full scale). If the volume of the region with unknown DT density exceeds 5.2 mm^3, a thermal model of this region may be used to correct the ΔPVT measurements. In the current conceptual design, the volume of the DT space inside the cell is only ~2.8 cm^3, leaving ~7.2 cm^3 available for the pressure gauge and the supply line, up to the shut off valve. The commercially available Heise gauge offers 0.02% accuracy, with a 4 cm^3 volume.

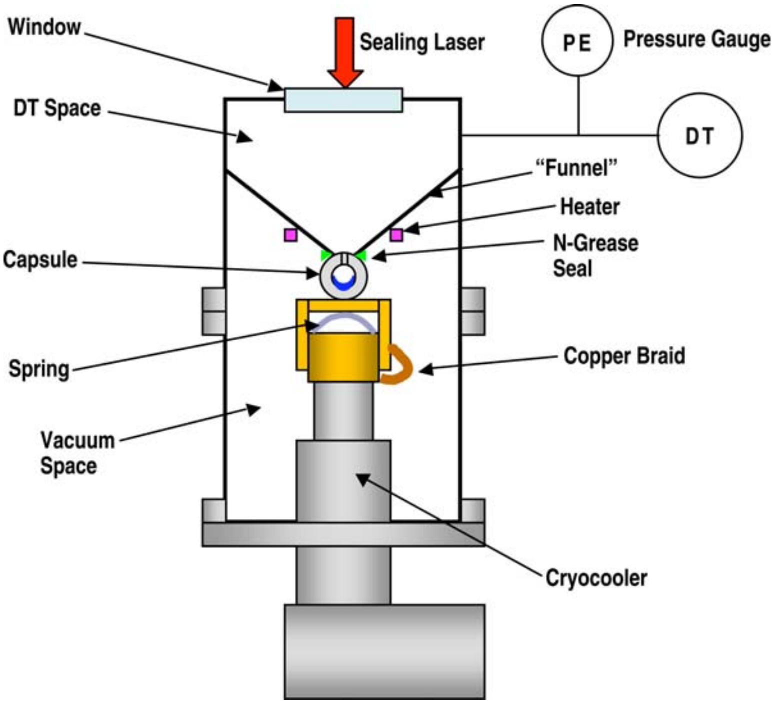

Fig. 3–5. Low-pressure cryocondensation concept.

As reported last year in General Atomics Report GA–A24147, finite-element analyses indicated the thermal feasibility of filling a capsule by cryocondensation, then sealing the fill hole with a laser. A steady-state thermal analysis showed that the temperature distribution needed for filling a beryllium capsule by cryocondensation can be achieved. A cryocooler is used to impose a temperature of 16 K at the bottom of the capsule. By applying a small heat rate (~74 mW) on the area surrounding the fill hole, the temperature of the hole can be maintained above ~34 K, keeping it clear of liquid DT; meanwhile, the bottom half of the capsule stays below ~23 K, ensuring condensation. A transient thermal analysis showed that commercially available, continuous wave (CW) or short-pulse YAG laser could be used to seal the fill hole with a plug of fused beryllium long enough to resist, with a very large margin of safety, the anticipated internal DT pressure of 400 atm at room temperature. No significant heating and vaporizing of the DT condensed at the bottom of the capsule would occur. Initial YAG laser experiments performed by LLNL in FY03 on 125 μm-thick beryllium foils achieved localized melting in accordance with GA's analytical predictions, as presented at the 15th Target Fabrication Specialist Meeting.

An initial design concept for the cryocondensing cell was produced and presented by GA in a poster at the same meeting. The concept was later refined and simplified, leading to the version shown in Fig. 3–6. It features a face seal for easier handling, a radiation shield extension anchored to the first stage of the cryocooler for more efficient cooling, copper springs that provide both heat conduction and contact pressure, a glass "funnel" to minimize

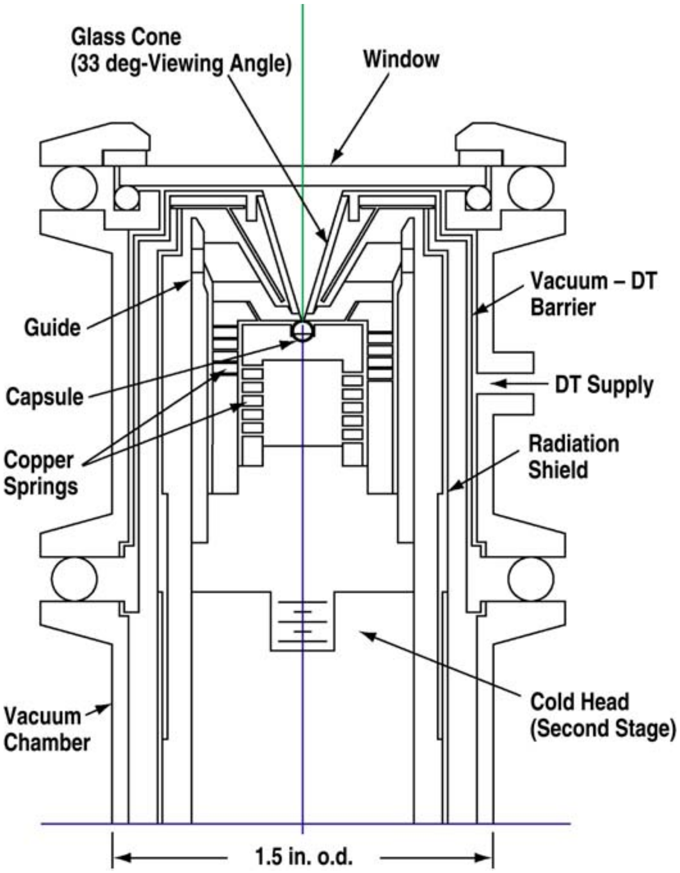

Fig. 3–6. Cryocondensation cell design concept.

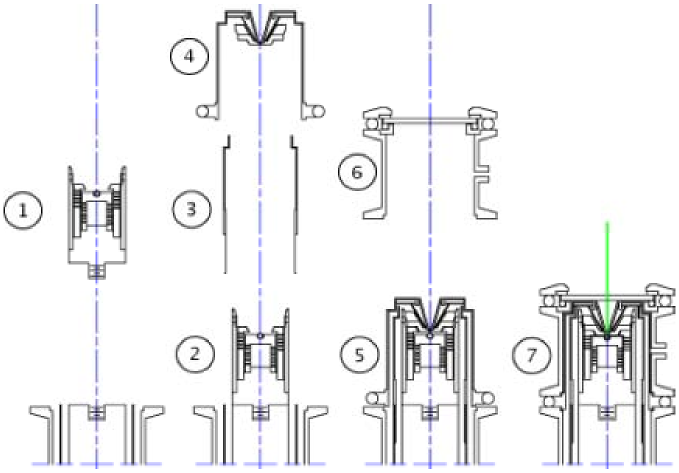

Fig. 3–7. Assembly sequence of the cryocondensation cell.

the heat leak to the capsule, and a minimized volume of DT gas in the fill chamber for better fill accuracy.

The proposed cell assembly sequence is illustrated in Fig. 3–7. The filling and sealing process is summarized below.

The capsule holder is composed of two nested, machined, copper springs and a guide tube mounted on a threaded copper base. The undrilled capsule is placed on top of the inner spring, in a cupped recess coated with a thin layer of vacuum (“N”) grease that holds it in place and improves thermal contact during cryocondensing. The capsule on its holder can then be placed in the laser-drilling chamber and the filling hole can be drilled through the top of the capsule. Alternatively, the already laser-drilled capsule can be placed on top of the greased holder, with the hole on axis at the top.

The capsule holder (1) is then screwed into the top of the second stage of a cryocooler fitted with a closely fitting vacuum chamber, and a radiation shield mounted on the first stage (2). The commercially available cryocooler with the smallest cold head diameter (CCS-100/202 by JANIS Research Co. or DE-202 by Advanced Research System) is selected to minimize the DT volume in the cell. An extension (3) is added to the radiation shield. Next, a ring of vacuum grease is placed around the hole at the bottom of the funnel assembly. The funnel assembly (4) is then lowered over the capsule holder until it rests on top of the capsule (5). The shield extension and the capsule holder guide the funnel assembly and center the funnel opening over the capsule hole. Finally, the window assembly (6) is slipped over the funnel assembly and clamped to the top flange of the cryocooler vacuum chamber, slightly compressing both copper springs and sealing the chamber (7).

The forces applied by the springs improve both the seal between the top of the capsule and the bottom of the funnel assembly; and the thermal contacts between the capsule, the capsule holder, and the funnel assembly. Under 3.7 N compression, the shear, bending, and bearing stresses calculated in the capsule are respectively 15, 19, and 5 MPa, much lower than the 200 MPa tensile strength at RT estimated from bursting tests of sputtered beryllium capsules.

The window assembly is then connected to the vacuum and DT-supply systems. To fill the capsule, the cryocooler vacuum chamber, as well as the space above the capsule and the inside of the capsule, are first evacuated in parallel. The total volume of the space in and above the capsule, in the short DT supply line, and in the high-accuracy pressure gauge, estimated to be ~10 cm^3, will have been previously measured. This space is now filled with DT at RT and valved off. The cryocooler may be turned on before or after the space is filled with DT gas. This optimization of the filling procedure is still being developed. Miniature local electric heaters and temperature sensors mounted in the capsule holder and the funnel assembly are used to bring the capsule temperature to ~16 K at the bottom and ~35 K at the top. This thermal gradient is maintained to condense the gas at the bottom of the capsule and keep the fill hole clear of condensate.

Preliminary, one-dimensional calculations were performed to verify the thermal feasibility of the conceptual design of the cryocondensing cell. Conservative assumptions were made on temperature distributions and temperature-dependent thermal properties were used through the CRYOCOMP program. The following heat leaks were obtained: ~0.6 W to the first stage at 45 K and ~0.3 W to the second stage at 14.7 K. These heat loads are well within the capacity of the selected cryocooler: 4 W at 45 K on the first stage with 1.2 W at 14.7 K on the second stage.

Preliminary concepts to conveniently find the hole and focus the sealing laser on it have been considered. One is shown in Fig. 3–8.

During the filling process, the fill hole is sighted through the window above it and brought to the focal point of the sealing laser. The 33 deg cone angle is designed to give an optical resolution of ~1 μm, as needed to find a ~2 μm–diameter fill hole. The entire cell and a surrogate target-focusing grid are mounted side-by-side on the same XYZ translation stage. The relative positions of the fill hole with respect to the focusing grid center is determined by illuminating and bringing each one in turn to the focus of a fixed telemicroscope camera, and recorded. The laser is first focused on the center of the grid outside the cell. The translation stage then brings the capsule fill hole into focus at the same location on the hole-imaging camera that the grid center has been imaged to. The focal point of the sealing laser will then be coincident with the hole. Alternatively, if the capsule surface is smooth enough, the laser can be focused directly by reflection off the top of the capsule.

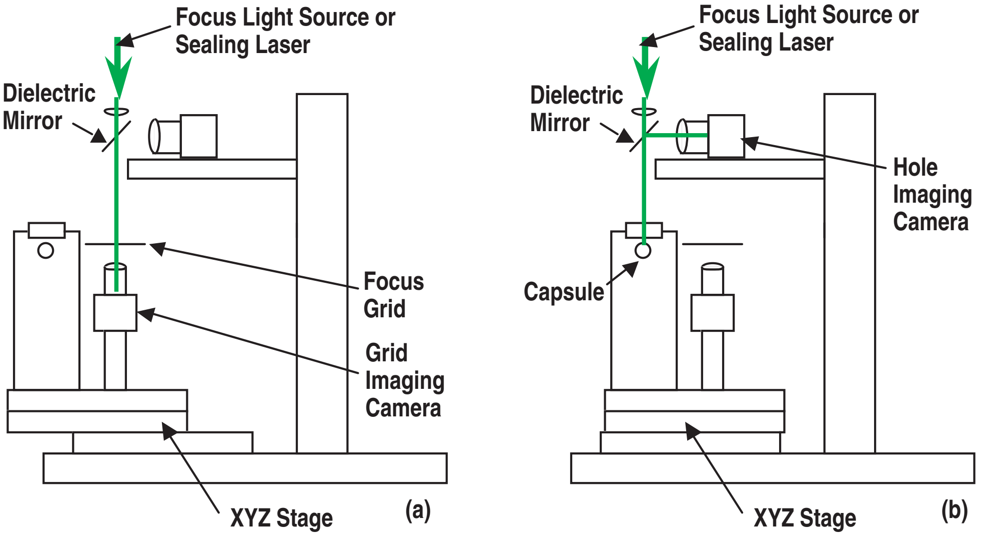

Fig. 3–8. Laser sealing scheme.

Once the desired DT fill is achieved, the laser is used to seal the hole through the window. The filled and sealed capsule is removed by reversing the above-described assembly process. Initially the actual DT fill is determined by weighing the capsule. If needed, the filling parameters, ΔPVT, is adjusted to account for density uncertainty in the "funnel" tip so that the desired capsule fill can be achieved with high yield.

3.2.2.2. Bonded Capsules. GA developed the detailed conceptual design of the pressure filling and bonding cell shown in Fig. 3–9. This work was documented in a detailed, 56-page, memo titled "Design of a Cell for Filling and Bonding Beryllium Capsules," IFT03/003, August 26, 2003.

The design is based on a commercially available pressure vessel. The vessel cavity is lined with solid quartz insulation. An electrical heater, composed of a heating coil, a quartz tube, and radiation shields, is inserted into the insulated space. The beryllium cylinder pairs to be filled and bonded, kept slightly apart by curved disc springs, as shown in Fig. 3–10, are stacked in a slotted cylindrical holder. The design can accommodate a batch of eleven pairs of beryllium cylinders at a time. The holder is placed inside the heater and the top quartz insulation is added. The vessel closure, with a dead weight hung from an extension of the valve stem at the top, is put in place and sealed. The vessel is evacuated, back filled with pressurized DT gas, and sealed. The heater is turned on "high" to quickly heat up the beryllium cylinder to the desired 850°C bonding temperature; it is then turned on "low" to maintain this temperature. A dummy beryllium cylinder fitted with a thermocouple is placed at the bottom of the stack of cylinder pairs to monitor their temperature and a programmable controller controls their temperature profile versus time. When temperature and DT pressure have stabilized, the dead weight is lowered by turning the valve and brought to rest on top of

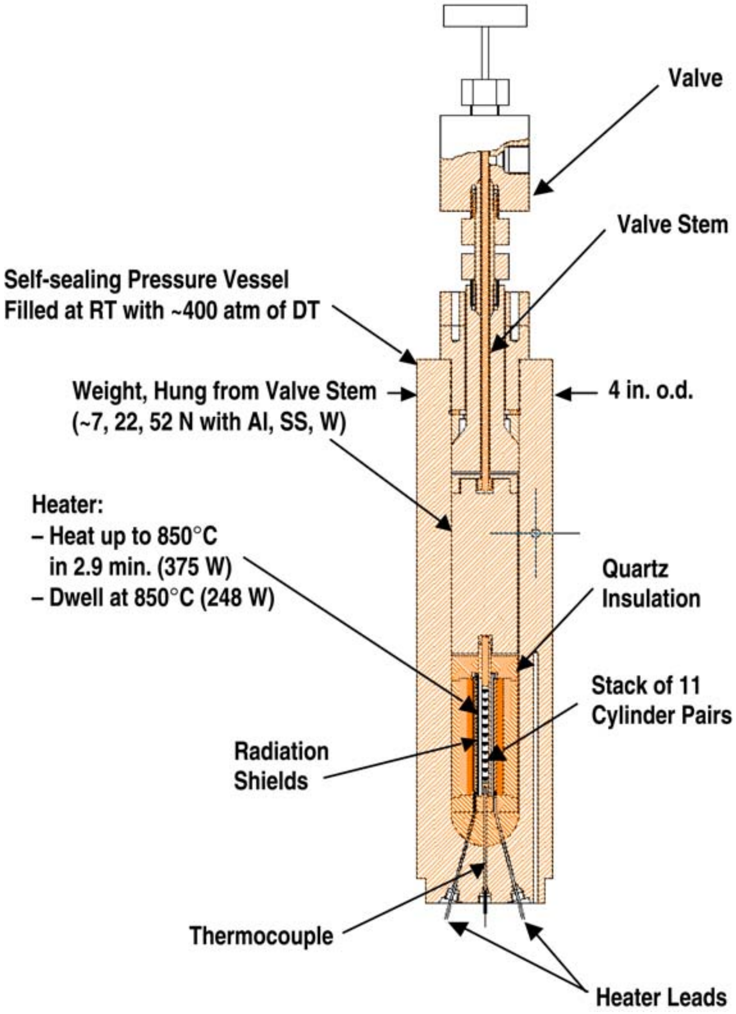

Fig. 3–9. Filling and bonding cell.

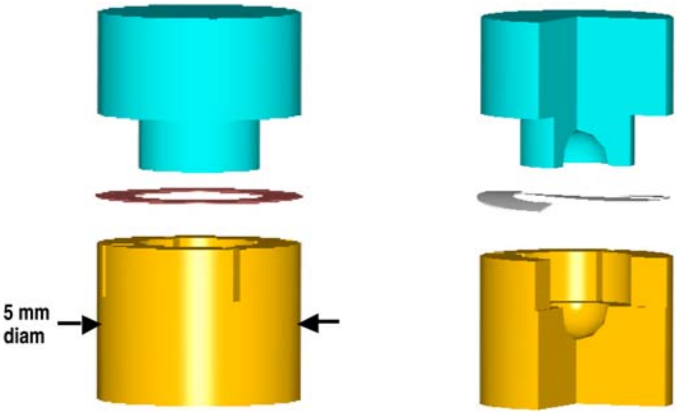

Fig. 3–10. Two views of a typical cylinder pair.

the cylinder stack to apply the desired constant bonding pressure. After the desired bonding time is reached, the vessel is allowed to cool, the DT is pumped out, and the vessel is vented. The assembly process is then reversed, and the eleven DT-filled and bonded cylinder pairs are taken out for inspection and machining into spherical capsules.

In this manner, the final mass of DT-fill in the bonded capsules is solely determined by the cell's initial pressure and temperature and the bonding temperature, which are relatively easy to control and measure with accuracy. However, the DT temperature, and thus its density, is not uniform during bonding. Therefore, the correlation between the measured parameters and the mass of DT sealed inside the capsules during bonding will have to be determined by monitoring process parameters and weighing the cylinders to determine fill.

The heating coil is made from 21-gauge (0.0724 cm-diameter), INCONEL 617, wire with a 1332°C (1605 K) melting temperature. The wire is 267 cm-long, spiral-wound with a 0.152 cm-pitch into a 10 cm-high coil with a 1.3 cm-OD. It is hung inside a quartz tube that supports it and serves as a layer of thermal insulation and a radiation shield.

The thermal feasibility of the design was established with transient and steady state finite-element thermal analyses. Updated thermal properties were used for DT and the cell materials. The analysis results are summarized in Figs. 3–11 and 3–12. The power required to heat up the cylinders from ambient to 850°C in 2.9 minutes, then to maintain them at this temperature, is respectively ~375 W and ~248 W. The thermal stress safety factors in the quartz internals were calculated and found to be larger than three in the thermal insulation and larger than six in the tube that supports the heating coil.

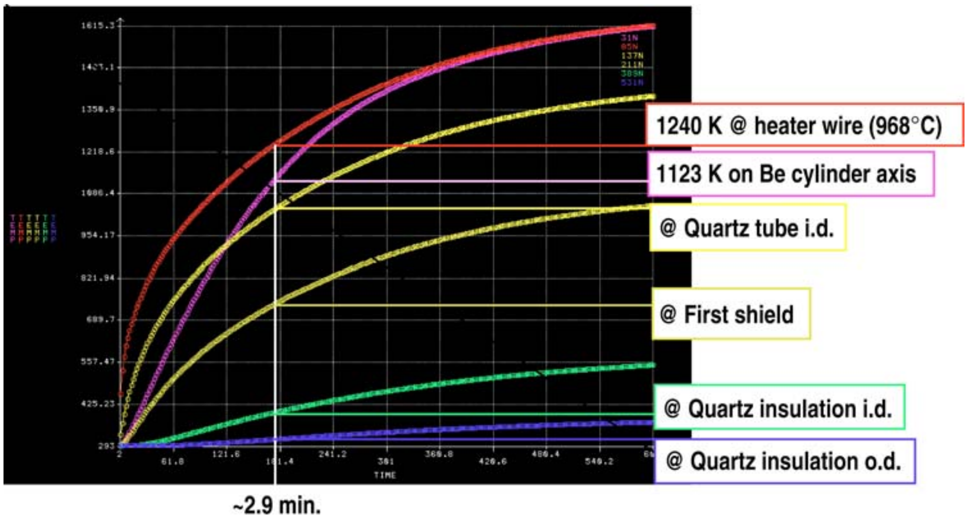

Fig. 3–11. Bonding cell component temperatures (K) versus time (s) during cylinder heating from RT to 1123 K (850°C).

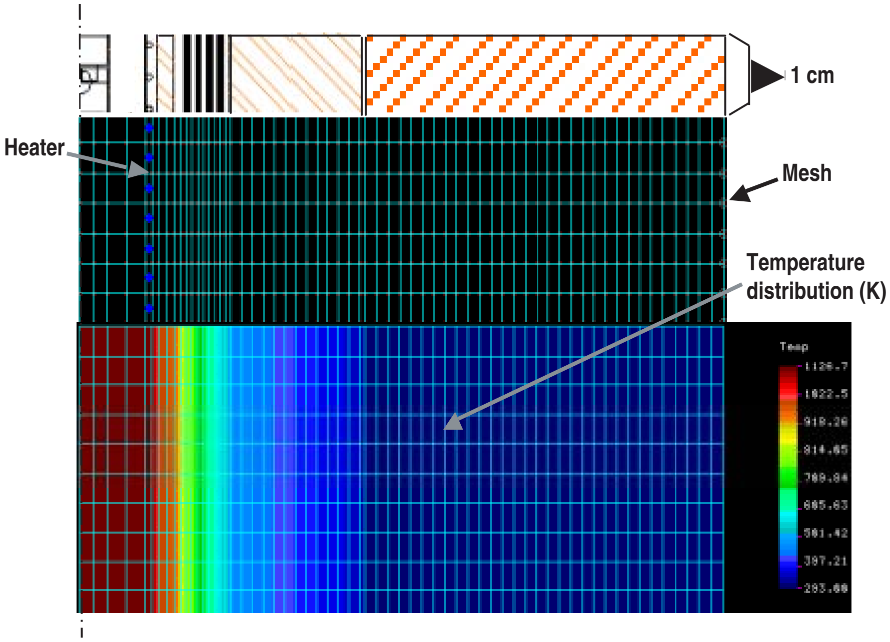

Fig. 3–12. Radial distribution of temperature (K) from the cell axis (left) to the vessel o.d. (right) during cylinder bonding dwell at 1123 K (850°C).

3.3. CENTER FOR ADVANCED CRYOGENIC LAYERING (D. BITTNER)

Center Head: Don Bittner (Schafer)
Technician: John Burmann (Schafer)
Designers: Raymond Fraze and Jerry Stewart (Schafer)

The NIF will require the development and fielding of complex cryogenic hohlraum target assemblies. The hohlraum target contains a spherical polymer capsule filled with frozen DT. The DT must be conformal to the interior of the capsule and be extremely smooth. The current baseline design calls for uniform DT layers approximately 100 μm thick on the interior of a 2 mm diameter capsule. The interior DT surface must be smoother than 0.5 μm rms. The development of suitable cryogenic targets is crucial to the success of NIF.

We continue to actively develop techniques to layer a capsule inside the cylindrical geometry of a hohlraum. Since completing the IR ring injection experiments, we have designed, fabricated, and started assembly of the fiber injection experiment. For this experiment, the IR enters the hohlraum through six optical fibers attached to the hohlraum barrel. In addition, we are optimizing the slow cooldown technique to determine how far below the triple point one can cool a layer under low IR power. Finally, we have begun raytrace modeling studies to understand the effect that thick-walled NIF scale capsules will have on our brightband analysis.

3.3.1. Layering Fundamentals

There are three basic layering techniques that have been investigated or are currently under development at LLNL. The first technique, referred to as β-layering, relies on the heat produced by the β decay of tritium to redistribute solid DT. The second two techniques are called enhanced layering methods since the β-layering effect is present in all targets containing tritium and these techniques serve to “enhance” the β-layer. IR layering augments the β-decay volumetric heating of solid DT using absorbed IR laser power. Joule heating uses an electric field typically produced by a microwave cavity to excite electrons in the gas at target center. These electrons are created by the β-decay electrons and the excited electrons produce an enhanced heat flux at the gas-solid surface. Joule heating will not be discussed further in this report.

When liquid DT is quickly frozen in an isothermal shell, it forms a rough mass on the bottom of the container. Because the DT solid self heats at a volumetric rate of $q_s = 5.06 \times 10^{-2}$ W/cm^3, there are variations in the temperature of the surface of the ice as the film thickness varies. The thicker areas of the film are warmer and, consequently, have higher vapor pressures, so material tends to sublime away from these regions and recondense at the cooler areas. If the container is isothermal, the ice surface at equilibrium conforms to the surface of the container. For pure DT, the rate at which the material migrates can be shown to be[1]

---

[1] Martin, A.J., et al., J. Vac. Sci. Technol. A **6** (3), 1885 (1988); J.K. Hoffer, L.R. Foreman, Phys. Rev. Lett. **60**, 1310 (1988); T.P. Bernat, et al., ICF Quarterly **1**, 57 (1991).

$$R_{DT} = \frac{q_s}{s\rho_s},$$

where s is the heat of sublimation (1550 J/mol) and $\rho_s = (5.18 \times 10^{-2}\,\mathrm{mol/cm^3})$ is the density of the solid, so that $1/R_{DT} = 27$ min.

The temperature profile within the solid layer calculated in one dimension is

$$T(x) = \frac{-q_s x^2}{2k_s} + \frac{q_s h x}{k_s} + T_0,$$

where k_s is the thermal conductivity of the solid, x is the distance from the inner edge of the container, h is the thickness of the ice, and T_0 is the temperature of the container. For wavelengths that are large compared to the surface thickness, the derivative of the temperature of the solid-gas interface with respect to the solid thickness becomes

$$\frac{dT(h)}{dh} = \frac{q_s}{k_s} \quad .$$

For 100 μm of DT ice this is 0.15 K/cm. The increase in surface temperature with increasing surface thickness drives the smoothing process. An increase in dT(h)/dh will result in a smoother surface. This is the foundation of the enhancement techniques.

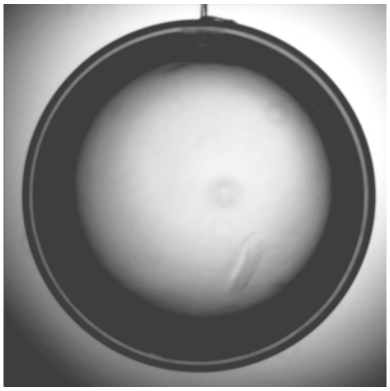

Fig. 3–13. Shadowgraph of a 125 μm layer inside of a 2 mm diameter 40 μm thick polymer capsule with a fill tube. The ice layer is the narrow white band just inside of the capsule edge. The layer roughness is 1.1 μm rms over modes 1 to 50. It is expected that removal of the fill tube and better centering of the shell will reduce the rms substantially by removing a source of low mode defects. The defect in the lower right part of the capsule is left over from where the slowly grown surface met during initial formation. The small circular defects are out of focus dust particles on the polymer capsule surface.

The quick freeze protocol just described for β-layering is conceptually simple but does not produce smooth layers. Multiple crystallites nucleate during the rapid cool. Grain boundaries between these crystallites are of sufficient surface energy to remain after the β-layering process comes to equilibrium and cause substantial surface defects in the final layer.[2] Quickly frozen β-layers are too rough to measure by shadowgraphy. The grain boundaries disrupt the surface finish sufficiently to cause breaks in the bright band. This bright band is caused by reflection of light off of the gas-solid interface. An example from a very smooth layer is shown in Fig. 3–13. The break up of the bright band renders our analysis techniques ineffective. Quick-frozen β-layers are not suitable for ignition targets.

Slowly forming a single nucleation site at a temperature just below the triple point and slowly cooling the layer approximately 80 mK at a rate of 0.25 mK/min until the layer is completely formed can produce smoother β-layers. Layers formed in this manner have been made as smooth as 0.4 μm rms. However, this number is somewhat stochastic and recent data indicate that it is dependent on the specific crystal orientation of the nucleation seed

---

[2] Sater, J., et al., Fusion Technol. **35**, (1999).

crystal. It is desirable to reduce this roughness to increase the robustness of the target with respect to ignition.

After formation, a DT layer can be cooled to approximately 19.3 K without degrading the surface. Cooling further causes the formation of cracks due to thermal contraction of DT. Most NIF target designs currently specify a DT layer temperature of 18.3 K. If this requirement is to be met, enhancement techniques must be applied to the layer.

3.3.2. IR Layering

To generate bulk heat for mass redistribution, (with or without tritium radiation), the collisionally induced IR vibration-rotation band is excited with a laser. The solid volumetric heating rate, Q_{IR}, and thus the redistribution rate, R_{IR}, and surface roughness are adjusted by controlling the incident IR intensity. The maximum Q_{IR} for hydrogen isotopes is limited by the vibrational relaxation time to $Q_{IR} \sim 1000\ Q_{DT}$. As mentioned previously, Q_{DT} is defined as the volumetric heating rate of DT (50 mW/cm^3). These large Q_{IR} values enable control of the hydrogen layer shape as well as enhance the redistribution process in laser-heated hydrogen solids. Proof-of-principle experiments to test the viability of the IR heating process were performed using a square sapphire cell filled with either HD or D_2.[3]

Initial IR layering experiments using shells were attempted with the goal being to form a single component HD layer from a solid lump using a quick freeze protocol. As was the case with DT, the layers formed this way were all found to be extremely rough. In order to improve the quality of the inner solid surface, a technique was developed that is conceptually identical to the slow freeze technique used for the multicomponent DT layers. Here a solid HD sample is first uniformly illuminated with IR radiation and then slowly warmed until the solid melts. As soon as the solid melts, the temperature is lowered until solid starts forming in the shell. At that point, the sample temperature is held constant until the solidification process is complete. This process was developed using volumetric heating rates on the order of 8 Q_{DT} on HD layers 150 μm or greater in thickness. 100 μm layers produced in this fashion have been made as smooth as 0.8 μm rms.[4]

In the case of both the tritiated as well as nontritiated hydrogen samples, smooth layers are formed near their respective triple points. This is, however, not the NIF design point temperature. The layers generally tend to remain smooth to approximately 0.5 K below the triple point before starting to degrade. Attempts to slowly cool smooth β-layers to 18.3 K, (1.5 K below the triple point), have not been successful. At high IR laser powers, on the order of 30 Q_{DT}, we have successfully produced uniform layers 1.5 K below the HD triple point (Fig. 3–14).

---

[3] Collins, G.W., et al., J. Vac. Sci. Technol. A **14**, (1996).
[4] Bittner, D.N., et al., Fusion Technol. **35**, 244 (1999).

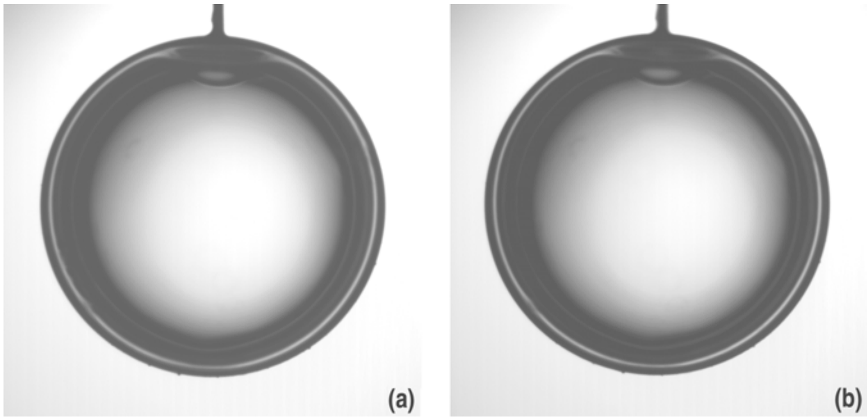

Fig. 3–14. Shadowgraph images of a layer where (a) is a uniform 50 μm thick HD layer formed near the triple point and (b) is the same layer cooled to 1.5 K below the triple point. The layer was formed inside a 40 μm thick and approximately 1 mm O.D. **D**-GDP shell with an attached fill tube. The volumetric heating rate in this case was $Q_{IR} = 30\ Q_{DT}$.

3.3.3. Enhanced Cryogenic Layering

3.3.3.1. IR Fiber Injection Experiment. We are in the process of investigating two IR injection techniques. Over the past two fiscal years we reported on our IR "ring injection" hohlraum experiments.[5,6] For these experiments optics external to the hohlraum were used to form a ring of IR radiation that was injected into the hohlraum through each laser entrance hole (LEH). An alternative to injecting IR through an LEH is to fiber couple the IR into the hohlraum through openings in the hohlraum wall. Over the past year we have designed, fabricated and started the assembly of an IR "fiber injection" experiment. This has also required a significant modeling effort in addition to designing the characterization and developing an understanding of how to make suitably rough hohlraums. R. London, B. Kozioziemski, and R. McEachern, all of LLNL, have contributed significantly to our joint effort on this project.

Based on the modeling calculations of B. Kozioziemski and R. London, we are in the process of fielding a hohlraum with six attached optical fibers. Figure 3–15 shows a drawing of a NIF-scale hohlraum with six optical fibers. There are three fibers spaced 120 deg apart on each end of the hohlraum. The two sets of three fibers are rotated 60 deg with respect to each other to help minimize nonuniformities in the heating of the capsule and ice layer. The design of the experiment is very similar to the ring injection experiment. In this design the external optics are replaced by optical fibers. For this hohlraum, as in the ring injection experiment, there are no LEH windows. The hohlraum assembly will be enclosed in a vacuum can filled with approximately 1 Torr of helium gas (Fig. 3–16). In addition to completing the design this year, parts have been fabricated and assembly has started. Figure 3–17 contains a picture of the roughened hohlraum mounted in a copper support. The

---

[5] "Inertial Confinement Fusion Annual Report", General Atomics Report GA-A23852, pp. 3-90 – 3-92

[6] "Inertial Confinement Fusion Annual Report", General Atomics Report GA-A24147, pp. 3-24 – 3-27

support provides both thermal and mechanical support for the hohlraum. In addition, the copper support provides positioning support for the six optical fibers. Figure 3–18 is a view of the hohlraum through the window in the vacuum can.

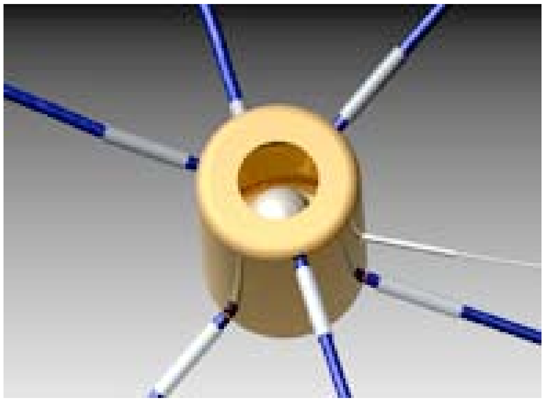

Fig. 3–15. Drawing of a NIF-scale hohlraum with six optical fibers attached. There are three fibers on each end of the hohlraum. In addition, there is a 2 mm capsule with attached fill tube.

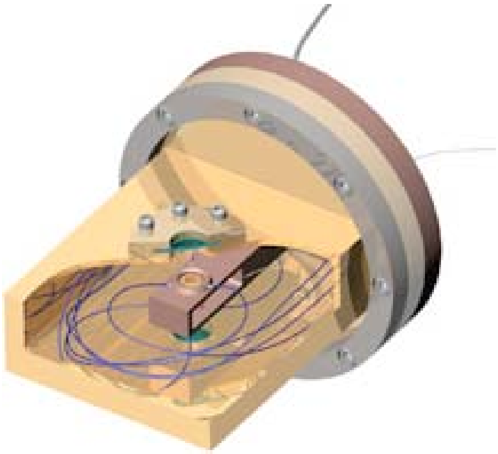

Fig. 3–16. Cut-away drawing of the vacuum can showing the NIF-scale hohlraum inside.

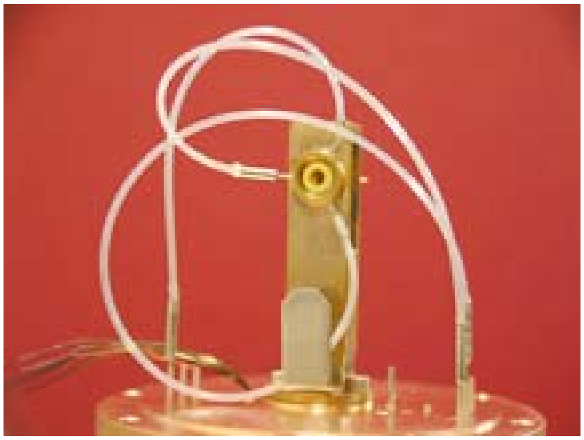

Fig. 3–17. Picture of a roughened hohlraum in the copper support.

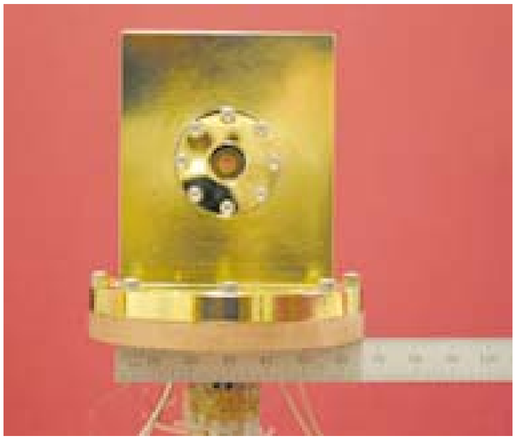

Fig. 3–18. View of the hohlraum through one of the windows in the vacuum can.

Using six optical fibers for injecting the IR requires optics for splitting a single laser beam output into six roughly equal beams. Figure 3–19 shows the layout of the optics. A combination of three 50:50 and two 70:30 beamsplitters divides the laser output beam into six beams that are then fiber coupled. To compensate for power variations between the six beams, an IR polarizer is placed in front of each fiber coupler. A seventh output coupler allows for optionally coupling the full laser output into a single fiber. An IR polarizer in front of this fiber coupler also provides the ability to adjust the power coupled into the fiber.

There are both positive and negative aspects to the ring injection and the fiber injection techniques for applying IR heating to a cryogenic hohlraum on NIF. The primary positive

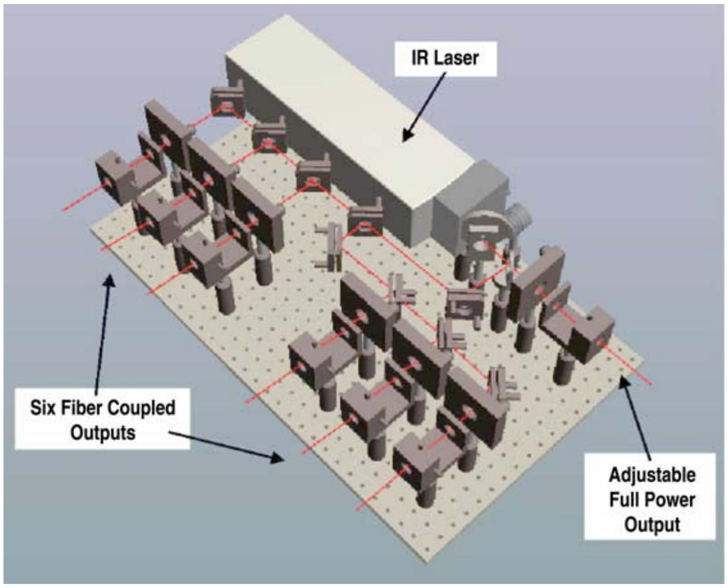

Fig. 3–19. Component layout for splitting the laser output into six beams that are fiber coupled. A seventh output allows for fiber coupling the full laser output power.

aspects of the ring injection technique are that the power into each LEH can be independently varied, the IR ring provides for cylindrically symmetric illumination of the hohlraum wall, and the external optics allow for adjusting the pointing of the injected beam into the hohlraum to help shape the ice layer. However, this also means that there are optics mounted on the shroud which require space and have weight, and, since the shroud will be removed prior to the shot, the IR will have to be turned off prior to shot time. The fiber injection technique addresses the external optics issue. There will be no shroud optics, and the IR can remain on till shot time. In addition, there can be power adjustability for each fiber output. The fiber injection technique also has some negative aspects. Attaching multiple fibers with leak-tight seals to the hohlraum makes for a more complicated hohlraum. There is also no way to adjust the pointing of the IR, and there is no longer cylindrical symmetry in the IR illumination of the hohlraum wall. The lack of cylindrical symmetry results in variations in the capsule and ice layer heating profiles not only along the hohlraum axis but also about the hohlraum axis.

3.3.3.2. IR Heating Optimization Study. A proof of principle experiment was conducted that showed that a layer illuminated with high IR power could be cooled to 1.5 K below the triple point.[7] The volumetric heating rates used for the successful slow cooldowns were at least 25 times the volumetric heating rate due to beta decay heating of DT (25 Q_{DT}). These volumetric heating rates are too high for application in a NIF-scale hohlraum. Current capsules are expected to absorb IR at roughly 10–20 times the rate of IR absorption in DT. Since the relatively low thermal conductivity helium tamping gas extracts the capsule heat, IR heating can generate a large temperature drop between the capsule and hohlraum wall. Based on current hohlraum designs, the estimated maximum allowable IR volumetric heating rate will be 4–10 Q_{DT}. The proof-of-principle experiment addressed the question of whether or not it was possible to use IR to cool a layer 1.5 K below the triple point without layer degradation. There is a different question to ask at these lower IR volumetric heating rates: at low IR power, how far can the temperature be lowered before there is significant layer degradation?

---

[7] "Inertial Confinement Fusion Annual Report," General Atomics Report GA-A23537, pp. 5-1 – 5-3

As part of the proof-of-principle experiment, slow cooldowns were conducted at low IR power as well as high IR power. Initial experiments included heating rates of 1–10 Q_{DT}. All of these low IR power experiments were conducted at a cooling rate of 20 mK/3 min. The experimental results indicated that layers could potentially be cooled to between 0.5 and 1.0 K below the triple point.

We have started a new series of slow cooldown experiments. These experiments are being performed at low IR power to determine how low in temperature a layer can be cooled before significant layer degradation occurs. Initial experiments have been performed primarily at ~4 Q_{DT}. So far we have had limited success in forming and maintaining the layer quality while cooling the layers. Figure 3–20 shows the images of a layer at three different temperatures during a slow cooldown. Defects in the ice layer grew as the temperature was lowered, but they did not show rapid growth as the temperature was lowered ~1 K. The corresponding power spectra, shown in Fig. 3–21 did not significantly change as the temperature was lowered. Typically in these slow cooldown experiments, roughening appears as growth in the higher order modes. These results are consistent with the earlier proof-of-principle slow cooldown experiments.

3.3.3.3. Shadowgraph Modeling. The brightband in the shadowgraph images is used to determine the symmetry of the ice layer. Early modeling[8] of the brightband resulted in an equation that related the position of the inner ice surface to the brightband using parallel rays. Due to the total internal reflection of rays off the inner ice surface, a parallel ray incident on the shell will reflect off the inner ice surface and leave the shell as a parallel ray to produce the brightband. Figure 3–22 shows the parallel ray reflecting off the inner ice surface. In this case the shell is 1.04 mm o.d. with a 40 μm thick wall, and the ice layer is 150 μm thick. The ray is traveling along the +z-axis at y = 0.95545 mm. The ray color denotes relative power from red, corresponding to high power, to blue, corresponding to low power. The relationship between the position of the brightband and the inner ice surface can be calculated from the relatively straightforward geometry of the model.

In addition to raytrace modeling ice layers in thin-walled shells with parallel rays, later modeling efforts addressed the issue of brightband analysis when the capsule was backlighted with a diffuse light source.[9,10] Figure 3–23 shows the shadowgraph radial lineouts for both a collimated source and a diffuse source raytrace through a 2 mm o.d. by 1.92 mm i.d. shell containing a 100 μm ice layer. Also noted on the plot is the calculated inner ice edge position from the parallel ray model. The main difference in the two lineouts, other than the relative intensities, is the width of the brightbands. The diffuse source has a broader brightband. For either collimated or diffuse backlighting the brightband is a relatively isolated feature with low background intensity and there is no significant qualitative difference between the shadowgraph images.

---

[8] "Inertial Confinement Fusion Annual Report", General Atomics Report GA-A22816, pp. 5-11– 5-13

[9] J.A. Koch, et. al., Fusion Technol., 38, 123 (July, 2000)

[10] J.A. Koch, et. al., Fusion Technol., 43, 58 (Jan, 2003)

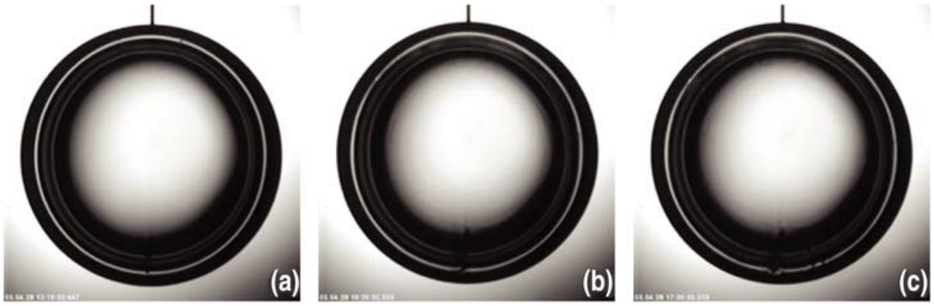

Fig. 3–20. Three images showing the slow layer degradation occurring during a slow cooldown at ~4 Q_{DT}. Layer degradation is indicated by breaks in the brightband and the growth of features in the central area of the image. The temperature drops below the triple point for images (a)–(c) are 0.208 K, 0.798 K, and 0.955 K, respectively.

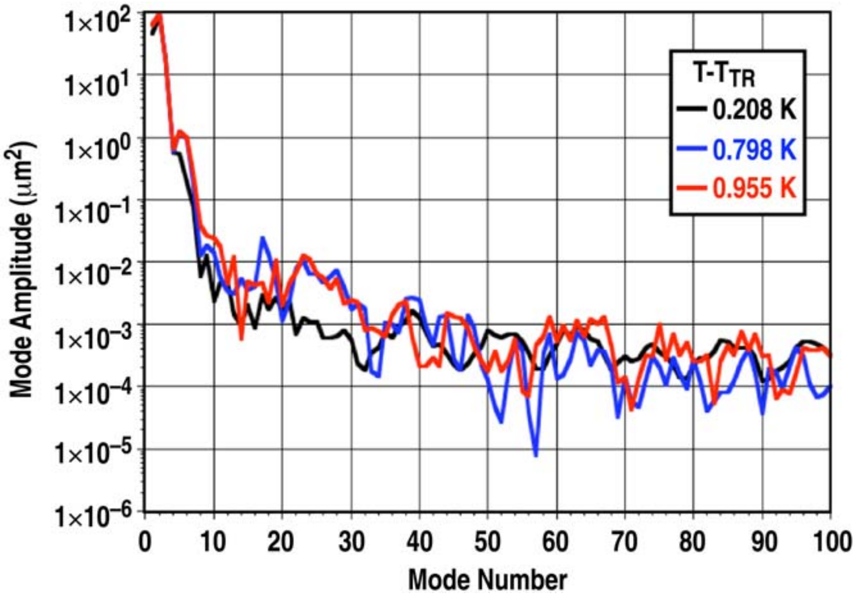

Fig. 3–21. Power spectral plots for the three images shown in Fig. 3–20. The temperature drops below the triple point for images (a)–(c) are 0.208 K, 0.798 K, and 0.955 K, respectively.

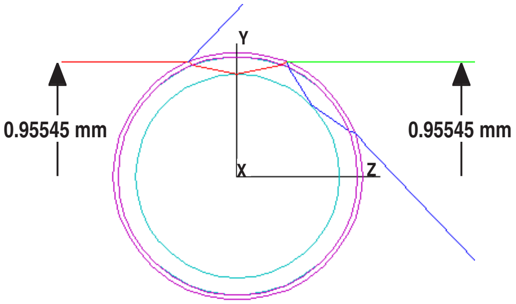

Fig. 3–22. Raytrace diagram of a parallel ray through the shell and ice layer. The total internal reflection off the inner ice surface results in a parallel exit ray that forms the brightband.

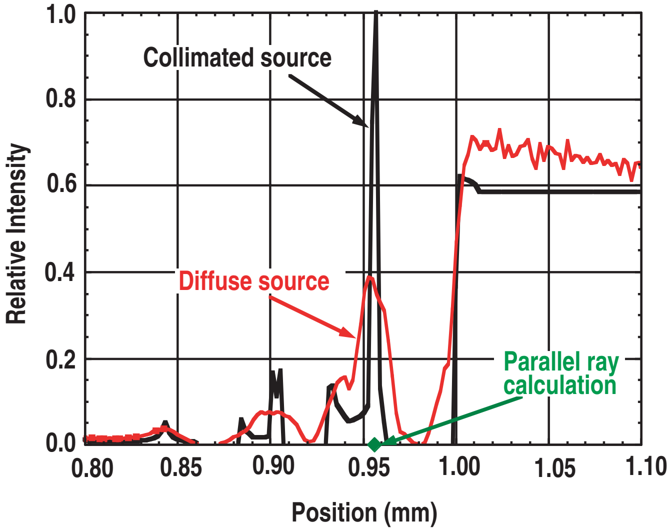

Fig. 3–23. Shadowgraph radial lineouts for both a collimated source and a diffuse source raytrace through a 2 mm o.d. by 1.92 mm i.d. shell containing a 100 μm ice layer. Also noted on the plot is the calculated inner ice edge position from the parallel ray model.

However, NIF capsules have thick-walled shells. A typical NIF capsule has a wall ~150 μm thick. During this fiscal year we began exploring how shadowgraphs of thick-walled capsules differ from those of thin-walled capsules and determining the significance of that difference on our analysis procedures. Figure 3–24 shows the shadowgraph radial lineouts for both a collimated source and a diffuse source raytrace through a 2.17 mm o.d. by 1.85 mm i.d. shell containing a 100 μm ice layer. Also noted on the plot is the calculated inner ice edge position from the parallel ray model. It is readily apparent from the lineouts that the type of backlighting source makes a significant difference in the resultant image. There is no apparent brightband when diffuse backlighting is used. Near the brightband location there is a light-to-dark transition in intensity instead of an intensity peak. For the collimated source, the brightband is surrounded by ”background” intensity.

The basic issue with analyzing thick-walled shells is that the brightband is not a relatively isolated feature. Light rays that would get refracted out of the optical system for thin-walled shells are collected by the optical system in the case of thick-walled shells. These differences between thick and thin wall capsules in the shadowgraph images require modifications to our analysis procedures. One modification option is to work with the diffuse backlighting and modify our analysis procedures. In this case one models ice layers with different layer roughnesses using a diffuse light source and determines if variations in the light-to-dark transition position correspond to the inner ice surface roughness. If there is a correspondence with the inner ice surface roughness from the modeling, then performing an edge detection analysis of the light-to-dark transition in the shadowgraph images will provide information about the inner ice surface roughness.

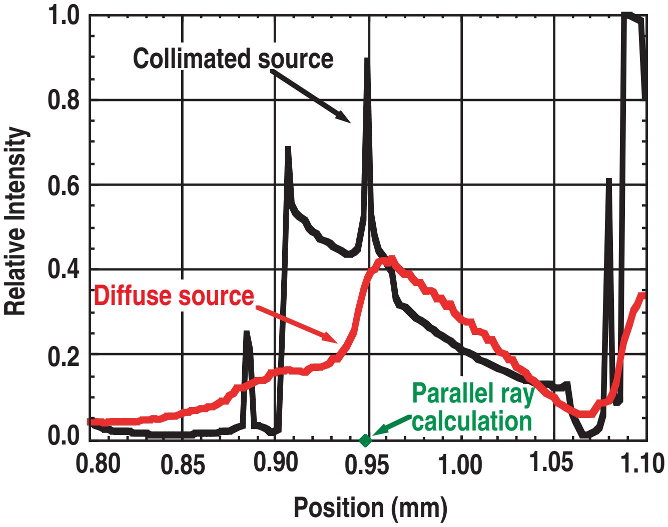

Fig. 3–24. Shadowgraph radial lineouts for both a collimated source and a diffuse source raytrace through a 2.17 mm o.d. by 1.85 mm i.d. shell containing a 100 μm ice layer. Also noted on the plot is the calculated inner ice edge position from the parallel ray model.

A second modification option is to use a collimated light source and to work around the “background” rays. Here one could simply analyze the brightband above the background intensity or try to remove the background intensity. We have performed some raytrace modeling using a simple relay lens system to look at ways of removing the “background” rays. A possible option for removing the rays is to backlight the capsule with a ring of parallel light and place a pinhole at the focal point between the two relay lenses. Basically the only rays that make it through the optical system are parallel rays that form the brightband or pass outside the capsule. Figure 3–25 shows the results of one of our raytrace models. Here we modeled a 2.17 mm o.d. by 1.85 mm i.d. thick-wall shell containing a 100 μm ice layer. Although the brightband location is obvious without the pinhole in this case, one can see that the effect of the pinhole is to reduce the background intensity around the brightband.

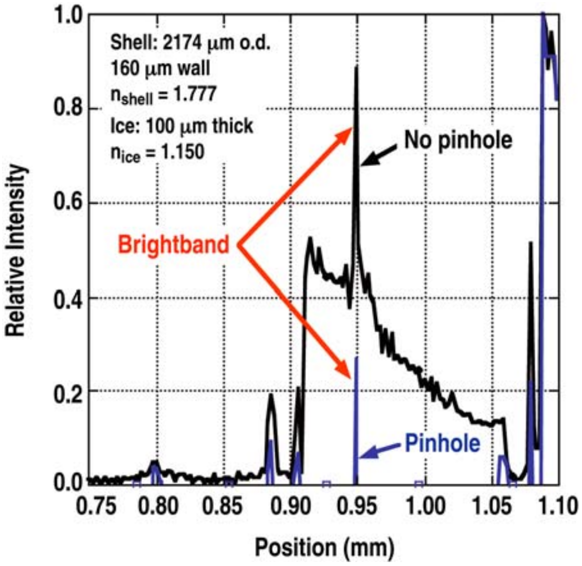

Fig. 3–25. Raytrace model lineout showing the reduction in “background” rays by using a pinhole in an image collection system. The parallel ray calculated brightband position is at 0.948 mm.

3.4. CENTER FOR TARGET COMPONENT FABRICATION AND FABRICATION DEVELOPMENT

Center Head: Jim Kaae (GA)

Scientists: Jim Kaae, Joe Smith, and Emilio Giraldez (GA)

Tecnicians: Clyde Shearer, David Woodhouse, Martin Hoppe, Jr., and Jason Wall (GA)

Overview

In FY03, fabrication of target components was our major activity. We produced a range of ICF target components for LLNL, LANL, SNL, and UR/LLE using combinations of high-precision micromachining, physical vapor deposition, and electroplating. Altogether in FY03, we produced 1352 very precise ICF target components of different types.

Development of techniques is needed to fabricate many of the orders we receive for new components each year. Several of these techniques are discussed in subsequent sections.

3.4.1. LLNL, LANL, SNL, and UR/LLE Deliveries (Jim Kaae)

Near-term fabrication and delivery of target components of many different designs and made of many materials is critical for the success of the DOE ICF program. We provided this important support for experiments by LLNL, LANL, SNL, and UR/LLE scientists.

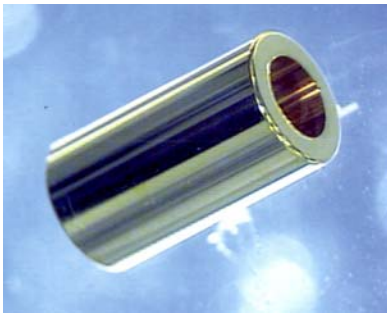

Fig. 3–26. Hohlraum with 25 μm walls.

3.4.1.1. LLNL Deliveries. Foremost among these were 228 gold-plated copper cylindrical hohlraum mandrels of 13 different geometries. These components ranged from 1.2 to 6.0 mm in diameter and from 2.5 to 10.0 mm in length. Dimensions were typically controlled to within ±2 μm. (Similar dimensional control was achieved in all of the components that we produced.) An example of a hohlraum with 25 μm thick walls formed when the copper mandrel was leached out is shown in Fig. 3–26.

Fig. 3–27. Copper hohlraum mandrel.

Twenty-three similar copper hohlraum mandrels of two different designs were coated first with a thin (2 μm) layer or gold and then with a thicker (100 μm) layer of epoxy rather than a single layer of gold. A photograph of one of these hohlraums is shown in Fig. 3–27.

Prototype NIF cryogenic hohlraums are more complex than conventional hohlraums and require more machining and coating steps. A photograph of one half of one of these hohlraums is shown in Fig. 3–28. (They are produced in halves so that assembly with an internal shell will be easier.) The body of the hohlraum has been roughened to give diffuse reflection of IR radiation, which may be used to expedite layering inside the shell once the hohlraum has been assembled. The process used to produce this controlled random roughness was developed in a cooperative effort between GA and LLNL. Seven whole cryogenic hohlraums (14 hohlraum halves) were produced for LLNL in FY02.

Two hundred and twenty-three of sixteen different types of gold-coated cylinders also were produced. Some of these were half-round cylinders, some were square cylinders, and some were round cylinders with and without flanges on the ends. A photograph of a square cylinder is shown in Fig. 3–29, and an example of a half-round cylinder is shown in Fig. 3–30.

Fig. 3–28. One-half of a cryogenic hohlraum.

Fig. 3–29. Square cylinder with copper leached out.

We also produced a set of 12 circular cylinders out of very pure aluminum. These cylinders are used as mandrels for mixed element (“cocktail”) deposition experiments being carried out at LLNL. Hohlraums made from these cocktails may have advantages over gold hohlraums in NIF.

Another type of cylindrical component that we produced was a copper mandrel with end flanges, the whole coated with epoxy. The fabrication of these components, which are used for studying laser-plasma interactions, is described in a subsequent section. A total of 37 of these components of 6 different designs were fabricated.

A small gold truncated cone similar to the one shown in Fig. 3–31 was another type of component that we produced. Altogether, we made 15 of these in 2 different geometries. As with the other gold components, these were made on copper mandrels.

Yet another gold-coated copper component that we produced this year was a small cup. Thirty-five of these cups in seven different designs were fabricated. Examples of the gold cups are shown in Fig. 3–32.

Fig. 3–30. Half-round cylinder with gold leached out.

Fig. 3–31. A small gold truncated cone.

Fig. 3–32. A set of gold cups in varying sizes.

Fig. 3–33. A disk with a precisely defined thickness and diameter.

Fig. 3–34. A gold cylinder with a conical flange on one end.

Two hundred and forty witness plates of eleven different designs also were produced for LLNL. Some were stepped; some contained sine wave profiles; and some were flat. They were made of pure aluminum, 6061 aluminum, OFHC copper, polyimide, and Ge-doped GDP.

We also had two separate requests for a total of 26 gold trapezoidal shields. The fabrication of these shields was discussed in last year's annual report.

Twelve NIF hohlraum window saddles were requested. This is a new component and its fabrication is described in a subsequent section.

3.4.1.2. LANL Deliveries. In FY03, we produced 255 precisely machined components of 16 different designs. One of these components was a disk with precisely defined thicknesses and diameters and very smooth surfaces. These disks were made from either gold or very pure aluminum and varied in diameter from 2 mm to 10 mm. Altogether 89 disks were produced. An example of one of the disks is shown in Fig. 3–33.

Another component that was produced for LANL was a gold-coated copper circular cylinder with a conical flange at one end and with the gold machined off of each end so that when the copper was leached away a gold tube would remain. Thirty of these cylinders of varying diameters and lengths were produced. A photograph of one of the cylinders is shown in Fig. 3–34.

We also made 65 small gold hohlraums similar to the one shown in in Fig. 3–26 in two different campaigns. The hohlraums were 1.6 mm in diameter and 1.2 mm long.

Sixty-two sloped pure aluminum witness plates with three different thicknesses were also fabricated.

In addition, we fabricated 21 gold cups that fit on the end of some of the gold cylinders.

Finally, we machined, gold plated, characterized and delivered 28 mandrels with a hemispherical end. After machining, the position of the copper mandrel in a special holder was measured, the mandrels were coated and dimensionally characterized, and then they were sent to another company (Alumiplate) for electroplating with aluminum. After this, they were returned to LANL, where they were inserted into a diamond turning machine and remachined using the position measured at GA. For this to succeed, it required precise measurements at both GA and LANL. The remachining was accomplished successfully.

3.4.1.3. SNL Deliveries. Of the 211 components produced for SNL in FY03, 33 were conventional gold hohlraums similar to the one shown in Fig. 3–26.

Another 63 were gold or 6061 aluminum disks of 8 different designs, none of which were the same as the designs requested by LANL. An example of one of the disk designs requested by SNL is shown in Fig. 3–35.

We also produced 65 witness plates of 7 different designs from very pure aluminum, GDP and Ge-doped GDP.

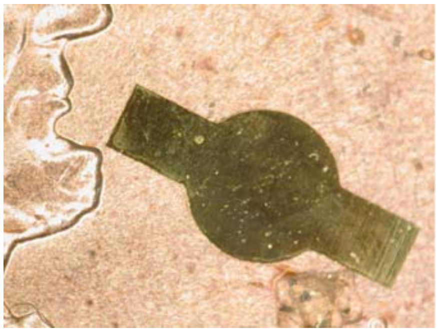

Fig. 3–35. A gold disk with tabs produced for SNL.

Finally, we fabricated 44 thin-walled aluminum cylindrical components of five different designs. These were fabricated by sputtering aluminum on an acrylic mandrel. They proved to be very difficult to fabricate; details of the process and the difficulties are described in a subsequent section.

3.4.1.4. UR/LLE Deliveries. The 123 UR/LLE deliveries consisted of 3 types of components. The majority were stepped and flat aluminum witness plates. One hundred and fifty of these plates of five different designs were produced, characterized, and delivered.

The remainder of components fabricated for UR/LLE consisted of 23 gold trapezoidal shields like those shown in Fig. 3–36 and 23 half-round cylinders like those shown in Fig. 3–30.

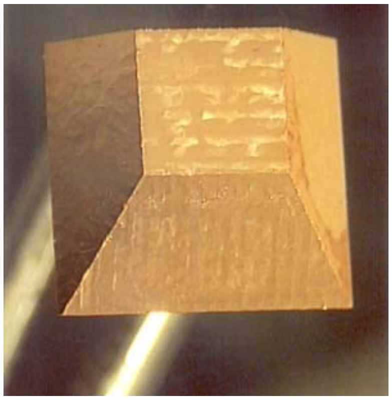

Fig. 3–36. A gold trapezoidal shield.

3.4.2. Fabrication of Epoxy Hohlraums

Epoxy hohlraums are used for studying laser-plasma interactions. Actually these components do not have the same shape as a normal gold hohlraum since the laser entrance hole is not smaller than the hohlraum barrel diameter; it is the same size as the barrel diameter. There are flanges on each end of the hohlraum for gluing thin windows to seal gas inside the hohlraum. Given this description, the component shown in Fig. 3–37 is easily recognized as an epoxy hohlraum. Following is a description of the technique used to fabricate epoxy hohlraums.

We begin with a copper mandrel that will be machined to the shape of the hohlraum in a brass holder, which will be used for centering and axial repositioning in the remachining process. The holder and the copper mandrel is shown in Fig. 3–38. The rear of the copper mandrel is shaped in a diamond turning machine with a tool oriented as shown in Fig. 3–39. After this operation, the barrel of the holder is machined, as shown in Fig. 3–40. This surface will be used for centering in the remachining process. Then a face on the holder is machined as in Fig. 3–41 and the axial position is recorded for repositioning in the remachining process. Following machining of the holder, the front of the copper mandrel is shaped with a diamond tool oriented as shown in Fig. 3–42. The holder is removed from the machine and it is manually coated with epoxy. When the epoxy has hardened, the holder/epoxy coated mandrel is reinserted into the diamond turning machine and the same operations as were used to shape the copper mandrel are repeated to remove excess epoxy to yield the desired barrel thickness and the thickness of the flanges.

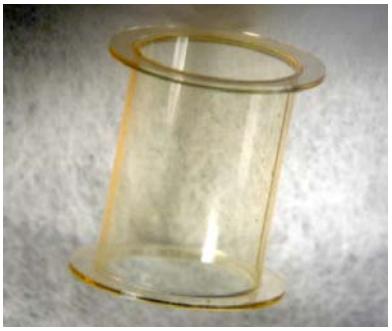

Fig. 3–37. An epoxy hohlraum.

Fig. 3–38. The copper mandrel and holder used for making epoxy hohlraums.

3.4.3. Fabrication of Thin-Walled Aluminum Tubes

Fabrication of thin-walled aluminum components poses problems that are not encountered in fabricating gold or epoxy components. The first is in a choice of the mandrel material. Aluminum is reactive with many acids, although copper could be used because nitric acid does not dissolve aluminum. However, we have found that for thin-walled components the hydrogen gas bubbles that are formed when an acid is used to leach the mandrel can distort the component. For that reason, we prefer to use acrylic mandrels when we fabricate thin-walled components. Acrylic can be dissolved with acetone and this exerts little or no force on the component.

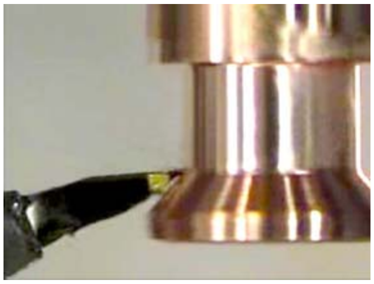

Fig. 3–39. The first shaping step on the copper mandrel.

A drawing of the foil tube is shown in Fig. 3–43 along with the dimensions. An acrylic mandrel machined to these dimensions is shown in Fig. 3–44.

The method that we chose to use to deposit the aluminum was sputtering. The acrylic mandrel was rotated during deposition so that the coating was uniform. A photograph of an acrylic mandrel in the sputtering chamber surrounded by the sputtering plasma is shown in Fig. 3–45.

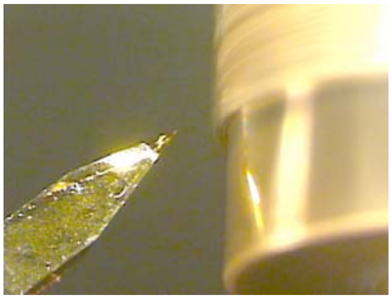

Fig. 3–40. Machining of the barrel of the holder for centering of the component after it has been removed and returned to the diamond turning machine.

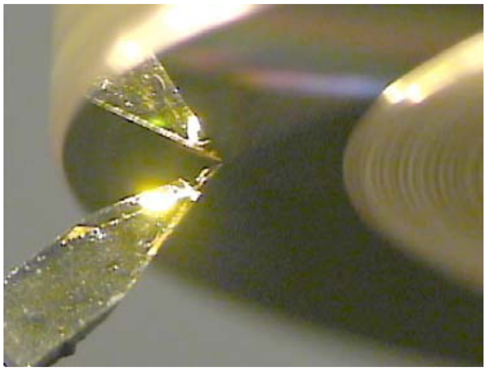

Fig. 3–41. Machining of a face on a holder to obtain an axial reference position.

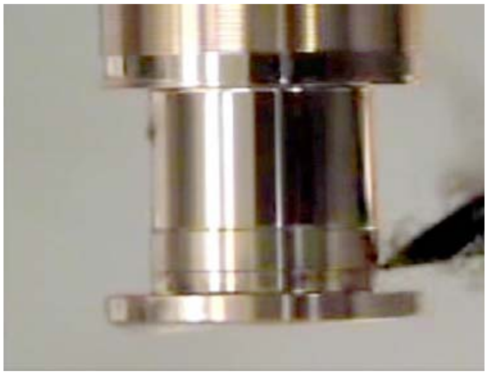

Fig. 3–42. Shaping the front of a copper mandrel. Note the different tool orientation from that shown in Fig. 3–39.

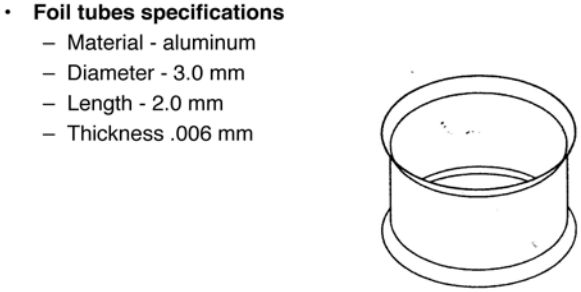

- **Foil tubes specifications**
  - Material - aluminum
  - Diameter - 3.0 mm
  - Length - 2.0 mm
  - Thickness .006 mm

Fig. 3–43. Drawing of foil tube with dimensions.

Fig. 3–44. An acrylic mandrel machined to the shape and dimensions shown in Fig. 3–43.

Fig. 3–45. The acrylic mandrel in a sputtering chamber.

Acrylic softens at a relatively low temperature and has a much higher coefficient of thermal expansion than aluminum. Therefore, it was important to keep the temperature of the component from getting too high during deposition. If this occurred, the coating would either crack or would show wrinkles as would occur when the aluminum was forced into compression by the acrylic shrinking more than the aluminum. Photographs of each of these are shown in Fig. 3–46.

To overcome cracking and wrinkling, we operated the sputtering system in an on-off mode, coating for two minutes and then cooling for seven minutes. This made the coating of the acrylic mandrels a time-consuming process. Another factor that enters into the success of obtaining good aluminum coatings on acrylic mandrels is the age of the aluminum sputtering target. As the target is used, a groove is developed where the sputtered material is removed. This causes the shape of the plasma to change and the deposition rate to decrease while the heat input to the component increases. We are still quantifying this effect to define the limiting age of targets.

With proper control, it is possible to produce aluminum coated acrylic mandrels as shown in Fig. 3–47. Machining of the aluminum off of the flanges as shown in Fig. 3–48 opens up these regions for dissolution of the acrylic. A completed part is shown in Fig. 3–49.

3.4.4. Fabrication of Window Saddles for NIF Cryogenic Hohlraums

Attachment of a planar diagnostic viewing port to the cylindrical wall of the NIF cryogenic hohlraum requires a saddle-like transition piece. This saddle-like transition piece is known as the window saddle. The window saddle, shown in Fig. 3–50, can be described as a cylinder with flanges at either end. One flange is flat, where a polymer window is attached, while the other flange is curved so that it can be attached to the side of the cryogenic hohlraum. While the basic design of this window saddle is straightforward, its fabrication is not, given the scale and precision of the component. We solved the fabrication problem by making a mandrel that consisted of two segments assembled together. Each segment was machined using a combination of diamond turning and diamond milling.

Figure 3–51 shows CAD renderings of the two segments that make up the window saddle mandrel. One segment consists of two coaxial cylinders of different diameters. The diameter of the small cylinder, also referred to as the pin, matches the inside diameter of the window saddle. The other segment consists of a curved section that matches the curvature of the curved flange. A hole is

Fig. 3–46. A defective aluminum coating showing wrinkles and cracks.

Fig. 3–47. An acrylic mandrel with a successful aluminum coating.

Fig. 3–48. An aluminum coated mandrel after the final machining step.

Fig. 3–49. A completed aluminum foil tube.

Fig. 3–50. CAD rendering of a window saddle.

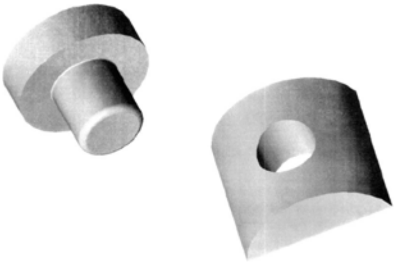

Fig. 3–51. Segments that make up the window saddle mandrel.

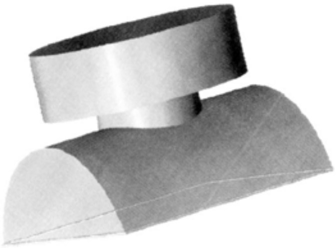

Fig. 3–52. Window saddle mandrel assembly.

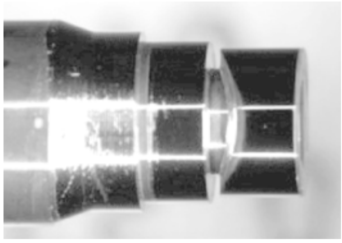

Fig. 3–53. A photograph of the window saddle copper mandrel.

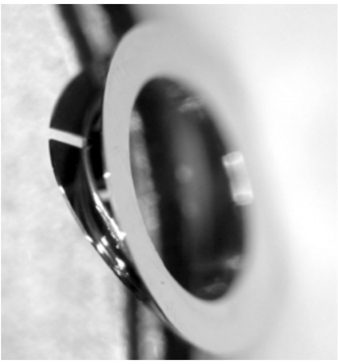

Fig. 3–54. The electroformed window saddle.

machined in the center of the curved section and is used in aligning and securing the two segments together.

The two segments are assembled together by pushing the pin into the hole until the pin bottoms out. Shrink fitting the two segments with an interference of 4 μm between the diameter of the pin and diameter for the hole gave the best results. Shrink fitting eliminated the deformation and abrasion of the pin as it is pushed against the sides of the hole during assembly. The pin segment was cooled in liquid nitrogen to –196°C and the curved segment was heated to 100°C with a heat gun. This temperature difference is sufficient for the pin to fit inside the hole without any interference prior to assembly. The assembly was carried out with the aid of an alignment fixture and an arbor press. Figure 3–52 shows a CAD rendering of the assembled mandrel. A completed window saddle copper mandrel is shown in Fig. 3–53.

The window saddle is electroformed by electroplating 30 μm of gold. Initial gold plating trials showed that if there are any gaps in the fit between the pin and the hole, gold is plated into the gaps. On dissolution of the copper this appeared as thin gold protrusions on the surface of the curved flange. To overcome this problem, the copper mandrel was plated with 4–5 μm of copper to fill in the gaps. The diameter of the pin and diameter of the hole were adjusted accordingly to compensate for the added copper thickness from the copper plating step. Figure 3–54 is a photograph of the finished window saddle.

3.5. CENTER FOR POLYMER AND COATINGS AND FOAM CAPSULE DEVELOPMENT

Center Head: Abbas Nikroo (GA)

Scientists: Kuo-Chun Chen, Don Czechowicz, Barry McQuillan, Reny Paguio,
Joe Pontelandolfo (GA), and Masaru Takagi (LLNL)

Technicians: Erwin Castillo, and Wes Baugh (GA)

Introduction

We report on the major activities of the Center for Coatings, Polymer and Foam Shell Development in FY03. Our major task in FY03, as in the previous years, was the support of on time delivery of targets requested by all the various DOE ICF labs. Our group was responsible for two essential operations in achieving this task; PAMS shell production and GDP coatings, necessary for fabrication of the variety of requested capsule and flat targets. PAMS batches were manufactured to stock our inventory of mandrels and as needed for individual orders. Doped and undoped GDP coatings were deposited on a variety of substrates, mainly shells, in the course of fabrication of the majority of the targets delivered.

In addition, we had the administrative task of coordinating the target delivery requests for University of Rochester's Laboratory for Laser Energetics (UR/LLE). We report on the LLE deliveries in Section 2 and outline the various types of targets delivered to LLE. The various FY03 UR/LLE's deliveries are categorized by type and difficulty in that section. Through the data and knowledge bases accumulated over the past several years, fabrication of many of the previously challenging and time consuming targets for UR/LLE has become routine. We discuss the procedure used in fabrication of the more routine LLE targets in Section 2 as well.

We also delivered gas retentive fast ignition targets for the first time shot at OMEGA as part of LLE's effort. These targets are also developmental involving a shell mounted on a gold cone. The new developments in this area dealt with fabrication of gas filled targets and the related characterization of the assembled targets.

In Section 3, we report on the developmental targets delivered to UR/LLE. We continued our efforts towards the development of foam shells for University of Rochester's Laboratory for Laser Energetics (LLE). We present a brief summary of this developmental effort supported by a contract from UR/LLE. The major developments in foam fabrication were production of batches of low density (100 mg/cc) shells with relatively high yields (25%) of shells with the appropriate wall uniformity. Gas filled foam shells with a GDP permeation barrier delivered to UR/LLE were shot for the first time in the US both at room temperature and in cryogenic mode at LLE.

A number of indirect drive NIF target fabrication issues were examined as well by our group in FY03. Production of NIF quality GDP mandrels was examined in FY03. By appropriate changes to the PAMS fabrication and drying procedures and clean GDP coating environment, a high percentage of mandrels can be produced which are below or very close to the NIF curve. These developments are summarized in Section 4.

We were also in charge of assembling a new GDP coater and a new sputter coater funded through the EQU-03 task. These coaters were assembled and placed in use for production activities reducing equipment bottlenecks associated with these activities. Figure 3–55 shows pictures of the two coaters in our laboratories.

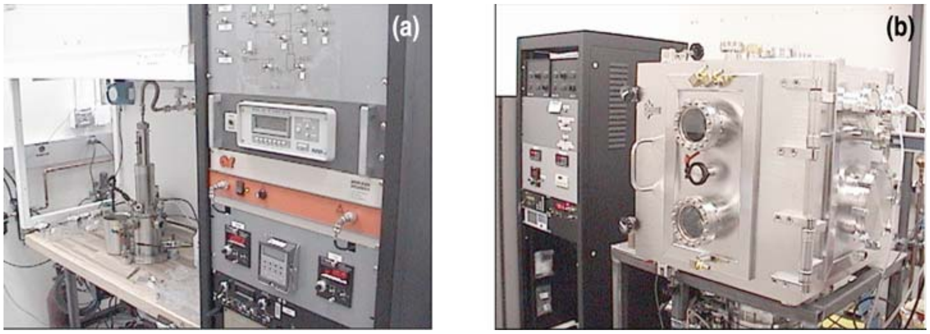

Fig. 3–55. (a) New GDP coater (b) new sputter coater assembled using EQU-03 tasks to reduce production bottlenecks associated with this equipment.

3.5.1. UR/LLE Deliveries

In FY03, our group continued coordinating delivery of targets to UR/LLE. Delivery requests were received from UR/LLE points of contact and processed through the various steps of fabrication to ensure on time delivery. Final target data were sent to LLE electronically via e-mail as well as posted onto a password protected web site accessible by LLE personnel. A total of 1025 shells in 57 separate orders were delivered to UR/LLE for shots on the OMEGA laser. The different types of shells delivered as part of the orders mentioned above are categorized in Fig. 3–56. Figure 3–56(a) lists the deliveries according to the number of orders (or batches) delivered, while Fig. 3–56(b) shows the number of shells provided for each type. In the figures, the different types of shells are also delineated by the level of difficulty involved in fabricating the shells. Routine types, mainly pure CH and CD shells, ~15–35 μm in wall thickness, are those that can be made in a relatively short period of time and with a minimum of effort. Fabrication of these types of shells has become routine through the experience we have gained in the past few years in producing such shells. This is described in more detail below. While many of the shells were of the routine type, a significant number were of developmental or transitional types. Transitional types mainly consist of multi-layer and thin wall cryogenic shells. While the major development on these types has been completed, they still involve multiple manufacturing and testing steps and require more effort.

The developmental types involved foam and fast ignition shells. The developmental efforts in FY02 and FY03 on foam shell fabrication led to several deliveries of foam shells in FY03. The foam development is summarized in Section 3. We also delivered gas retentive fast ignition targets for the first time shot at OMEGA as part of LLE's effort. These targets are also developmental involving a shell mounted on a gold cone. The new developments in this area dealt with making the targets gas retentive and the related characterization of the assembled targets. The reader is referred to Ref. 11 for the details of this developmental activity.

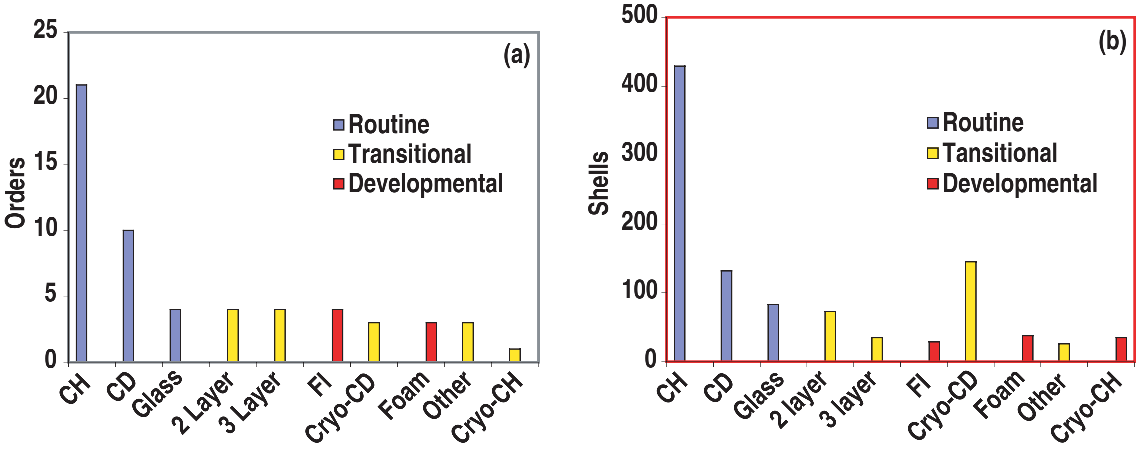

Fig. 3–56. Summary of capsule deliveries to UR/LLE in FY03 categorized by the various types of shells delivered. (a) Number of orders (batches) delivered. (b) Number of shells delivered.

Deliveries of developmental types are more challenging and usually require more lead-time and substantially more manpower. Our goal is that in time the transitional and developmental targets will become routine. These plots point out that the effort involved in providing all the needed targets depends not only on the number of shells or orders delivered but the difficulty involved in fabrication as well.

In addition to the deliveries above, we also provided targets as “samples”. These were either shells or flat samples provided to UR/LLE for uses other than laser shots. Over 300 shells, mostly PAMS shells, were delivered as “samples” along with about a dozen flat full density films. We also delivered a variety of foam shells and foam planar targets as “samples” described in Section 3. As part of our delivery activities, we also performed extensive mechanical and permeation testing of thin wall shells used for cryogenic shots for quality control. This information is necessary to ensure consistent shell quality for the successful high pressure filling and cryogenic cooling at UR/LLE.

As mentioned above, fabrication of pure CH and CD shells has become routine. The procedure used in making such shells routinely is described below. The three-step depolymerizable mandrel technique (Fig. 3–57)[12] is used to fabricate single or multi-layer GDP shells for deliveries to UR/LLE, as has been done for the past several years. This technique affords the flexibility needed for capsule fabrication of the different diameters and wall thicknesses. As the technique involves three distinct steps, each step needs to be routine

---

[11] D.W. Hill, E. Castillo, K.C. Chen, S.E. Grant, A.L. Greenwood, J.L. Kaae, A. Nikroo, S.P. Paguio, C. Shearer, J.N. Smith, Jr., R.B. Stephens, D.A. Steinman, and J. Wall, “Fabrication and Characterization of Fast Ignition Targets,” to be published in Fusion Sci. Technol. 2004.

[12] S.A. Letts, E.M. Fearon, S.R. Buckley, M.D. Sacula, L.M. Allison, R.C. Cook, “Preparation of Hollow ICF Targets Using a Depolymerizable Mandrel,” J. Mater. Res. **372**, 125 (1995).

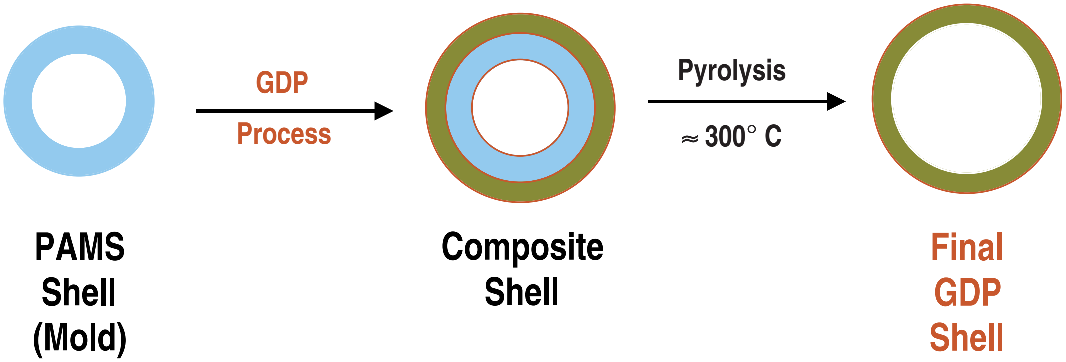

Fig. 3–57. Depolymerizable mandrel technique is used extensively in capsule fabrication for LLE. PAMS mandrels are overcoated with GDP and after pyrolysis of the PAMS mandrel, the final capsule is a pure GDP shell.

in order to allow routine fabrication of shells. Since PAMS shells are the starting point, a full stock of PAMS shells is needed to allow rapid and timely response to the various delivery requests from UR/LLE including the pure CH and CD shells. Therefore, a full inventory of such shells, fully characterized for size and quality, is continuously maintained in the diameter range suitable for UR/LLE targets. In fact, in FY03 when the canonical shell diameter needed for direct drive shots at OMEGA was changed to ~860 μm from ~920 μm, a full set of shells involving batches spanning the full range of 800–900 μm was fabricated (Fig. 3–58). The next step in fabrication, CH and CD GDP coatings, has been perfected over the years with coating rates fully established allowing fabrication of shells with the desired wall thickness to within the current specifications, ± 1 μm, consistently. In the pyrolysis step both the wall and diameter of shells shrink considerably (several percent) and the shrinkage depends on the material type. Therefore, over the past several years, extensive shrinkage data has been accumulated for the different types of GDP coatings, including CH and CD. Figure 3–59 shows a sample of such data used to determine the initial shell diameter and wall thickness needed to obtain the final shells with the desired dimensions. Such predictive capability is essential in producing shells with the required diameters and wall thicknesses to within specifications *routinely*. The above procedure was followed numerous times during FY03 to fabricate the multitude of shells requested, many time with leads times as short as 2 weeks or less.

3.5.2. Foam Shell Fabrication

In FY02, we had embarked on a developmental effort to fabricate foam shells for future use at UR/LLE. Two types of foam shells are required. First type, referred to as low density, are required to have a density of ~30–140 mg/cc and wall thicknesses ~30–100 μm. The second type, referred to as high density, has a density of ~180–250 mg/cc and wall thicknesses of 80–100 μm. A thin, ~1–5 μm, CH gas permeation barrier is required for both types. The diameter of these shells is required to be in the current UR/LLE size range of ~820–880 μm. An important specification is the shell wall thickness uniformity, which is specified to be less than 5 μm. We present a summary of the progress achieved in FY03. For a more complete description the reader is referred to Ref. 13.

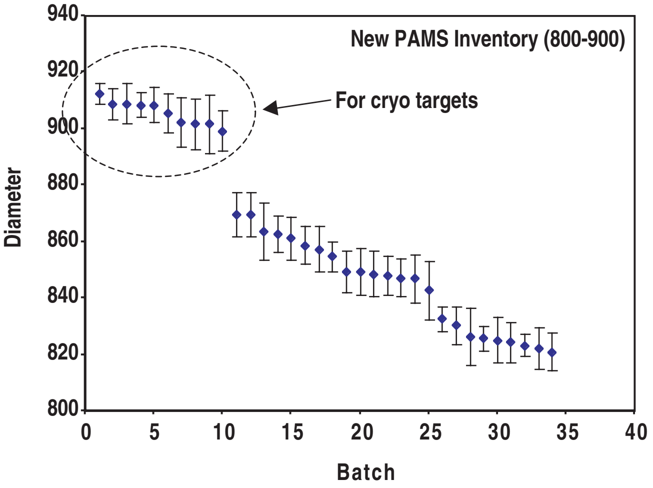

Fig. 3–58. A new inventory of PAMS shells was fabricated in FY03 for the new UR/LLE diameter size of ~860 μm. The larger diameter shells near ~900 μm is used for fabrication of cryogenic shells which shrink during the cooling at UR/LLE's cryogenic system. An inventory of PAMS shells allows rapid and reliable delivery of GDP shells.

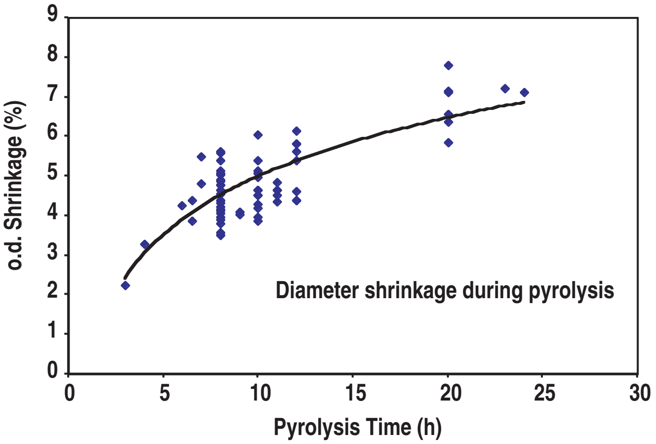

Fig. 3–59. Diameter shrinkage of GDP-coated PAMS shells during the pyrolysis step in the depolymerizable mandrel process (Fig. 3–57) as a function of pyrolysis time. Proper knowledge of shrinkage during pyrolysis allows the correct choice of PAMS shell diameter and pyrolysis time. The spread in the data is due to the GDP coating thicknesses which are tabulated separately.

---

[13] A. Nikroo, D. Czechowicz, R. Paguio, A.Z. Greenwood, Masaru Takagi, "Fabrication and Properties of Overcoated Resorcinol-Formaldehyde Shells for OMEGA Experiments," to be published in Fusion Sci. Technol. 2004.

In FY02, we had shown that we were able to fabricate low density shells using resorcinol-formaldehyde (R/F) foam chemistry chosen as the chemistry of choice because it leads to transparent foam shells, which allow optical characterization of shells. In addition, we had shown that GDP coatings could be used as the permeation barrier. Such coatings led to gas retentive shells; however, not with a 100% yield. We had begun to make shells with polyvinylphenol (PVP) coatings deposited using a chemical technique. In FY03, we examined several reproducibility issues related to the low density shells and GDP permeation barrier. In addition, we continued our work on GDP and PVP permeation coatings. We also began investigating fabrication of high density shells.

We first examined the reproducibility and reliability of fabrication of low density shells with the required wall thickness uniformity. Dozens of batches of shells were made and density matching of the various phases in the microencapsulation process was varied to improve wall uniformity. To obtain enough statistics, many batches were dried using the critical point drying procedure and shells were characterized using full interferometric measurements to obtain 4 pi wall uniformity. By careful density matching, batches of shells with a high percentage (~25%) of shells with the required wall uniformity could be made. This level of reproducibility was sufficient for production purposes. Figure 3–60 shows a histogram of wall non-concentricity showing the relatively wide spread in wall uniformity within the batches and the fact that about 25% of shells have a non-concentricity below ~5% (wall uniformity of <5 μm) for many batches.

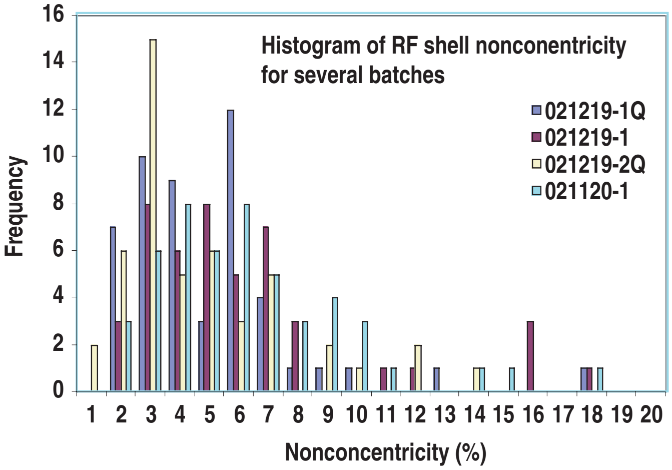

Fig. 3–60. Histograms of the wall concentricity of four different batches of low density foam shells. Such histograms were produced for many batches. ~25% of shells meet the specification of ~3% to 5% nonconcentricity (~5 μm wall thickness nonuniformity).

GDP coatings and PVP coatings were both examined on a batch basis for gas retentiveness. Foam shells were coated with ~3–4 μm of GDP or PVP. The overcoated shells were tested for argon holding capability by filling the shells and then following the argon content by its x-ray fluorescence as a function of time in the XRF unit. Figure 3–61 shows the typical signal from GDP coated shells. About 60%–70% of GDP coated shells and 90%

of PVP coated shells were gas retentive. The fact that not all the coated shells held gas meant that every shell needed to be tested for gas retention before delivery for laser shots. In addition, we found that the PVP coated shells shrank by as much as 20% for coatings of ~3 μm (Fig. 3–62). This presented a concern regarding densification of the foam layer under the coating. Therefore, GDP coatings were used exclusively for the deliveries to UR/LLE in FY03 and are planned to be used in the future as well.

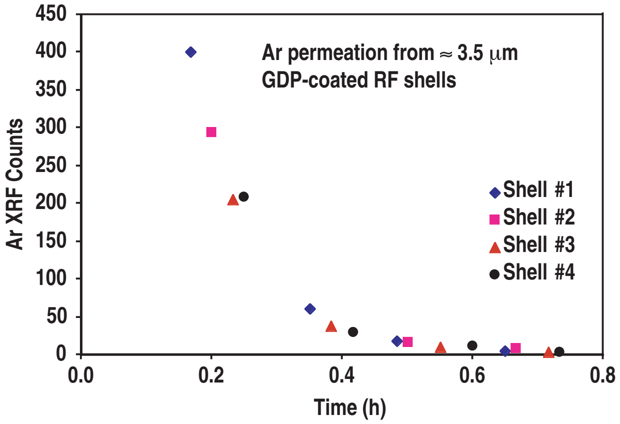

Fig. 3–61. Argon permeation out of ~3 to 4 μm thick GDP coated RF foam shells as observed by the argon x-ray fluorescence signal from the shells. The permeation rate is consistent with a 3 to 4 μm GDP layer.

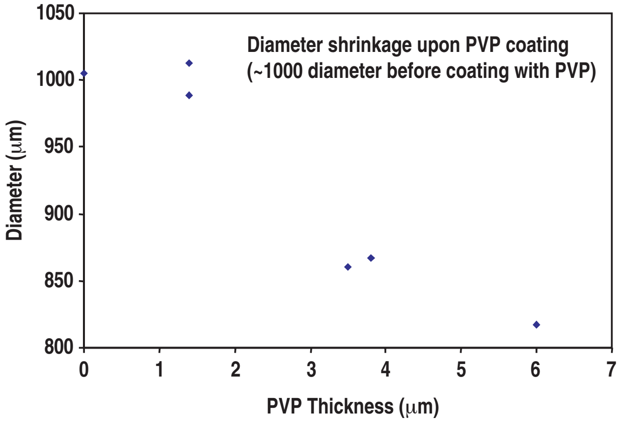

Fig. 3–62. PVP coated RF foam shells shrink by as much as 20% depending on the thickness of the coating. At the nominal 3 to 4 μm thickness, the PVP coated RF shells shrink by 15% which leads to densification of the inner foam layer.

We also examined fabrication of high density shells. Initially, shells disintegrated during the curing step of fabrication (before the shells had fully gelled). Variations in the recipe to cause faster gelation exacerbated the problem. The recipe was then varied to allow slower gelation which led to fabrication of intact shells [Fig. 3–63(a)] although with a very poor surface and by optimization of the gelation time intact shells with good surface [Fig. 3–63(b)] were produced. The wall uniformity of high density shells has been worse than those of low density shells (only <5% of shells in the best batches have wall uniformity <5%). Our current effort is concentrated on improving the wall uniformity of the high density shells.

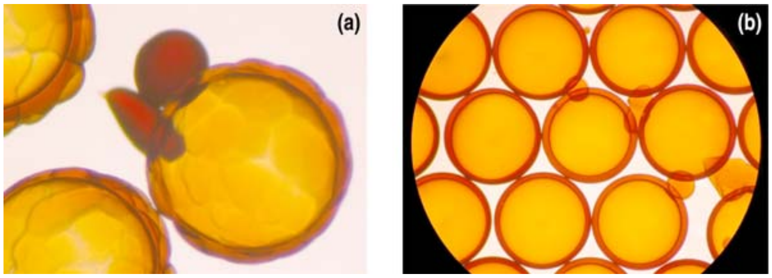

Fig. 3–63. (a) Intact high density RF shells with a soccer ball-like surface. The poor surface results from improper chemistry of the RF recipe. (b) Adjustments to the RF recipe leads to intact shells with proper surface.

Our developmental effort led to practical application in form of several batches of over coated gas retentive foam shells to UR/LLE in FY03. In addition to shell fabrication we also made a number of flat foam films and cylinders. GDP coated flat foam films were delivered to UR/LLE for laser shots on OMEGA as part of astrophysical experiments. Planar cryogenic target holders (copper cells) were also filled with foam for surrogates in study of cryogenic filling of shells (Fig. 3–64).

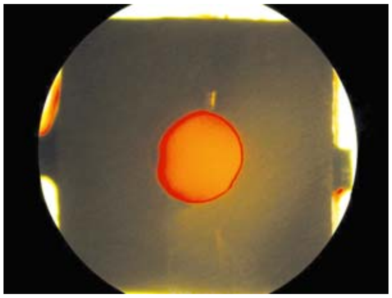

Fig. 3–64. View of a planar cryogenic target cell filled with RF foam which was delivered to UR/LLE to be used as a surrogate in cryogenic filling and cooling studies.

In summary, our progress in FY03 on shell fabrication led to the first ever laser shots, both room temperature and cryogenic, in the US involving gas filled foam shells (with a GDP permeation barrier) at UR/LLE.

3.5.3. NIF Mandrel Fabrication

In FY03, we examined the issues involved in making NIF quality ~15 μm GDP mandrels in production mode. While the demonstration of the feasibility of making such a mandrel was shown over two years ago, making such high quality shells consistently had proven to be difficult. In FY03, we were able to consistently produce NIF quality GDP mandrels by improvements to the three-step process (Fig. 3–57) used in making such mandrels. These improvements developed in FY03 to the processes of PAMS shell fabrication, GDP coating and pyrolysis are briefly summarized below. The reader is referred to Ref. 14 for further information and background.

---

[14] A. Nikroo, B. McQuillan, R. Paguio, M. Takagi, R. Cook, J. Bousquet, “Progress in 2 mm Glow Discharge Polymer Mandrel Development for NIF,” to be published in Fusion Sci. Technol. 2004.

NIF quality PAMS batches can be made by adding high molecular weight PVA to the polyacrylicacid (PAA) stripping fluid in the outer W2 phase during the encapsulation process. Many batches of shells made using this technique were examined by spheremapping and it has been shown that nearly 75% of shells sampled from several different batches are at or below the NIF standard. Also, we have demonstrated that when clean handling techniques and gentle agitation of shells are exercised, GDP coated PAMS shells are also of NIF quality. The GDP coating laboratory has been converted to a class 1000 cleanroom, with the areas around the coaters being ~ class 10 by employing positive flow hoods. In general, some 70%–80% of the GDP coated shells are NIF quality. We found that GDP shells degraded severely during pyrolysis, with some even exploding and others becoming too oblate to be spheremapped, when the newly fabricated NIF quality PAMS mandrels were used. The mechanism for such degradation is the residual solvents left in the newly fabricated PAMS shells. A simple solution to this problem is pre-baking of PAMS shells prior to coating. This must be done at sufficiently low temperatures where the PAMS shells do not deform themselves. In fact, pre-baking at room temperature is the gentlest pre-baking procedure and effective in removing the solvents. This process does take nearly two months, but it involves the least handling of shells and hence the least amount of debris pick up.

Table 3–1 summarizes the results for a number of batches of GDP mandrels made using carefully selected pre-baked PAMS shells from a NIF quality batch. Careful clean handling procedure was used in selecting and loading of PAMS shells into the GDP coater. As can be seen about 70% of the shells were at or below the NIF standard. The goal of this work was to have 50% of the mandrels be at the NIF standard. Figure 3–65 shows AFM spheremaps for a subset of these shells.

Table 3–1
Summary of Spheremap Results Using Pre-baked PAMS Shells

Batch	NIF Quality	Total
1	6	6
2	2	3
3	1	3
4	3	3
5	4	4
6	1	4
7	4	4
8	4	6
9	2	4
10	3	4
11	3	3
12	1	3
13	3	3
14	2	3
Total	39	53

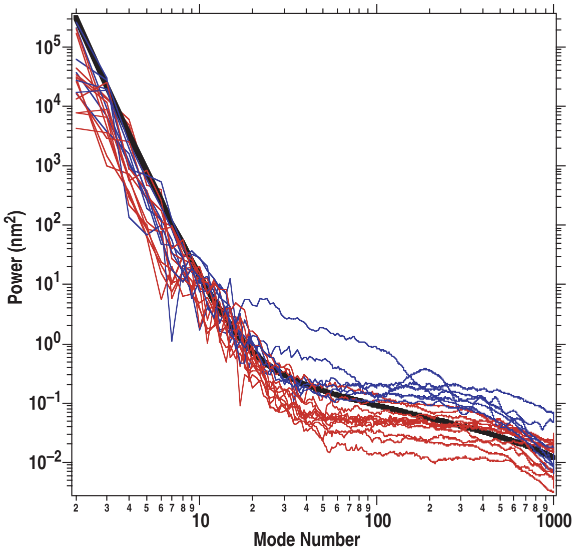

Fig. 3–65. A sample of 19 AFM power spectra of shells listed in Table 3–1 along with the NIF standard (thicker black line). Over 50% of shells are at or below the NIF curve as desired. All usual nine traces from three orthogonal axes were included in calculating the power spectra shown.

3.6. CENTER FOR FOAM DEVELOPMENT AND PRODUCTION

Center Head: Diana Schroen (Schafer)

Scientists: Jon Streit, and Kelly Youngblood (Schafer)

Technicians: Chris Russell, and Dave Tanner (Schafer)

The Center for Foam Development and Production is responsible for the development and delivery of low-density foam components used as precision target and diagnostic components. These targets are requested primarily by SNL, but occasional requests are also made by NRL, LANL and LLNL. Three staff members at two facilities are responsible for this work. On-site at SNL are Jon Streit and Diana Schroen. In Livermore, Kelly Youngblood assists as funding permits. This combination of people and facilities gives us the ability to produce five foam types: polystyrene, resorcinol-formaldehyde aerogel, silica aerogel, DVB, and TPX (4-methyl-1-pentene). The foams can be molded, machined, doped, or cast with embedded objects.

For SNL, we produced 133 foams in FY03; that number is up from 113 in FY02. It is also important to stress the unique processes that we developed to produce the required foams. While the final foam may have identical compositions to foam produced by published techniques, the foams produced by GA/Schafer have been made by modified procedures, which at a minimum make them more cost effective to produce. Often, the changes in production have been very dramatic and resulted in additional benefits. The production of TPX is the most extreme example of a change in process that resulted in high production efficiency and in benefits to the final product. The established process for producing TPX foams was to dissolve the polymer in a blend of durene and naphthalene, cool, machine to shape, and extract the durene and naphthalene in a freeze drier. This process is very labor consuming as each foam must be individually machined and defects are not evident until after the solvents have been removed. In FY97, we developed a process to dissolve the polymer in a single solvent, cyclohexane. The frozen cyclohexane/TPX blend cannot be machined, but is easily molded and then extracted in a freeze drier. Molding is much more labor efficient and the cyclohexane/TPX process minimizes voids and other density perturbations. Even the structure of the final TPX foam is changed, and changed for the better. The old process produced a plate-like structure in the foam, the cyclohexane process produces a three-dimensional net structure. The net-like structure results in a much more uniform density.

In FY00, we demonstrated that this process also allowed for the embedding of objects such as diagnostic foils, markers and gas containing capsules. Clearly, to obtain precision placement of embedded objects requires casting, not machining. In FY03, we extended the embedding process to include a 6-μm shim surrounding a capsule. Both the capsule and the shim were required to be centered in the foam. Figure 3–66 is a composite of two radiographs, a length view and an axial view showing the centering of the shim and capsule in the foam.

We also extended our capabilities to doping of TPX foams. With an eye to flexibility, we developed two techniques, particulate doping and organometallic doping. The hope was that with these two techniques we would be able to supply a wide range of dopants with just minor modifications to the procedures.

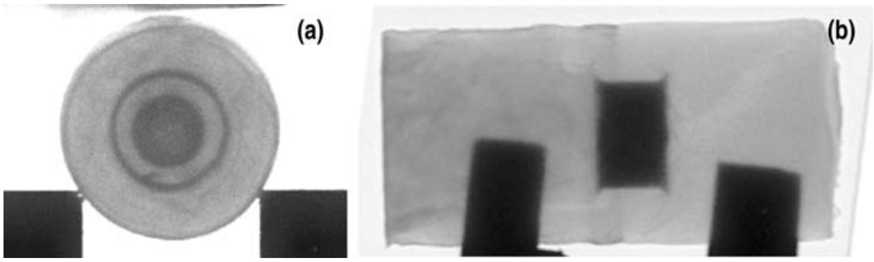

Fig. 3–66. The left radiograph is the length view of the foam with shim and capsule. The right radiograph is the view down the length of the foam. The nominal dimensions are: foam cylinder — 12 mm length, 6 mm o.d., 14 mg/cm^3 density; shim — 6 μm thick, 2 mm length, 3 mm o.d., capsule — 2 mm o.d.

The two doping procedures are quite different. The particulate doping was accomplished by using nanoparticles of the metal, which are distributed throughout the solution. The particles are usually only a few microns in diameter, but agglomerate easily. Our specifications required that all agglomerations be less than 10 μm. We easily met this specification with gold nanoparticles dispersed by a homogenizer as shown in Fig. 3–67.

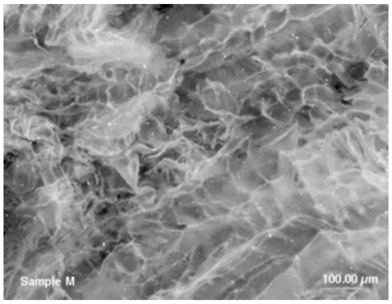

Fig. 3–67. This SEM micrograph shows the gold nanopowder distributed throughout the dried TPX foam. Most of the particles are so large that they must be agglomerations of the nanopowder, but less than the maximum size specification of 10 μm maximum.

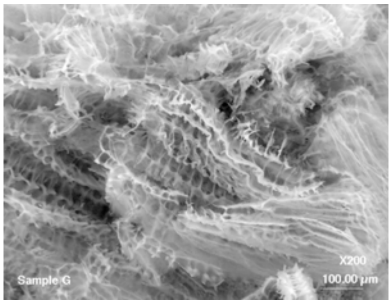

Fig. 3–68. The foam in this SEM is composed of an organometallic Si dopant coating the TPX foam structure. The structure seems somewhat modified from a standard TPX foam with slightly larger cell size. The Si is atomically distributed and particles, agglomeration and other nonuniformities are evident.

The second doping technique uses an organometallic compound (Fig. 3–68). This compound must be soluble in the solvent and have an affinity for the TPX molecule. The advantage of this technique over the particulate doping technique is that the dopant is atomically distributed. The disadvantage is that oxygen is added to the CH foam matrix. This technique had been used by LANL in the past, but the organometallic molecules they used were appropriate for the durene/naphthalene solvent system. They were not appropriate for use in the cyclohexane system.

In summary, the Center for Foam Development and Production continues to add capabilities to its foam production techniques. By building on our unique molding and batch techniques, these new capabilities are added without tremendous additional cost per target. This has allowed us to produce targets unlike those produced anywhere else and to produce them with only a slight increase in funding.

3.7. INERTIAL FUSION CAPSULE PRODUCTION

Center Head: David Steinman (GA)

Technical Group

Supervisor: Martin Hoppe (GA)

Scientist: Salvacion Paguio (GA)

Technicians: Stephen Grant and Ron Andrews (GA)

Deliveries Group

Supervisor: Annette Greenwood (GA)

Scientists: Jane Gibson and Dale Hill (GA)

OVERVIEW

The Center for Inertial Fusion Capsule Production is principally concerned with fabricating and characterizing capsules and components for current ICF experiments. This year, we delivered 117 orders comprising 2461 characterized target-quality capsules to the ICF program. We expanded our capabilities in coating large GDP capsules with both glass and PVA permeation barriers. In glass shells, we acquired a vacuum oven that should allow us to produce “Hoppe glass shells” that contain no residual gases and/or do contain Hi-Z diagnostic gas fills. We developed the capability to deposit tungsten coatings onto glass shells and demonstrated the ability to permeation-fill the composite capsule with deuterium. We developed a “dip, spin and dab” technique to uniformly coat a PVA permeation barrier onto 2-mm GDP capsules and improved upon our characterization methods. In addition, we fabricated a new type of double-shell capsule having a PVA permeation barrier on the inside wall of the outer shell, under very tight time constraints.

Our major effort is the fabrication of plastic capsules and glass capsules for near-term testing, evaluation, and experiments by the ICF laboratories. This section will highlight the wide range of targets that are requested by the ICF laboratories with only a few weeks lead time before delivery is needed.

3.7.1. Fabrication of a New Type of Double-Shell Target with a PVA Inner Layer

The General Atomics Target Fabrication team was tasked in FY03, under its ICF Target Support contract, to make a new type of double-shell target for LLNL. Its specifications called for the outer shell to have an inner lining of PVA that would keep the xenon gas fill from occupying the target wall. The inner shell consisted of a glass shell coated with 2000Å of silver and filled with 9 atm of deuterium. Furthermore, the delivery deadline was less than seven weeks away. The fielding of this double-shell target was made possible through the combined efforts of LLNL and GA target fabrication specialists.

3.7.1.1. Target Design. Figure 3–69 depicts the double-shell target we were tasked to build. The outer CH shell is 1000 μm in diameter, 12 μm thick and lined on the inside with ~1 μm of PVA. The inner shell is glass, 200 μm in diameter, 2 μm thick, filled with ~9 atm of deuterium and coated with 2000Å of silver. The outer shell has a ~250 μm opening to permit insertion of the inner shell, mounted on a ~25 μm tungsten wire. The mounting wire in turn protrudes through a 50 μm hole in a beryllium disk, 250 μm in diameter and 50 μm thick, that seals the opening to the outer shell allowing it to hold 1.5 atm of xenon.

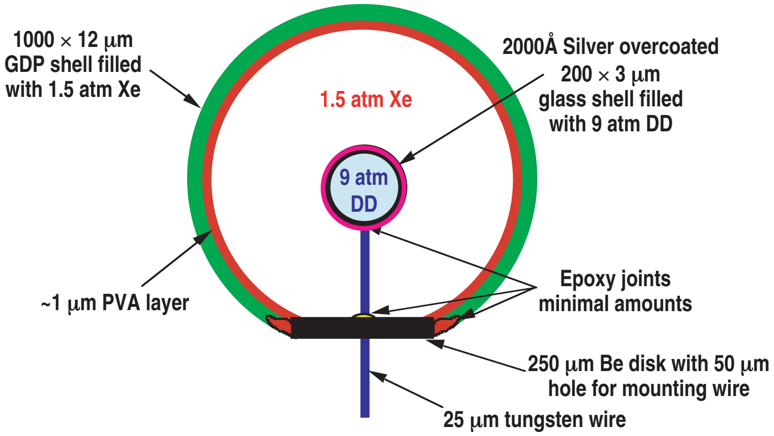

Fig. 3–69. Double-shell target containing an inner lining of PVA.

3.7.1.2. Outer-Shell Fabrication. The outer-shell fabrication plan we devised consisted of the following steps:

1. PVA-coat PAMS shells using drop tower technology.
2. Over-coat the PVA with ~10 μm of GDP (Glow Discharge Polymer).
3. Micromachine a 250 μm hole in the GDP/ PVA/ PAMS shell.
4. Dissolve away the PAMS mandrel with toluene leaving behind a GDP shell lined with PVA on the inside surface.

The outer-shell fabrication process began with the selection from our inventory of a batch of PAMS shells, one millimeter in diameter, made using microencapsulation technology.

We found we had to modify the standard PVA drop tower technique (used to coat 500 μm shells) because the 1 mm shells were still wet when they reached the collection plate at the bottom of the drop tower. We employed two fixes to completely dry the shells as they fell through the 5-m tall tower. First, we turned the tower temperature up to the maximum (145°C), that did not result in the PVA solution “boiling” and forming blisters on the shell. Secondly, we diluted the PVA in the water solution down to 6% from the normal ~10% and added 10% isopropanol to speed up evaporation. These two modifications of the standard drop tower technique enabled us to coat the PAMS shells with ~2 μm of PVA.

We next used bounce pan coating technology to apply the 12 μm thick layer of GDP to the PVA-coated PAMS shells. That operation went routinely.

Micromachining of the hole in the outer shell was done with multishell production in mind. As many as five shells at a time were affixed to a glass coverslip using water-soluble pancake syrup "cement," immediately available and shown to work on its first trial.

The coverslip was held by suction to a fixture on a lathe (see Fig. 3–70). Each shell in turn was centered on the axis of rotation and machined by a diamond tool bit that was brought in contact with the spinning shell, cutting a hole of the desired dimensions

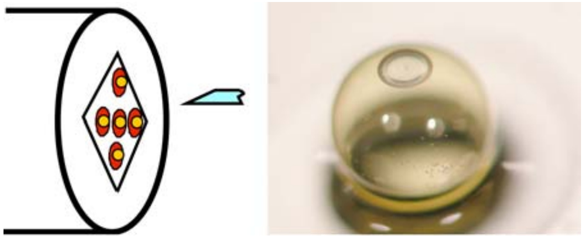

Fig. 3–70. GDP/PVA/PAMS shells were held in place with hardened Aunt Jemima® syrup on a coverslip (held in turn by vacuum on a lathe). After centering one shell at a time on the lathe's axis of rotation, a diamond tipped machining tool cut a 250 μm hole in each shell.

We immersed the coverslip holding the now "open" shells in toluene to dissolve away the PAMS mandrel. The air bubble inside the 1 mm shells prevented toluene from entering the hole. To alleviate this problem, we inserted a fine hypodermic needle into the shell through the opening and used it to admit fresh toluene solution into the shell and to remove the dissolved PAMS. We found that the dissolution process was extremely slow, likely due to the restricted fluid exchange through the small hole in the shell. Using the needle, we flushed the shell repeatedly with toluene, until the shell was PAMS-free, typically within 15 minutes.

The shells now had to be freed from the coverslip by removing the water-soluble "cement" without damaging the PVA layer inside the shell. This had to be accomplished without the water coming in contact with the inside of the shell that would cause the PVA to swell and/or dissolve. We took advantage of the immiscibility and density mismatch of water and toluene. The hypodermic needle was used to place a droplet of water at the bottom of the toluene filled petri dish containing the coverslip. As the density of water was greater than that of toluene, we were able to place the water droplet around the base of the shell where it could dissolve the cement. We used a vacuum pickup tool to remove the water from around the base of the shell and then to remove the shell from the toluene for air drying. Figure 3–71 depicts the process we developed to remove the PAMS from the GDP/PVA outer-shell.

3.7.1.3. Inner-Shell Fabrication. The fabrication of the inner shell required less development than that of the outer-shell. We used interferometric microscopy to cull drop tower glass shells having the desired dimensions from our inventory. We were careful to select a batch of shells that had good gas retention characteristics because of our concern that the shells might become hot during the silver deposition process and, as a result, lose their deuterium gas fill. We permeation-filled the glass shells with deuterium and sent them to LLNL for silver coating.

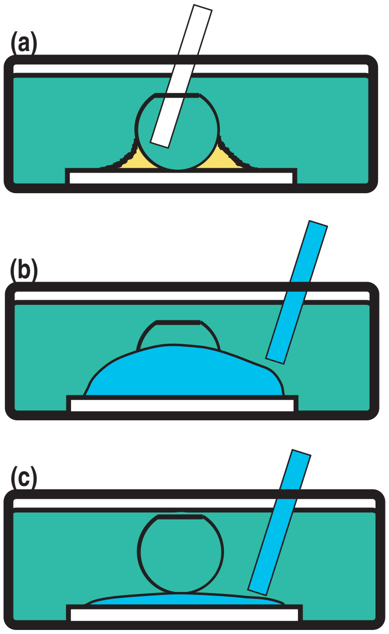

Fig. 3–71. Process used for removing the PAMS mandrel from the final GDP/PVA shell and freeing it from the glass coverslip. (a) Step 1: Removing the PAMS inner mandrel by dissolution in toluene using a hypodermic needle to repeatedly flush out the solution. (b) Step 2: Dissolving away the syrup "cement" by injecting water into the less dense and immiscible toluene so that the PVA inside the shell does not come in contact with the water. (c) Step 3: Suctioning away the water prior to removing and drying the shell.

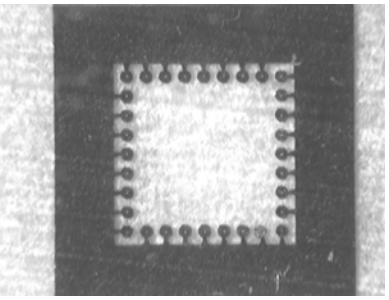

Fig. 3–72. LLNL fabricated numerous 250 μm disks, each containing a 50 μm hole, by laser machining the 50 μm thick beryllium flat pictured above.

LLNL target fabricators found that the small 200 μm shells were prone to being lost in their bounce pan silver-deposition system. To assuage this problem, they immobilized the shells on a tacky polymeric substrate and silver-coated them on one side then manually turned them over and coated the other side. Upon their return to GA, we determined the fill pressure of one of the silver-coated shells by breaking it in a chamber of known volume, measuring the resultant pressure rise and calculating the shell pressure, knowing the shell's diameter. That measurement came in close to 9 atm, indicating that there was no significant deuterium loss due to heating during the silver deposition.

3.7.1.4. Beryllium Disk Fabrication. The fabrication of the beryllium disk "plug" was also done at LLNL. A 50 μm thick beryllium flat, several millimeters square, was laser machined to produce the disks. Figure 3–72 shows the beryllium flat with disks still attached.

3.7.1.5. Target Assembly. The target assembly was very intricate. A drawn glass capillary tube served as the double-shell mounting post to which we epoxied a millimeter long, 30 μm thick, tungsten wire. The wire was threaded through the hole in the beryllium disk and epoxy was applied such that the appropriate length of wire would support the inner shell within the outer shell. Next, the inner-shell was epoxied to the end of the tungsten wire protruding from the beryllium disk. Finally, the inner-shell was inserted into the outer-shell and the beryllium disk was epoxied to the rim(Fig. 3–73). Optical microscopy using orthogonal views was used to position the components during assembly and to measure the concentricity of the inner shell relative to the outer shell. For all delivered double-shell targets, the center of the inner shell was located within 30 μm of the center of the outer shell which met the requirements of the experimentalist.

We considered applying a layer of PVA around the rim to minimize out-permeation of the xenon through the epoxy glue joint. As that development effort would have jeopardized our delivery deadline, we decided to test the assembly for leakage as it was. We did this testing by permeation filling the targets with 1 atm of xenon at 100°C overnight.

We then used our x-ray fluorescence (XRF) system to measure the quantity of xenon present in the shells immediately after the fill and over the course of 24 h as they out-gassed at room temperature. We found that the targets had fill half-lives on the order of two days duration. After consultation with our LLNL partner, it was decided that this half-life was sufficient for the targets to be fielded.

Fig. 3–73. Double-shell target containing an inner lining of PVA. Fabrication of seven of these first-of-a-kind targets was accomplished in six weeks.

3.7.1.6. Summary. In the time frame of a month, we devised a unique process for lining the inner wall of a CH capsule with PVA for a new type of double-shell target. We had to first find processing conditions that allowed us to use drop tower technology to PVA-coat the larger PAMS shells. Then we had to develop appropriate methods to remove the PAMS mandrel after the drop tower shell was coated with GDP. We fabricated and delivered seven of the new PVA-lined double-shell targets in all, meeting the needs of the experimentalists. The elapsed time from receipt of the request to delivery was six weeks.

3.7.2. Glass Shells from Doped GDP

3.7.2.1. Onsite Support for Mounting of Hoppe Glass Shells. In FY03, we provided target assembly support for LANL, onsite at LLE, for glass shells made by the Hoppe process. Two trips to LLE were made by Dr. Martin Hoppe during which he successfully mounted ~25 DD or DT filled shells (holding up to 10 atm gas pressure) with no shell loses due to breakage. The dimensions of the Hoppe glass shells mounted for LANL were approximately 1100 x 4 μm (o.d. and wall respectively).

In the course of this support work, Martin found ways to simplify the capsule mounting procedure normally used by LLE, tailoring it to the LANL capsules. His modifications resulted in less time spent handling each shell, thereby enhancing efficiency and safety. In addition, Martin trained Joyce Elliot, a LANL scientist, in the shell mounting procedure so that she could also perform that operation in future target campaigns.

3.7.2.2. New Oven for Improved Hoppe Glass Shells. Current production methods for Hoppe glass shells use open air ovens that result in residual gases remaining inside the shells after the final sintering step. This residual gas is ~1/3 atm in total pressure and consists primarily of nitrogen with a small amount of CO_2 and oxygen. Over the past two decades, ICF experimentalists have frequently asked for glass shells that either contain no residual gases and/or are pressurized with diagnostic gases such as Ar or Xe. The elimination of residual gases would enhance target performance while noble gas fills would aid in shot diagnostics.

To fabricate Hoppe glass shells meeting the need described above, we contracted Parr Instruments to customize a commercially available high temperature/pressure reactor vessel for our use. This new "oven" should give us the capability to fabricate either evacuated or noble gas-filled (up to ~3 atm) pure silica glass shells. The oven is equipped with gas ports and pressure gauges that allow us to control the atmospheric composition of the gases inside the oven at all times during the glass conversion process. Using pyrolysis gases composed of only helium and oxygen during the conversion of the silicon-doped GDP to glass will result in glass shells devoid of nitrogen in their interior. Any residual oxygen present in the shell can then be converted to water by heating in a hydrogen atmosphere. The water, being readily permeable at high temperatures through the shell wall, can be easily removed leaving a shell free of entrapped gases. Using this same concept, we also expect to produce capsules containing any of the Noble gases at pressures up to 3 atm.

We received the new oven at the end of FY03 and are in the process of setting it up (Fig. 3–74). The oven is designed to operate at temperatures up to 1100°C and pressures up to 10 atm, at temperature. The oven is equipped with a removable, rotating shaft which will give us a way to gently roll the shells during the glass conversion process, if needed at a future time. This ability to roll the shells may be necessary for some combinations of glass shell diameters and wall thicknesses as minor dimpling has been observed on some of the glass shells made by this process.

3.7.3. PVA-Coating of Multimillimeter Polymer ICF Capsules

While PVA has long been the permeation barrier of choice for polymer ICF capsules, fabricating large diameter capsules (≥1 mm) with PVA coatings that have a high degree of thickness uniformity has proven to be problematic for the ICF community. Though we have improved our capabilities this past year for coating large capsules with PVA, we still have much room for improvement.

The original spin-coating technique was developed for SNL capsule production during FY02. In this method, the vacuum chuck holding the shell is motorized to rapidly spin so that after the shell is dipped and withdrawn from a pool of PVA solution, the droplet of PVA hanging from the shell will redistribute itself upward due to centrifugal force (Fig. 3–75).

Fig. 3–74. The Hoppe glass shell Parr oven is designed to operate at up to 1100˚C and pressures up to 10 atm at temperature.

Fig. 3–75. Droplet of PVA resulting from the original spin-coating technique developed for SNL capsule production.

The spin-coating technique generally resulted in delivery of capsules with PVA layers several microns thicker at some point on the shell relative to another. If the shell is spun too rapidly, the PVA will form a band around the shell's equator that is thick relative to the rest of the shell. Likewise, if the shell is spun too slowly, the PVA can pool at the bottom of the shell. Unfortunately, spinning at intermediate speeds results in a thick band somewhere between the pole and equator.

Using the PVA spin-coating technique as the starting point for FY03 SNL deliveries, we made several improvements. We improved the PVA thickness uniformity by using a slower rotation speed (~200 rpm) coupled with a controlled, slow withdrawal of the capsule from the PVA solution. A fan was also employed to direct a flow of deionized warm air onto the shell reducing the drying time from ~12 minutes down to four. This modified method produced capsules coated with 4±2 μm of PVA at the equator. The slower rotation speed resulted in a thicker PVA layer at the pole but we remedied this problem by immediately touching the wet droplet of PVA hanging from the shell to a piece of wax paper which removed the excess. While we still have room for improvement in applying uniform PVA coatings to large diameter capsules, the new method resulted in the production of capsules having PVA thickness uniformity that varied by 2 to 3 μm compared to the 4 to 6 μm without the "dabbing-off" step. The use of the fan also increased our production efficiency by more than a factor of two.

We also improved our PVA layer characterization capabilities. The method we utilized at the beginning of the year (Fig. 3–76), while effective at determining the PVA layer thickness at many places around the shell, was quite labor intensive. Furthermore, due to their relatively large mass, the capsules would sometimes tend to creep down the Post-it® sticky paper causing measurement difficulties.

We devised an improved characterization method (Fig. 3–77) that allowed us to make faster and more reliable measurements. In this new method, many capsules are positioned in a line on a Post-it® note affixed to a flat glass block. The shells are then sequentially positioned under the interferometric microscope for a top wall thickness measurement of each shell. The line of shells is then manually rolled forward a fixed amount, equating to a given angular rotation, and new top wall thickness measurements are taken. This batch process is over twice as fast as the previous "one-at-a-time" method because many shells can be processed together. It also eliminates the problem of gravity adversely affecting shell orientations during data collection.

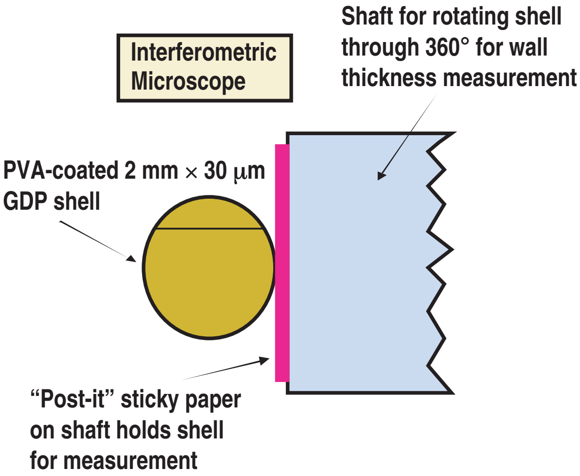

Fig. 3–76. The capsule is mounted on a piece of Post-it® sticky paper affixed to a shaft on a spindle. Rotating the apparatus under an interferometric microscope allows us to measure the wall thickness at many points around the capsule.

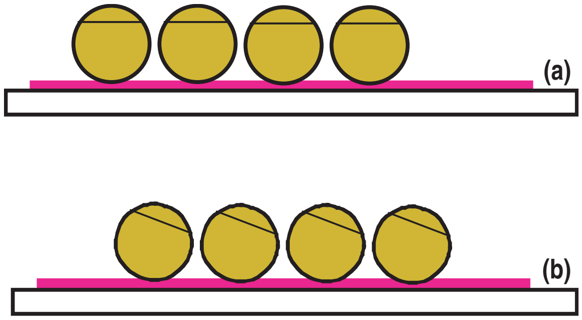

Fig. 3–77. (a) The capsules are lined up on a Post-it® note affixed to a flat glass block where their top wall thicknesses are measured by interferometric microscopy. (b) Each shell is then rolled forward to a new angular orientation and a new set of top wall thicknesses is measured. The "batch" process is repeated, providing wall thickness measurements of the shells from pole to pole.

3.8. ADVANCED PLANAR TARGETS (T. WALSH)

Center Head: Tom Walsh

Scientists: John Varadarajan, Ed Hsieh, Kelly Youngblood

Technicians: Derrick Mathews, Sue Carter, Brian Motta, Pat Collins

A major portion of ICF research involves planar targets. Planar targets are ideal for exploring material properties, hydrodynamic instabilities, and laser-target material interactions. The Nike Laser at the NRL is designed only for experiments using planar targets. The laser's beam is very uniform and well characterized so experimenters can explore the effects of depositing a large amount of energy in a material without perturbations from anomalies in the laser beam. For experiments to have meaningful results, the quality of the targets must at least equal the uniformity of the beam and exceed the limits of the diagnostic equipment. Over the years, as diagnostic equipment and prediction codes have improved, the requirements for target surface finish, uniformity, flatness, and purity have increased. Additionally, the complexity of target designs has increased by the addition of material layers, dopants, intentional surface and mass perturbations, and foams. NRL has also developed a cryogenic capability requiring targets that are designed to work in the wall of a cryogenic Dewar.

Other ICF program lasers also use planar targets in addition to the spherical targets for which they were designed. The OMEGA laser at the UR/LLE is a regular user of GA/Schafer planar targets for laser imprinting studies and Rayleigh-Taylor instability experiments. There are also plans to use planar targets at the NIF located at LLNL when it becomes operational.

We discuss the activities of the Center of Advanced Planar Targets in delivering and developing targets for NRL and UR/LLE, especially:

- Flat CH Films of polystyrene and polyimide as well as Si and Cl-doped CH films.
- Patterned CH Films with a wide range of sine wave periods and amplitudes. This year we made advances in producing large amplitude patterns on polymer films by machining the film directly rather than using a machined mold.
- Coatings of various metals on polymer or polymer foam.
- NRL Foams of a variety of polymer types and densities. This year we developed the capability to routinely produce high and low density resorcinol-formaldehyde (RF) foam and began development of DVB foam, higher density patterned RF foam and patterned CH film-RF foam constructs. We also made foams with a rippled surface.
- Nike EOS Targets which come in several varieties, many of which required intricate assembly schemes due to their complicated designs.

- Characterization of these targets which required new developments in white light interferometry, a scanning surface profilometer, and our home-built ultraviolet (UV) microscope.

3.8.1. NRL and UR/LLE Deliveries

The past year has seen an increased emphasis on more complex targets both for NRL and UR/LLE (Fig. 3–78). A large portion of the targets requested by both labs had a sine wave pattern on one surface with the opposite surface flat.

The sine wave peak-to-valley amplitudes varied from about 0.1 to 5 μm. Periods for the patterns were generally between 20 and 60 μm. Both labs also requested and received flat targets. Targets shipped to NRL during FY03 included targets with patterned surfaces, metal and metal-coated targets, and complex EOS targets in addition to simple smooth-surface flat films. Although the total number of targets shipped in FY03 decreased, the complexity increased (Table 3–2).

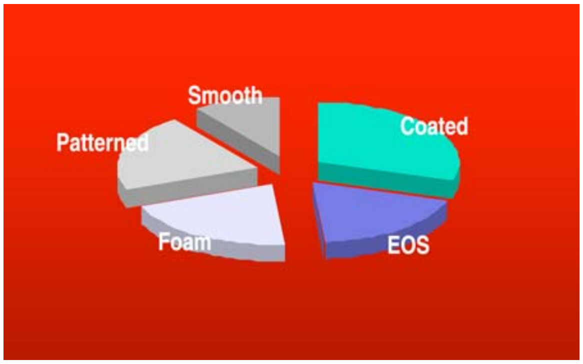

Fig. 3–78. FY03 target mix.

Table 3–2
Total Number of Targets Shipped

Target Type	FY02	FY03
Smooth	208	49
Patterned	74	104
Coated	167	147
Foam	10	99
EOS	70	92
Total	531	491

We also provided NRL with EOS targets consisting of metal or polymer, sometimes with steps, mounted on a cryogenic target mount (CTM). A number of metal targets or metal-coated CH targets (both flat and patterned) filled out the NRL orders for the year.

3.8.2. Flat CH Films

We continue to deliver some classic flat-film polymer targets mounted on polycarbonate frames (Fig. 3–79) to NRL. Nearly all flat-film polymer targets are made with polystyrene that we cast to precise specifications. Target thickness is usually required to be within 1 μm of a nominal thickness that can range from 10 μm to well over 100 μm. The thickness of each target must be uniform over the entire area of interest and must be reported with a precision of 0.1 μm. The surface must be smooth with no accidental perturbations greater than 25Å measured peak to valley. The films must also be very flat when mounted with a maximum of 1 μm of curvature over 1 mm laterally. We are able to consistently produce flat, smooth films by casting polystyrene on a flat substrate, usually a silicon wafer. After the polystyrene dries into a stiff film, it is annealed at 100°C for about two days to remove stresses in the film. We were also able to make silicon and chlorine-doped polymer films.

Many of the targets NRL requires are designed to work in a cryogenic environment. The targets have various configurations, but usually have certain things in common. All the cryogenic targets we made for NRL during FY01 consisted of an aluminum cryogenic target mount (CTM) (Fig. 3–80) and most had a covering of polyimide film.

Fig. 3–79. Nike target frame with gold-coated polymer film target.

The simple polyimide films for the NRL targets have been obtained commercially or spin cast in our laboratory. The films we make are normally 1.5 μm thick, but have been as thin as 50 nm. Thicker films, usually 13 μm, are available commercially. These commercially available films often are not smooth and have imbedded impurities and flaws, but if the requirement is only for a cryogenic pressure seal, they are adequate and less expensive than the high-quality films we make.

Fig. 3–80. Aluminum CTMs have a film of 1.5 μm thick Schafer-made polyimide stretched over them and sealed.

Often, we have been asked to deliver flat CH films that are doped with an impurity. The most common example of this is the silicon-doped CH films we send to UR/LLE. Ideally, these films are made much like we make the normal dopant-free CH films. However, the raw material used to make these films is usually not as suitable for making thin films as the high molecular weight, monodisperse polystyrene we use for the undoped films. As a result, materials such as silicon-doped polystyrene, which we obtain from GA, or polycyclohexyl-methylsilylene $C_7H_{14}Si$ (PCHMS) do not make robust, crack-free films. Because the doped films are usually not as cohesive as pure polystyrene films, we have difficulty lifting them from the casting substrate. We have been successful casting doped films on commercially available salt flats that can be dissolved away after the casting has cured. By the careful choice of the molecular weight of silicon-doped polystyrene and the solvent we have been able to improve the quality of our silicon-doped CH films.

Chlorine-doped CH film was another material we have worked on developing. Since there was no commercial source for the production of the doped material with the specified composition of the dopant, we have extensively investigated the production of the required material by blending pure CH polymers with chlorine-doped CH polymer containing a higher proportion of chlorine, in suitable solvent mixtures to eventually yield the desired film close to the specification.

3.8.3. Patterned CH Films

During FY01, NRL and UR/LLE requested an increased number of polymer films with a sine wave pattern impressed on them (Fig. 3–81). The normal method for making patterned films is to cast the film on a patterned substrate or mold.

We have gotten the best results casting patterned films on molds made of laser-etched fused silica. Fused silica has a very smooth surface, the pattern reproduces well on the film, and the film is easy to separate from the mold after it dries. These molds, however, do have a finite lifetime. After several years of use, we have noticed organic deposits on the molds that cannot be removed by rinsing with solvents. Since target surface finish is critical to the success of many experiments, we do not use mechanical cleaning on these molds. Several times we have had to buy replacement molds for often used combinations of wavelength and amplitude.

As more of our patterned molds became unusable, it became evident that we needed some way to clean them. Consequently, we purchased a plasma asher. The March Instruments PX 250 (Fig. 3–82) has demonstrated an ability to return our silica molds to near new condition. The asher is flexible for use as a research machine as well as for preparing surfaces for sputter or evaporative coating and activating surfaces so that multiple layers of polymers may be cast into one target foil.

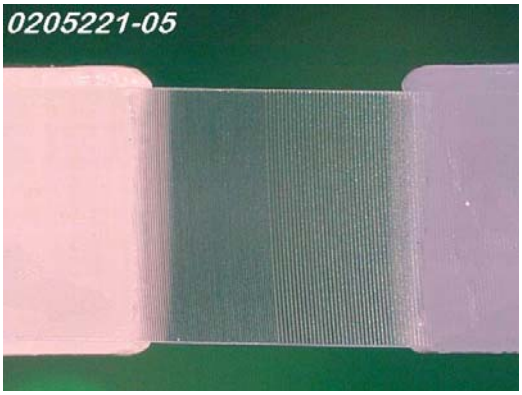

Fig. 3–81. For a NRL experiment, the ridges on a patterned polystyrene film had to be mounted parallel to the edges of the Nike target holder. This target has two different patterns machined side by side.

Fig. 3–82. March Instruments PX 250 Plasma Asher. This machine is used to clean silica molds, prepare surfaces for coating, and conduct materials research.

Both NRL and UR/LLE have also requested a number of patterned targets with larger amplitude perturbations. When the amplitude of the perturbations is above 1 μm, it is easy to machine a casting mold from a ceramic or plastic material such as Delrin. Usually, the surface finish for these targets is not as critical as it is for smooth targets or those with smaller amplitudes so single point diamond turning makes an acceptable surface on plastic. Polystyrene usually casts well on Delrin and can be lifted easily. Sometimes, however, especially with larger amplitude patterns, the polystyrene clings to surface features on the mold and cannot be lifted without tearing the film. To facilitate separating the casting from the mold, we coat the mold with a layer of sodium chloride before we cast (Fig. 3–83). The layer conforms to the shape of the mold's surface so the proper pattern is impressed on the polymer film. Separation is easy because the salt layer dissolves away when the mold with its casting is immersed in water.

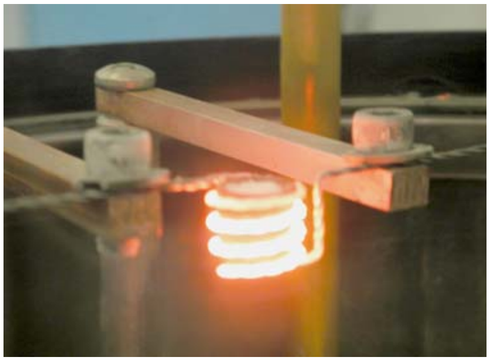

Fig. 3–83. This filament-heated crucible is part of a salt coater used to apply a release layer to some molds before casting.

We have also made patterned substrates of gold, copper, silver, and aluminum blanks using our precision micromachining capability. Unfortunately, it is difficult if not impossible to remove polystyrene from machined metallic molds after casting. We have not attempted to use a salt coating on metallic molds as a release layer, but the technique should work if the salt conforms to the smaller amplitude patterns as well as it does to those of the Delrin molds.

During the past year we have developed a new technique for making patterned polymer foils: machining the pattern directly onto the polymer. We have used this technique on both polystyrene and polyimide with excellent results. Machining a pre-cast foil not only gives us the proper pattern, but we have better control over the thickness of the finished target.

For targets that have patterns with amplitudes less than a micron or so, etched silica still gives the best results. We have a number of silica molds in our inventory and can order more from our supplier. Table 3–3 is a list of the patterned silica substrates currently on hand at Schafer for casting.

3.8.4. Coatings

This year, demand increased for targets made of polymer or foam with a metallic coating. Metal coatings have been primarily aluminum, gold, and palladium. We apply coatings to targets in one of two ways: sputter coating or evaporative coating. Our evaporative coater (Fig. 3–84) can use a variety of tungsten filaments or boats to melt and evaporate most metals. Also we have installed two independent e-beam guns in the chamber to do thick, precision and mixed metallic coatings. The substrate to be coated is mounted above the source. A shutter protects the target from excessive heat and a quartz crystal thickness monitor controls the correct amount of material to be deposited. Even with careful control, the heat radiated from the source is often too much to be absorbed and reradiated by a polymer film, particularly if the film is thin. To protect the film from damage, we mount it on a heat-conducting material.

Sometimes, mounting film on a heat sink for coating is not practical. Additionally, coating layers of metal thinner than 500Å is difficult to control with the precision required for many experiments. In these situations we sputter coat the metal onto the film or foam (Fig. 3–85). The sputtering process can be controlled so that the resultant coating temperature is low enough to keep from damaging polymers. The sputtering coating rate is slower so it is easier to control for thin coatings. We have sputtering targets for Al, Cr, Cu, Au, MG, Pd, Si, Ti and W, and can order more with lead times of about 8 to 10 weeks.

Table 3–3
List of the Patterned Substrates Currently Available at Schafer for Casting

Plate or Design	Surface Function	Period (μm)	Amplitude (μm)
Gnd Quartz #3	Ground with 3 μm grit		
Gentec #01B	Sin(x)	12.0	0.23
Gentec #01C	Sin(x)	12.1	0.28
Gentec #01D	Sin(x)	12.1	0.31
Gentec #06	Sin(x)	20.0	0.25
Gentec #10	Sin(x)	20.0	0.50
Gentec #11	Sin(x)	20.0	1.00
Gentec #08b	Sin(x)	30.0	0.25
Gentec #08a	Sin(x)	30.0	0.26
Gentec #07	Sin(x)	30.0	0.10
Gentec #08	Sin(x)	30.0	0.25
Gentec #09	Sin(x)	30.0	0.50
NPL01	Sin(x)	30.8	0.94
Gentec #03	Sin(x)	60.0	0.10
Gentec #04	Sin(x)	60.0	0.25
Gentec #14	Sin(x)	60.0	0.47
Gentec #15	Sin(x)Sin(y)	20.0	0.23
Gentec #12	Sin(x)Sin(y)	30.0	0.10
Gentec #16	Sin(x)Sin(y)	30.0	0.26
Gentec #13	Sin(x)Sin(y)	60.0	0.10
Gentec #17	Sin(x)Sin(y)	60.0	0.23

Fig. 3–84. The evaporative coater is used primarily for aluminum or gold coatings with thickness greater than 1000Å.

Fig. 3–85. Sputter coating facility at Schafer.

We did salt coatings as a release layer for various applications. Because of the low melting point and high vapor pressure of salts, we do not coat salt in our metallic coating chamber to prevent cross contamination. We have a dedicated salt coating system equipped with shutter and crystal thickness monitor. We can do NaCl, KI and CsI.

3.8.5. NRL Foams

The primary ICF target design for NRL includes low-density foam. In the past, and to some extent now, we provided polyimide-covered CTM to NRL and they would make and mount RF foam to complete the target. During FY01, we developed our own capability to make RF foam targets. Because our foam laboratory is in a clean room environment, the foams and foam targets we make are generally cleaner and of better quality than those made in a chemistry lab at NRL. The techniques we use are those that were developed at NRL and some of the equipment we use was supplied by NRL.

We also made foams with rippled surfaces. We form these foams against a mold of rippled polyimide or a patterned quartz substrate. The foam pattern matches the pattern on the mold fairly well; wavelengths match exactly and amplitudes are about two-thirds the mold amplitude (Fig. 3–86). We are starting work on making patterned foams directly on patterned polyimide that has been stretched onto a CTM. Thus, we will provide targets with flat polyimide and patterned foam, patterned polyimide and flat foam, and finally patterned polyimide with patterned foam.

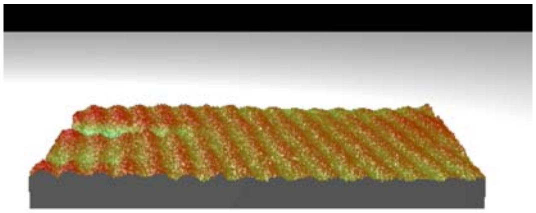

Fig. 3–86. Rippled surface on RF foam.

We were routinely able to produce higher density RF foams (250 mg/cc) with desirable thickness (120–140 μm). We have used these techniques to produce RF foam with sine wave pattern on the surface by single point diamond turning. We have also produced patterned polystyrene film-RF foam (250 mg/cc) targets by directly casting the foam solution on the patterned film. Currently we are developing the process for mounting flat RF foam (100 mg/cc) on flat and patterned polyimide films glued to CTMs.

For making thin target components we are developing DVB foam as an alternative to RF foam. DVB offers a unique combination of pure CH elemental composition, density as low as 10 mg/cm^3, and a cell size approaching a micrometer (Figs. 3–87 and 3–88). It has been easy to produce bulk samples, but difficult to mold due to the very fragile nature of the foams. The combination of low density and small cell size dictates that the walls must be thin. Removing foam from a mold and then handling it often results in the complete destruction of the foam. This is aggravated by nonreproducible properties in foam batches. One batch (shipped to NRL in July) released well and produced very promising AFM traces when analyzed at NRL. Two more recent batches did not release as well and have been difficult to impossible to characterize by AFM. While these difficulties are not unexpected in a new foam system, especially when trying to produce a difficult geometry, the causes are not currently understood and are part of our ongoing research.

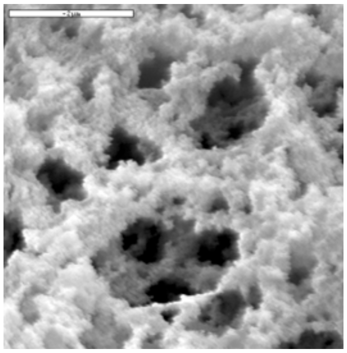

Fig. 3–87. This SEM micrograph shows the cell size and structure of DVB foam. There appears to be very little change in cell size as the density changes.

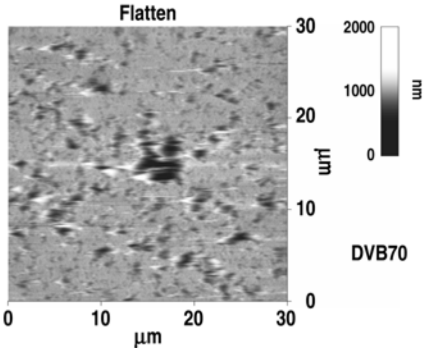

Fig. 3–88. This AFM trace of a DVB foam cast at 70 mg/cm^3 shows an average feature size of approximately 1.5 to 2.5 μm.

Additionally, some DVB foam has been used for wicking experiments with liquid D_2. The preliminary indications are that the foam survives the filling process and fills well but more analysis is required.

3.8.6. NIKE EOS Targets

This year we delivered a new type of EOS target for NRL. These EOS targets consist of a machined 60 μm aluminum plate with a 25 μm step and a pair of aluminum witness strips mounted 60 μm or 100 μm above the plate. The assemblies are mounted on a 13 μm polymer film attached to a CTM.

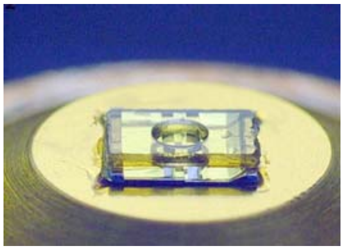

Fig. 3–89. A new type of EOS target for NRL.

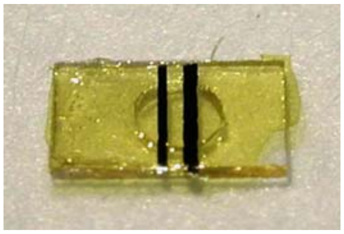

Fig. 3–90. Glass cover slip with a hole drilled in the center supports the aluminum witness stripes.

Figure 3–89 is a photograph of one of these targets. To implement the design, we machine a 60 μm/85 μm thick aluminum plate with 60 or 100 μm high supports on each end, depending on the specification. The support walls are actually curved slightly because the plates are machined on a lathe and cut out from a circular piece. The base plates are attached to a CTM that has a 13 μm thick layer of commercially procured Kapton stretched over it. The aluminum witness stripes must be supported away from the base in order to provide a diagnostic x-ray flash during the experiment when the shock wave reaches them. We support the aluminum with a 6 μm sheet of polyimide with a piece of glass cover slip for stiffening. A hole drilled in the center of the cover slip allows characterization without sacrificing rigidity (Fig. 3–90). The assembled witness plate is fastened to the target in the proper position using the support rails machined into the side of the aluminum base plate.

We also provided other types of EOS targets, some of machined metal and some of polystyrene. The metal targets were mounted on Kapton-covered CTMs or Nike frames and consisted of a piece of aluminum that was machined to a precise thickness. Many of the targets had from one to five precision steps machined into the top surface (Fig. 3–91).

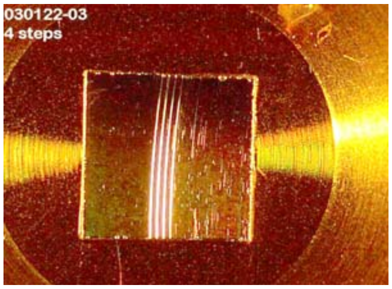

Fig. 3–91. EOS target consisting of a five-level aluminum plate mounted on a Kapton-covered CTM.

3.8.7. Characterization

Making targets to precise specifications is critical to the success of ICF experiments — just as critical is characterizing the targets precisely. We have several methods of characterizing targets and target parts including white light interferometers, laser scattering setups, transmission photometers, optical microscopes, and surface profilometers.

3.8.7.1. White Light Interferometer. Most film thickness characterizations are performed with a white light interferometric microscope (Fig. 3–92). This instrument consists of a Nikon Optiphot microscope with a Michelson interferometer in the objective lens assembly. A mechanical probe measures stage displacement to a precision of better than 0.1 μm.

To measure film thickness, we use one of three techniques. When the thickness must be measured far from an edge and the film is attached to a reflective substrate such as a silicon wafer, we focus the microscope on the surface of the film using the interferometer for precision, and then refocus on the substrate. The thickness of the film is calculated by dividing the displacement measured by the mechanical probe by the index of refraction of the material. If the thickness can be measured near an edge of the film and the film is over a reflective substrate, we focus the microscope on the substrate beside the film and then move the focus to the substrate below the film. Dividing the distance the stage moves by the index of refraction minus one gives the thickness of the film. Incidentally, for films with an unknown index of refraction, measuring the thickness using a combination of the preceding methods allows us to solve for both the thickness of the film and the index of refraction.

Sometimes the film is not attached to a reflective substrate and a third method must be used. In this case, we focus on the top surface of the film and then refocus on the bottom surface. As in the first method, the thickness is calculated by dividing the distance the stage moves during refocusing by the material's index of refraction. This method does not always work, especially with patterned films, because there may not be enough light reflected from the bottom surface of the film to allow precise focusing.

3.8.7.2. Scanning Surface Profilometer. The surface of complex objects can be measured with our scanning surface profilometer (Fig. 3–93). Like the white light interferometer, this machine has an interferometric objective that generates constructive and destructive fringes when the microscope is nearly in focus. The maximum constructive interference (brightest fringe) occurs when the microscope is focused precisely.

Fig. 3–92. By positioning the fringes from this white light interferometer, focus position and therefore film thickness can be measured precisely.

Fig. 3–93. Our Veeco RST–500 scanning surface profilometer is used to measure the surface of complex objects.

The scanning surface profilometer generates a three-dimensional map of a surface by scanning the focus through a preset range, up to 500 μm, and noting the position of maximum constructive interference for each pixel in the CCD. Thus, a planar image is formed of an entire surface with height information for each point on the surface (Fig. 3–94). Because the scanning white light profilometer is very sensitive to vibration, we purchased and installed a vibration isolation system this year (Fig. 3–95). The base of the system has active vibration isolation and the box surrounding the microscope is insulated against acoustic vibrations. This system will allow us to measure all parts more precisely. Additionally, we will be able to measure parts mounted on suspended membranes; an impossible task without acoustic isolation because the noise from the air handling system couples into the membrane.

3.8.7.3. UV Microscope. In order to characterize the uniformity of RF foams, we built a UV microscope. The microscope has a strong UV light source that is aligned below the object to be examined (Fig. 3–96). One of two UV objectives collects light transmitted through the object. A UV-enhanced CCD forms an image of the transmitted light, which can then be analyzed using Interactive Data Language (IDL™) software for data analysis, visualization, and cross-platform application development. This microscope was patterned after a similar machine at NRL. In addition to measuring the optical density of foams, the UV microscope can be used to characterize the uniformity of thin metallic coatings or examine other objects using transmitted light. The system is designed to work with visible light as well as UV.

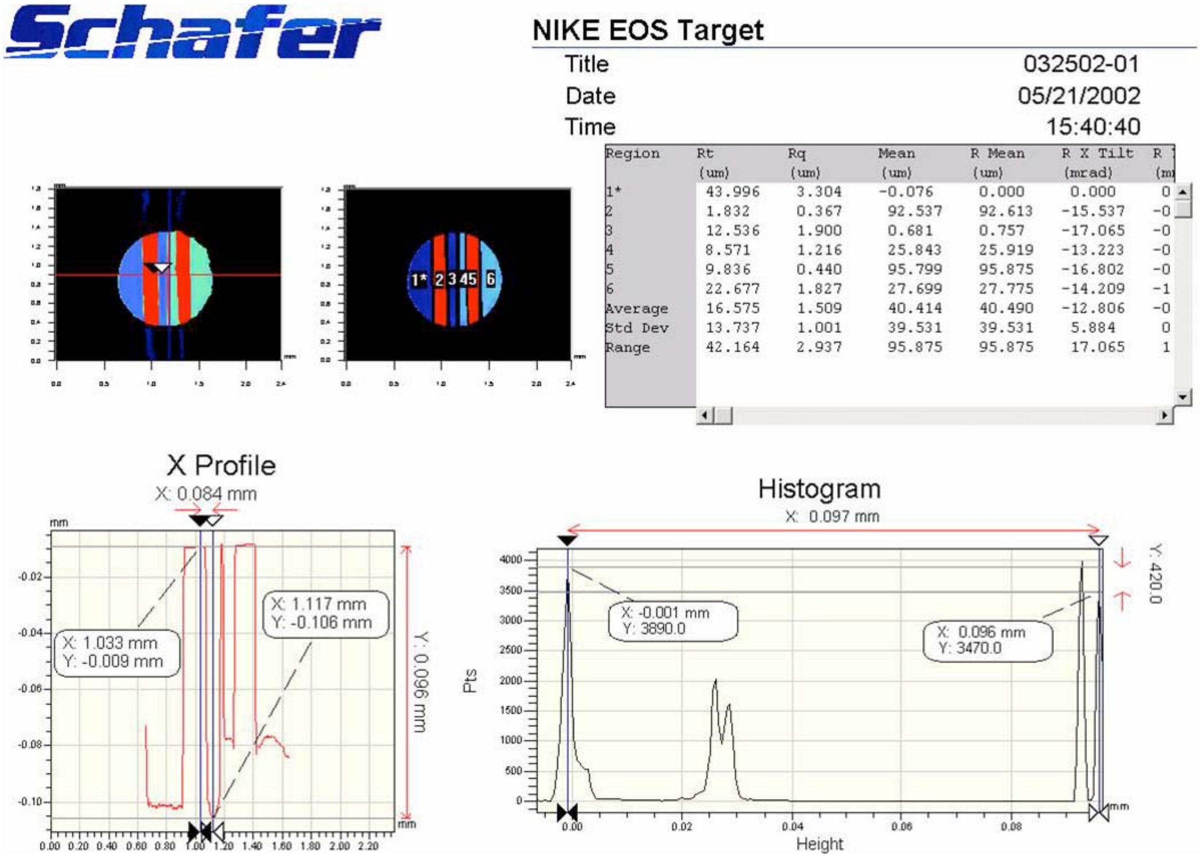

NIKE EOS Target

Title 032502-01
Date 05/21/2002
Time 15:40:40

Region	Rt (um)	Rq (um)	Mean (um)	R Mean (um)	R X Tilt (mrad)	R (m
1*	43.996	3.304	-0.076	0.000	0.000	0
2	1.832	0.367	92.537	92.613	-15.537	-0
3	12.536	1.900	0.681	0.757	-17.065	-0
4	8.571	1.216	25.843	25.919	-13.223	-0
5	9.836	0.440	95.799	95.875	-16.802	-0
6	22.677	1.827	27.699	27.775	-14.209	-1
Average	16.575	1.509	40.414	40.490	-12.806	-0
Std Dev	13.737	1.001	39.531	39.531	5.884	0
Range	42.164	2.937	95.875	95.875	17.065	1

Fig. 3–94. The scanning surface profilometer measures the heights of points over a surface and reports the data in a variety of formats as shown by these characterization results from a foam EOS target.

Fig. 3–95. Vibration isolation system.

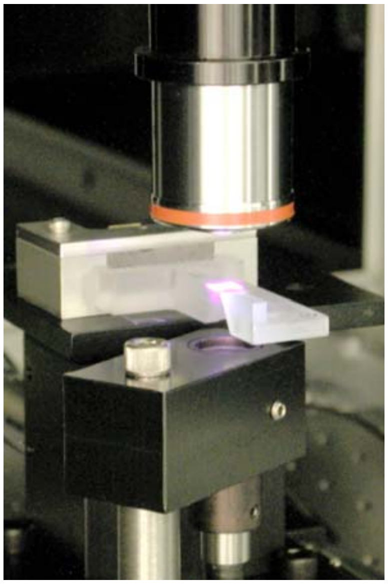

Fig. 3–96. A Nike target is examined by imaging transmitted UV light.

3.9. GA/SCHAFER CHARACTERIZATION INNOVATION AND DEVELOPMENT OFFICE

Office Head: Rich Stephens (GA)

Scientist: Haibo Huang (GA)

OVERVIEW

The characterization innovation and development office is responsible for anticipating and defining new characterization requirements within target fabrication and developing the required capability. The focus of FY03 was to improve productivity through automation in process control and characterization. Three areas of activities are reported here.

3.9.1. Data Logging for Production Control

3.9.1.1. Flame Ionization Detector (FID) for Microencapsulation. The FID (flame ionization detector) measures the fluorobenzene concentration for the 3 to 5 days during which microencapsulation shell batches are under curing. The detector reliably monitors the rate of solvent removal (slow to minimize surface distortion) and indicates the point at which they should transition to a washing cycle (shells sufficiently robust, but debris not irretrievably stuck to the shells). The FID will allow much tighter control of this curing process leading, we hope, to batch optimization and improved repeatability.

For more information, please contact Barry McQuillan.

3.9.1.2. Mass Spectroscopy for Permeation Testing. The output from a mass spectrometer has been set up to allow unattended logging of gas pressure in a permeation cell. The computer can now automatically track chamber temperature to give reliable shell permeation constants, necessary for predicting the gas pressure in a shell at shot time.

For more information, please contact Wes Baugh.

3.9.1.3. Shell Crusher for Retention Testing. The shell crusher, usually used for destructive measurements of the absolute gas pressure inside of shell capsules, can also be used like the permeation tester above. We have also added to this instrument the capability to automatically logging total chamber pressure to increase the reliability of the results and free up the operator for other activities.

For more information, please contact Marty Hoppe.

3.9.2. Spheremapper Coverage Improvement

Modifications of the hardware and software of the GA Spheremapper (SM) extend the mapping range accessible to the AFM head to a band 660 μm wide on a 2 mm diameter shell.

It is now feasible to profile the entire shell surface using five such bands (one equatorial and 4 polar, with 45 deg rotations between the latter). With 30 μm profile spacing, a complete set of profiles (~115 traces) can be collected in less than 3 hours. Registration of the data within each band is excellent, between bands limited by the angular rotation and registration accuracy with which shells can be picked up from and replaced onto the rotating vacuum chuck.

Prior to this improvement, bands of ~30 μm width was used to characterize shell surface, limited by the 4 μm polar-range of the AFM head. It was unsatisfactory as the traces had only a low probability of detecting isolated lumps on the surface (shown as the blue curve in Fig. 3–97). We have taken advantage of a motorized stage that is normally controlled by the AFM controller to implement simple changes that removed this restriction (Fig. 3–98).

First, we added a relay box to allow the SM computer to take control of the stage used for automatic engagement of the AFM head. (The AFM computer is not aware of the loss.) The relay control signal comes from the existing MIO card, and the motor control output comes from a previously unused channel of an existing third-party motor controller.

Second, we modified the polar-translation module in the SM control software to allow the AFM tip to track the curvature of the shell surface. It uses the AFM output as feedback during polar-translations and drives the radially oriented AFM motor as necessary to keep the AFM tip within its PZ range.

The shell continues to rotate during polar-translations. To ensure the new curve is centered in the AFM range, the software uses data from the previously recorded profile to compensate for surface irregularities.

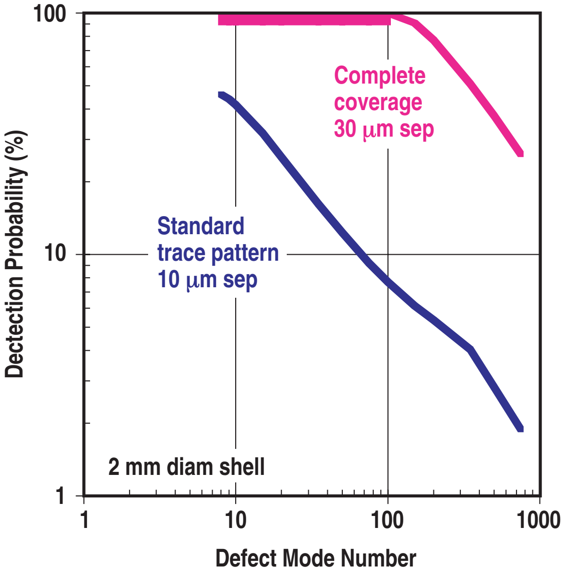

Fig. 3–97. Probability of detecting a single lump versus the mode number of that lump for two different trace patterns.

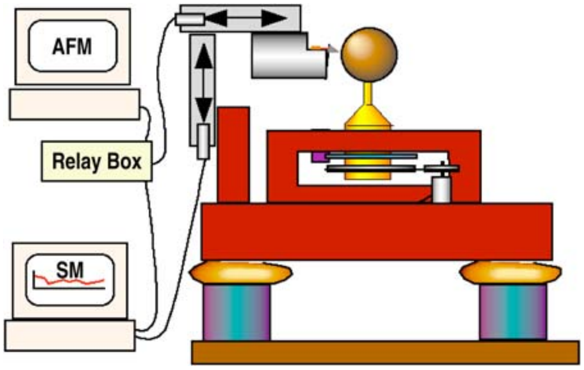

Fig. 3–98. New control arrangement for spheremapper. The added relay box allows the SM computer to take control of a radially oriented motorized stage; software modifications allow the AFM head to follow the curve of the shell surface as it is translated in the polar-direction.

The complete coverage profile set can be used to get a far more reliable representation of the average fluctuation power spectra than before. The traces overlap at the poles and the equator, so those regions are over-weighted (by factors of 4 and 2 respectively), but no area is missed. This data also allows new uses and we have developed several new visualization tools. The bands are in excellent registration and are wide enough (~600 μm) to show the 2-D shape of surface fluctuations with 1:1 aspect ratio (Fig. 3–99); this gives valuable feedback for process improvement. The bands can also be wrapped around a sphere to give a representation of the sphere [Fig. 3–100(a)]. One can see that there are small errors in the registration of the bands. These come from errors in the assumed radius and center of each of the profiles as well as small bobbles in picking up and putting down the shell on the rotating vacuum chuck when changing the rotation axis. These curves can be melded together to get a surface accurate for low modes [Fig. 3–100(b)]. We are currently looking at shell handling improvements and processing algorithms that will eliminate or correct these errors.

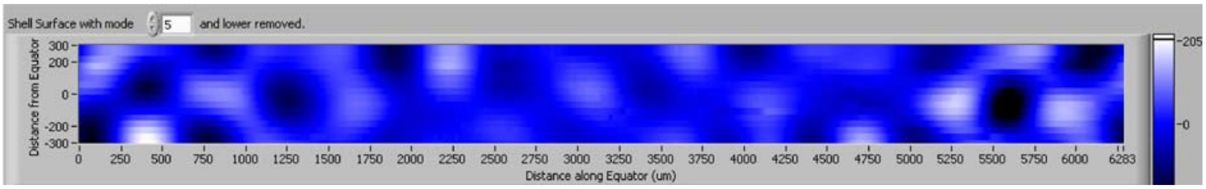

Fig. 3–99. Surface profile with low (<5) modes eliminated. Regular pattern of surface distortions suggest instability driving convection cells during curing. A dominant mode-2 fluctuation made this regularity very hard to detect in an unprocessed display.

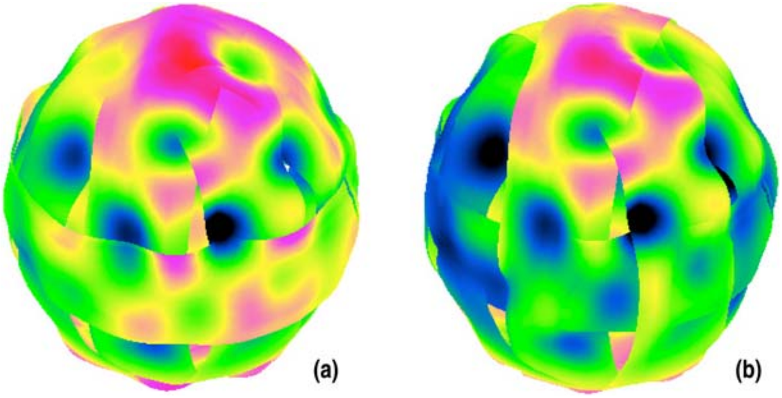

Fig. 3–100. Set of complete coverage profiles (a) combined into bands and wrapped around a sphere and (b) merged into a continuous surface. The color bands span 0.8 μm; the distortions are magnified ~300 times.

We have upgraded over 90% of the sub VIs in the original control software package to keep up with the evolving technologies and to improve instrument control. For example, even a slight touch of the mouse used to cause small angular registration errors in the AFM profile. DAQ activity is now triggered and scan clocked by external counters on DAQ card, which makes the rotary indexer triggered data acquisition largely immune to user/background activities in the computer operation system.

For more information, please contact Haibo Huang.

3.9.3. Spheremapper Noise Reduction

After we replaced our Spheremapper's obsolete Atomic Force Microscope with a newer model from Digital Instruments (Bioscope) we discovered that the noise level (fluctuations measured with the AFM tip on an unrotating shell) was unacceptably high. Figure 3–101 shows three consecutive noise tests and their average. You can see that the noise level was too close to the NIF specification to be acceptable.

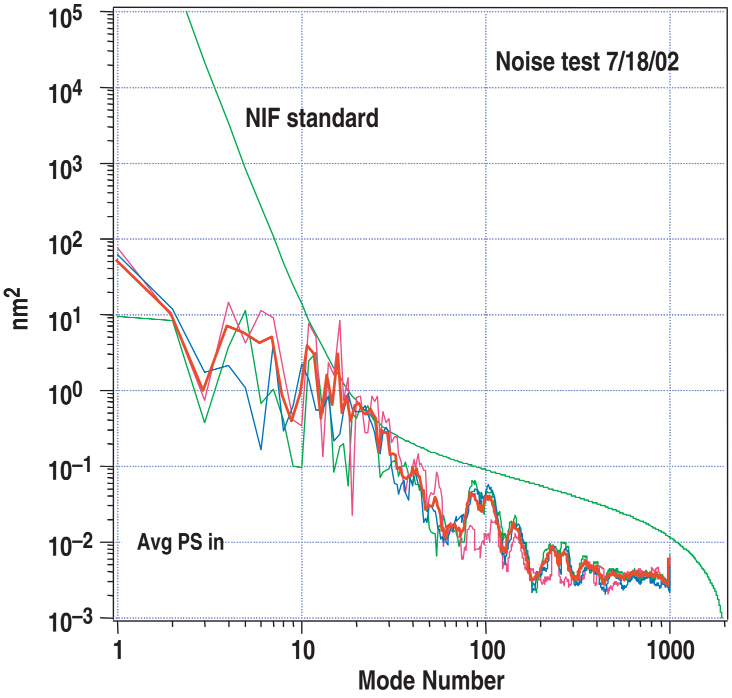

Fig. 3–101. Three consecutive noise tests and their average after replacing the AFM head with a new one. The noise level was near the NIF specification which was unacceptable.

We then performed numerous experiments to identify and minimize sources of noise.

We noticed the AFM was more stable early in the morning before the air conditioning turned on. Covering the AFM table with a tent fashioned from plastic sheeting improved the noise at mode 10 by an order of magnitude. Now we routinely have the tent in place while we are taking data. It is easy to roll back while we are accessing the shell or centering the rotating vacuum chuck.

We also optimized the gain settings in the AFM controlling software resulting in significant further noise reduction. We found new gain settings for the AFM that reduced the noise on our system to the level that the manufacturer (Digital Instruments) measured on one of their in-house atomic force microscopes under optimum conditions (see Fig. 3–102).

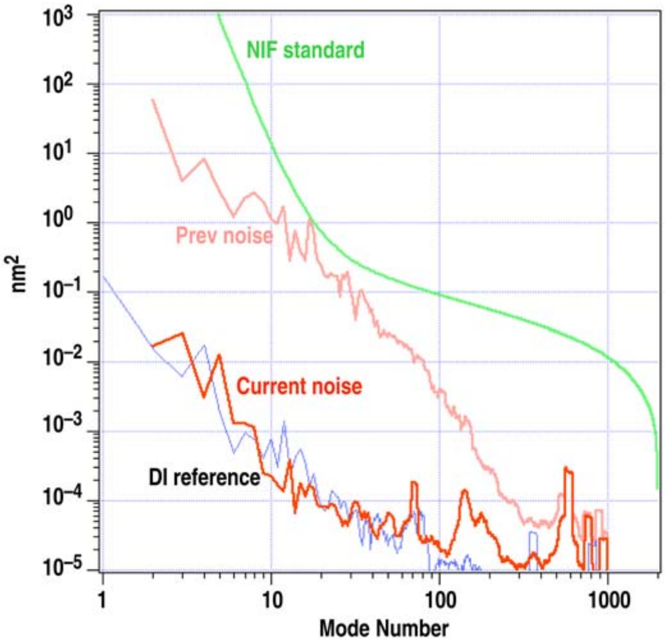

Fig. 3–102. Digital Instruments' in-house reference noise spectrum, current noise spectrum on GA's AFM, and previous noise spectrum. The noise power was reduced by more than 3 orders of magnitude.

The result of this effort has been to reduce the noise power by more than three orders of magnitude, much less than it was even before the system upgrade, and close to the noise exhibited by a DI instrument measuring a surface on a granite slab.

For more information, please contact J. Gibson.

3.9.4. Automicroscope Capability

The NEXIV VMR Nikon microscope has been programmed for automated batch characterization of a wide range of shells. The performance was carefully adjusted and evaluated, and inter-calibrated with the other shell characterization techniques used in the lab. It can be operated at two levels of precision: **detailed** and **quick**. The former requires 15 minutes to fully characterize a batch of (~20) shells (diameter, circularity, and out-of-round of the outside and inside surfaces, non-concentricity, wall thickness, and wall thickness variation). The latter requires only 1 minute to characterize a batch of shells (outside surface diameter and circularity). In either mode, the resulting data are reported as individual measurements for each shell, the batch average, and the standard deviation of those averages.

These results depend on two hardware improvements and development of a suite of measurement scripts. The hardware changes were vital, but relatively simple. The previously reported asymmetric illumination problem was eliminated by re-alignment of internal circular polarizers, and self-aligned shell arrays are formed on a grid of small drilled holes (0.5 to 0.7 of the shell diameter) on a plastic Petri dish instead of the liquid drops on hydrophilic dots. Drying and potential surface contamination is therefore eliminated.

The quality of these measurements has been subjected to intensive scrutiny. We find they are very robust for OD, ID and Wall thickness measurements, but are slightly different than measurements by the other techniques used in our lab. The differences (0.1% to 1%) are explainable by the physics of the different measurements, and have been incorporated in the measurement scripts and data reports. Table 3–4 shows the repeatability of measurements. We have found a software problem with the elliptical fit routine. It sometimes (most frequently on the outside surface of NIF-sized shells) leads to a grossly erroneous OOR result. We are working with Nikon to resolve this problem.

Table 3–4
Repeatability of Measurements for NIF, OMEGA, and Nova Shell Sizes

Repeatability (μm) ⇒ Parameter	**NIF (2000 μm)**	**OMEGA (850 μm)**	**Nova (400 μm)**
o.d. (Detailed or Quick)	0.4	0.1	0.1
Batch St. Dev. o.d. (Detailed or Quick)	0.2	0.1	0.1
Circularity-Exterior (Detailed and Quick)	0.2	0.2	0.1
OOR-Exterior (Detailed)	Varies(a)	Varies(a)	Varies(a)
i.d. (Detailed)	0.4	0.1	0.1
Batch St. Dev. i.d. (Detailed)	0.2	0.1	0.1
Circularity-Interior (Detailed)	0.2	0.1	0.1
OOR-Interior (Detailed)	0.2(b)	0.2(b)	0.2(b)
NC (Detailed)	0.2	0.1	0.1
Wall (Detailed)	0.2	0.1	0.1
4π W (Detailed)	0.2	0.2	0.2

(a)Do not use.
(b)Use with caution.

Among the three types of shells, the OMEGA shells are by far the easiest to measure because of their usually pristine surface and the ease of handling. The NIF shells are very easy to handle, but are susceptible to the OOR problem discussed above. The Nova shells are very easy to measure, but painstaking to mount onto the array because the shells are too light-weight and stick to the vacuum wand. Simply degreasing the needle tip and ionizing the area are not sufficient to overcome static problem. One must use a particularly small needle with a beveled tip to release these shells by gently nudging on the array substrate.

For more information, please contact Haibo Huang.

3.10. OPERATIONS OFFICE FOR SCHAFER DIVISION OF INERTIAL FUSION TECHNOLOGY

Director and Head of Operations: Keith Shillito (Schafer)

Target Fabrication Technicians: Ron Perea, Craig Rivers, Chris Bostick, Steve Gross

Overview

The Operations Office at Schafer's Livermore Laboratory is responsible for budgets, reporting, task coordination and personnel management for all activities related to Schafer's role in the ICF target fabrication program. It also serves as the link for those people who work on-site at LANL and LLNL under laboratory supervision. The work of our LLNL on-site employees is covered in Section 3.11.1.

3.10.1. On-Site Support at LANL

During FY03, Ron Perea built over 1200 targets for the Trident Laser Facility. He has built targets, including numerous flyer plates that were involved in "experimental reinvestigations" for a different LANL experimenter who repeated numerous shots from the previous year (GFY02).

Laser-launched flyer plates are being developed to accelerate a 1-D plate to high velocities (100 to 1000 m/s) to impact 1-D targets as depicted in Fig. 3–103. By recording the free surface of the shocked target, the dynamic response of the target to shock waves and release waves can be understood. This data is of importance for weapon programs, ICF target designs, and basic material properties. These on-going experiments have been conducted at the Los Alamos Trident laser to study shock propagation and spall properties of materials depicted below (Fig. 3–104). These experiments are for the purpose of making the necessary preparations to perform experimental campaigns to study the material spall properties of Pu. The experiments involve laser-launched flyer plates where a high velocity flyer plate impacts a target material sample. An optically based diagnostic measures the response of the target material sample as it is impacted by the flyer plate. Components have been developed and fabricated for flyer plate assemblies as well as the target material samples. Fabrication of the flyer plate assemblies begins with a BK-7 glass substrate onto which is deposited 0.5 mm C, 0.5 mm Al and 0.5 mm Al_2O_3 layer. Onto these deposited layers is glued a 250 mm Au plasma shield. Onto the plasma shield is bonded a flyer plate disk (5 to 8 mm diam.) with thicknesses in the range of 500 to 1200 mm. Flyer plates are diamond turned Au. Fixturing and tooling that was needed to bond these components together in a very flat configuration have been developed and demonstrated. Perea employed a metrology method for the flyer plates that involves simultaneous measurement of the upper and lower surface of the flyer plate using confocal lasers. This measurement provides the flyer plate thickness as well as the upper and lower surface profile. Such a measurement is necessary in order to confirm that the flyer plate meets the required specifications of uniform thickness and overall flatness. After the flyer plate is glued down, WYKO measurements are

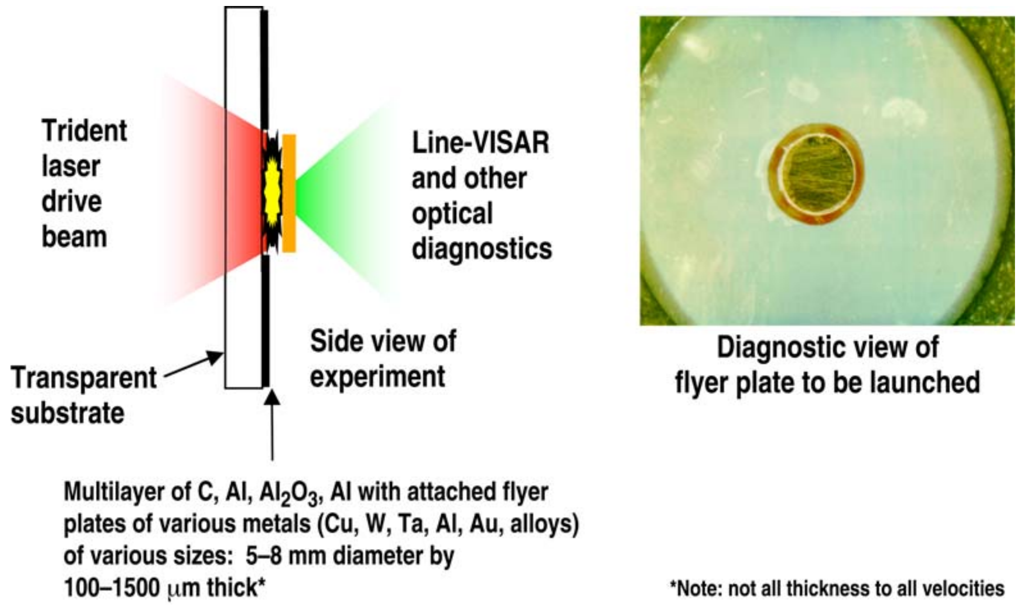

Fig. 3–103. The Trident laser can launch 1-D flyer plates of various thickness (2 to 1500 μm) and velocity (0.1 to 5 km/s).

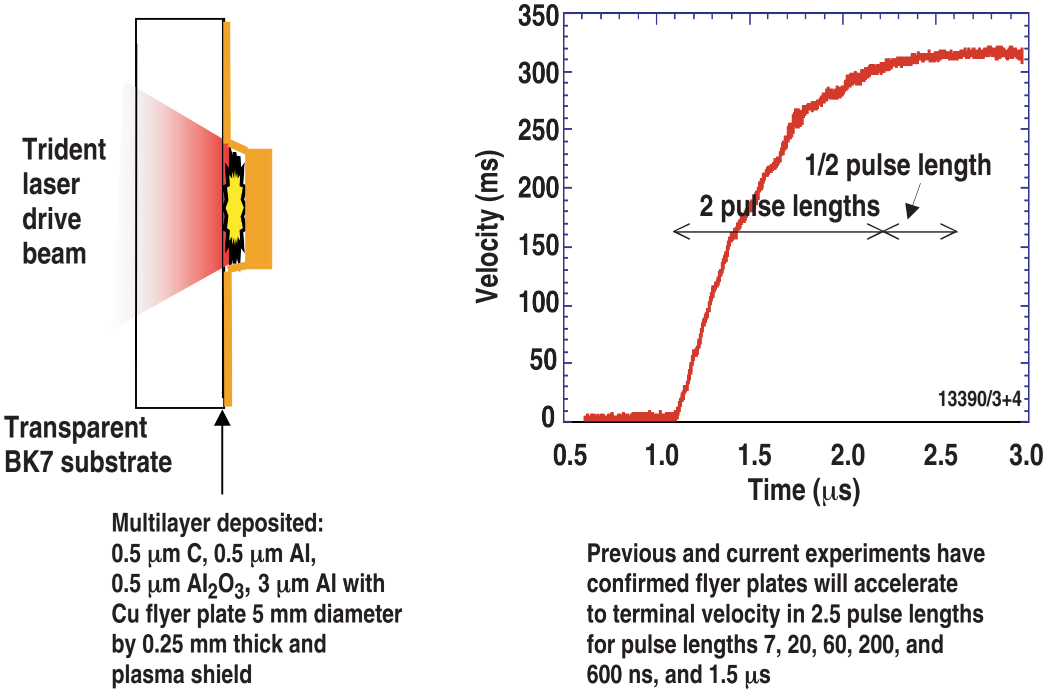

Fig. 3–104. Trident experiments will use laser-launched flyer plates to collect spall data.

made of the overall flyer plate assembly thickness profile. The target material samples were cylindrical samples that consisted of an inner cylinder that is press fit into an outer cylinder. These components were successfully used in experiments to demonstrate the measurement of material spall on non-radioactive components (Au). Experiments planned for the near future (hopefully before January 2004) will use these components to study the material spall properties of Pu. Fabrication of substrates and flyer plates with precision and accuracy is required for quality experimental data. The quality of the flyer plates and targets determine the shot-to-shot variation.

3.10.2. On-Site Support at SNL

The on-site support task at SNL saw three very significant changes in FY03. First the target requests were exceedingly much more demanding. This was due to the increased complexity of the targets and due to the increased characterization required. The second change was the initiation and successful registration of our processes to the ISO 9001 standard. The third change was a significant change in personnel. Each of these changes will be described individually.

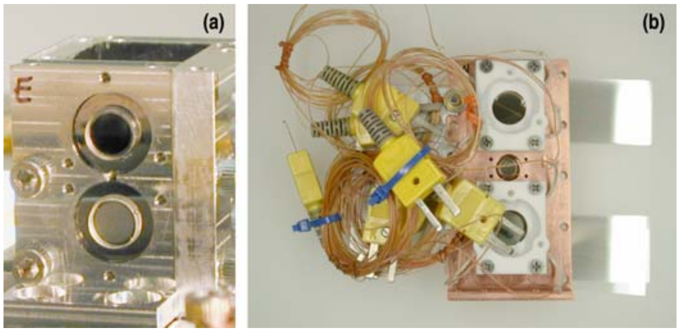

Fig. 3–105. (a) A typical EOS panel assembled in FY01. (b) A preheated material EOS panel assembled in FY03. There are four panels per experiment.

The increase in the workload due to the complexity of the targets and increased documentation needs is easy to see. Double Pinch Hohlraums in FY03 required Be liners in the apertures, gold foil around the apertures, foam tamping between the primary and secondary hohlraums, large gas filled capsules and tighter assembly tolerances. Equation-of-state targets in FY01 were simple shock breakout experiments. In FY03, EOS targets were measuring isentropic compression in preheated metals, or the opposite — cryogenically cooled materials, and hazardous materials such as irradiated stainless steel and depleted uranium (Fig. 3–105). As the complexity of the experiments increased, the number of parts and difficulty of assembly increased since the assembled parts has to be parallel with known distances from each other. The characterization needed included confocal and interference microscopy and Veeco profilometry at various steps during assembly. Dynamic Hohlraum targets in FY03 required foams with embedded capsules, capsules and shims, and doped foams (see Section 3.6.) The additional characterization required by these complex targets required a redesign of the radiography system to allow more foams to be analyzed at once and for each target to be individually rotated. This new system has been designed and components manufactured.

The second change was the initiation of the ISO 9001 system. This change was undertaken because of the increase in workload. As each type of target became more complex, it became increasingly difficult to track all of the required steps and ensure that they were being carried out reproducibly from target to target. To comply with the ISO system, we wrote procedures, created forms and instituted an electronic work order system to track all requirements and changes. Another requirement of the standard is to obtain customer feedback. This is was a very important component of our system. We are pleased to report that the Target Fabrication Lab at SNL was registered on January 31, 2003, and passed its six-month review in July of 2003.

The third major change was a significant turnover in personnel. Three individuals left the group: a SNL student intern, a SNL target assembler, and Dave Tanner the Schafer assembler. This left the on-site task without documentation support and any dedicated assembler. We are pleased to report that in spite of this, assembly continued on schedule and all targets were all delivered on time. This was due to the ISO 9001 system being in place, with its documented processes and work order requirements, and the willingness of the remaining members of the group to take on any needed function. The missing assemblers have now been replaced, but it is a testimony to the group that during the transition time we received customer feedback indicating that over 90% of the time we did an excellent job (the highest category in our four level ranking system) meeting their requests.

In summary, FY03 was a very interesting and successful year for the on-site task at SNL. We have risen to the challenges of increasing complexity in target assembly and characterization and raised our own professionalism by obtaining ISO 9001 registration. The result is a very cohesive team ready to aggressively meet the needs of the experiments in FY04.

3.10.3. Aerogel Technology Transfer to LANL

In GFY03 Schafer was tasked to transfer technology to synthesize aerogel materials from Ocellus, Inc. (sub-contractor to Schafer) to LANL. Keith Shillito worked with Mike Droege of Ocellus to transfer the existent aerogel expertise at Ocellus to LANL. Ocellus provided support for the design of a LANL apparatus in which to synthesize aerogel, and advise in the operation of the equipment to produce aerogel material.

During the course of the year pressure vessel and closure designs and hardware were reviewed and preliminary system designs and physical layouts for the equipment offered by LANL were reviewed and critiqued. Vessel design modifications were collaboratively updated with Ocellus and LANL and the vendor. High pressure metering valve options were reviewed and a valve supplied by LANL was tested at Ocellus' laboratory leading to suggestions in design changes to the metering valve. At the request of LANL a hazards plan and pressure safety analysis was prepared, reviewed and accepted by LANL.

An aerogel synthesis Operational Procedures Document was written for LANL and delivered for the aerogel system. Foam synthesis and process training for LANL personnel was conducted at Ocellus using their existing equipment. The LANL equipment designs were evaluated and updated, hardware was specified with vendor selections, and equipment purchase orders were produced for the supercritical fluid drying system needed to process aerogel foams. Upon receipt of all the hardware, Ocellus will assemble and checkout the equipment, train LANL personnel in its use, ship it to LANL, reassemble and verify operational status at LANL. This will all occur in GFY04.

3.11. OPERATIONS

Operations Office Head: Wayne Miller

On-Site Target Fabrication at LLNL

Project Leader: Russell Wallace (LLNL)

Target Fabrication Technicians: Chris Bostick, Steven Gross, Craig Rivers (Schafer), and John Ruppe (GA)

Overview

The Operations Office supports the division in carrying out program activities, in supporting and monitoring the Division of IFT to help ensure customer satisfaction. The Operations Office also provides administrative support for on-site target fabrication technicians stationed at LLNL. (Technical direction is provided by the LLNL project leader.) The Operations Office is described in Section 4.3.11.

3.11.1. On-Site Support at LLNL (W. Miller; writing contributed by John Ruppe)

Most of our on-site LLNL support consists of micromachining and characterizing target components and then assembling these components into a major portion of the completed targets that are used for LLNL experiments at UR/LLE's OMEGA facility. In so doing, we produce targets incorporating parts that vary over a wide range of materials, shapes, thicknesses, and sizes. This year, for the first time, a substantial effort was also put into providing targets for the initial campaigns on LLNL's new mega-joule NIF laser facility. We will discuss these first NIF targets and touch upon some representative types of our targets currently being fielded at OMEGA.

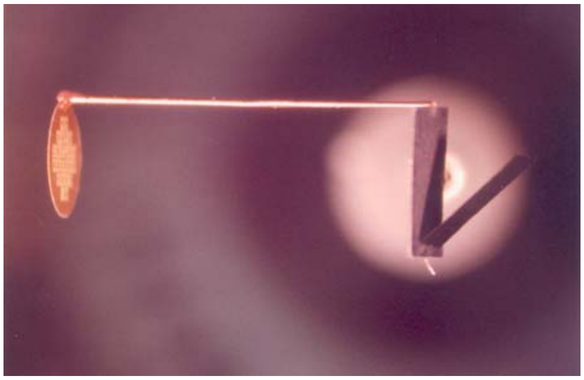

Fig. 3–106. An example of an alignment aid target for initial NIF shots. Alignment aid targets consist of specifically oriented combinations of lettered grids, pinholes, and backlighters.

The first targets supplied to NIF were alignment aids, ranging from simple mounted gold disks to more complex assemblies composed of various combinations of specifically oriented letter grids, backlighters, and/or pinhole arrays (Fig. 3–106). The first "real" targets shot in a campaign using the first four beams of NIF to become operational were of the gasbag and gas pipe type. The gasbag targets were of the same type as had been used for many years previously on LLNL's former primary laser, Nova. Twenty-seven of these were made and shot essentially as diagnostic check-outs and to test the comparability of NIF and Nova results using virtually identical targets.

The gas pipes, however, with an inner diameter of 4.1 mm and lengths, depending on type, of either 4.0 or 6.9 mm were considerably larger than gas hohlraums shot on previous laser systems (Fig. 3–107). Gas pipes of this size and volume can only be shot on NIF, since the power of the four of its beams now operational provide laser geometries that exceed the power that could be gotten from similar geometries at other laser systems currently in use in the national ICF program. Shooting these larger gas pipes allowed for considerably longer observations to be made upon, and more data to be gathered about, certain laser-plasma interactions than had been possible when lesser laser power necessitated shooting smaller volume targets.

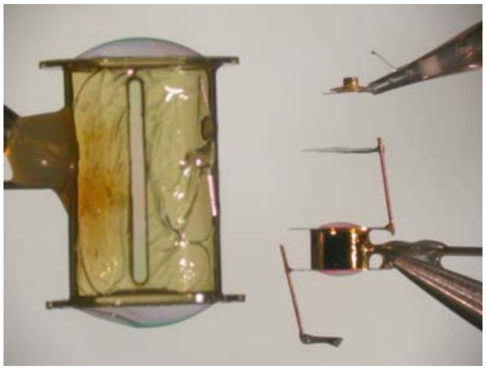

Fig. 3–107. The difference in size is here demonstrated between a NIF-sized gas pipe target (at left) and two standard-sized OMEGA targets. At lower right is an OMEGA gas hohlraum, while at upper right is a high-temperature target incorporating a 400 μm diameter by 400 μm long "top-hat" hohlraum. (The wavy appearance at the front of the 7000 x 4000 μm NIF hohlraum is caused by a layer of glue holding a polyimide film over the central diagnostic slot).

Fig. 3–108. A gas pipe target is a transparent epoxy hohlraum with thin polyimide windows and filled with a specified gas or gas mixture.

The mandrels for these large-sized hohlraums were machined at GA, where they were subsequently coated with an epoxy, then machined again to leave a top epoxy layer 100 μm thick over the mandrel's main body and 200 μm thick over the flange at the laser entrance holes (LEHs). The coated mandrels were then sent to LLNL where, after heat-treating, the mandrels were etched away, leaving behind the large transparent epoxy pipe bodies (Fig. 3–108). These were then sent to an outside vendor where, over the LEH flanges (and in a few instances, over a side diagnostic slot) were glued polyimide windows thin enough to provide minimal obstruction to entering laser beams but strong enough to seal and enclose the volume of gas specified to be in the target at the time of shooting. Upon return to LLNL, the pipes were incorporated into the target assembly design specified by NIF experimenters and returned to the micromachining group for leak testing. If leaks were found, efforts were made to pinpoint their locations and microassembly personnel would strive to seal them. Once sealed, a pipe-film assembly was set aside until it was requested by NIF for an impending shot, at which time it would be filled to a precise pressure with a previously prepared gas fill of neo-pentane, carbon dioxide, argon, xenon, or a mixture of these gasses. Fifteen such large gas pipes were qualified to be shot.

While it is expected that making targets for NIF will be claiming larger and larger percentages of our efforts in the years to come, targets made for OMEGA still constitute the major portion of our production. Much of the novelty in OMEGA targets from year to year appears in the form of significant evolutions of, or modifications to, basic elements in an existing target design. More often than not, such changes add some degree of difficulty to the assembly task. Figure 3–109 pictures a target nearly identical in the shapes and placements of its three elements (pinhole slot, capsule, backlighter) to a target shown in last year's review [General Atomics Report GA–A24147 (2003) p. 3–90, Fig. 3–112] as an example of how a simple-looking target could be made quite complex to assemble by having exacting specifications as to the ways (orientations, angles, distances) in which its elements must relate to one another. The target's new feature this year involved replacing the single shell with a shell mounted within a second, larger shell. The inner shell is mounted on the end of a 25 μm diameter tungsten wire that has been run up through the hollow glass target stem support and then through a 50 μm hole in the 500 μm diameter beryllium disc, which serves as a platform on which the larger shell is then placed. (A section of the larger sphere has been machined off to nearly match the diameter of the disc where the former rests upon the latter.) The wire had been run up through the disc hole to a calculated height such that, when mounted upon it, the smaller sphere would be concentric with the larger (had a section of the larger not been machined away) [Fig. 3–110(c)]. Two sets of these shell-in-shell assemblies were delivered to LLNL for inclusion in OMEGA targets. The first set had considerably smaller and lighter (200 μm diam, 3 μm wall thickness) inner shells than those pictured here. All members of this set were intact and survived the journey from San Diego to Livermore, California, and from there across country to Rochester, New York. The second set, with larger and heavier (570 μm diam, 40 μm wall thickness) inner shells, did not fare a s well at first. Between San Diego and Livermore, several of these inner shells lost their grip on their precarious perch and began to freely rattle around inside the outer shell. When this happened, the situation was saved by carefully dissolving the glue bond between the outer shell and the beryllium disc and lifting off the outer shell. The inner shell was then remounted on its wire support with an epoxy-uv glue mixture that was sturdier than had been necessary for the smaller inner shells in the previous batch. The outer shell was then replaced over the inner, glued in place, and the target sent on its way (Fig. 3–110). All targets,

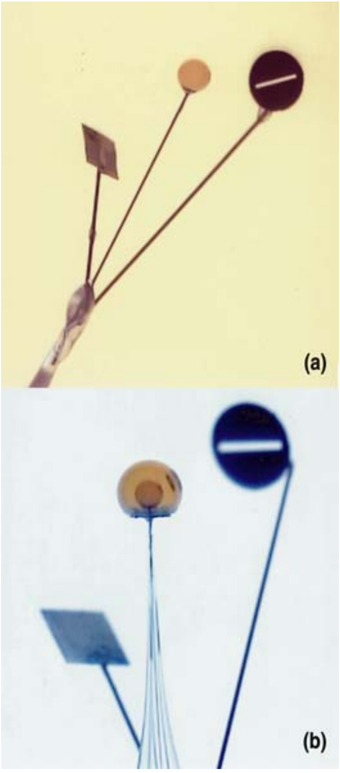

Fig. 3–109. (a) A target from FY02. The complexity of the interrelated angles and distances specified (e.g., slot at 54 deg to target support within substrate tilted 10.8 deg to vertical axis at line of sight distance of 4000 μm from slot center to center of capsule) provided a high level of difficulty in assembling this seemingly simple target consisting of a GA PVA-coated GDP capsule, a backlighter, and a pinhole slot. (b) The latest FY03 version of this backlighter-sphere-slot target substitutes a shell-within-shell component for the previous simple sphere.

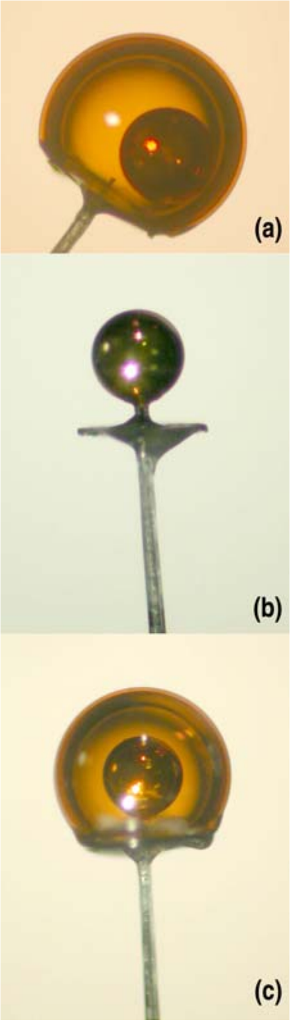

Fig. 3-110. The dislodged-in-shipping inner shell of this assembly (a) is repaired by carefully removing the outer shell before retrieving and remounting the inner shell (b) and then re-gluing the outer shell to its beryllium platform (c).

including those repaired, survived their shipment to Rochester and were ready to be shot on arrival.

Another type of double shell target that GA onsite microassembly support group aided in producing presented a different type of difficulty. Unlike the shell-within-a-shell direct drive type of target described just above, the latest series of indirect drive double-shell targets required a pre-assembled shell to be placed at the plane of the seam of the hohlraum such that the seam of the nearly opaque capsule was oriented in a certain way, for example, a diagnostic hole machined into the body of the hohlraum. The capsule was held centered at the level of the hohlraum between two layers of formvar in much the same way as is the single shell pictured in Fig. 3–111, which illustrates the discussion of a different type of target. It had been decided on the basis of negative results from previous experiments that the method of creating a double shell by gluing hemishells around a smaller shell could never be consistently done with the required precision to work well in an indirect drive setting. A great deal of LLNL time, expense, and manpower was then lavished over many months in a successful effort to produce about a half dozen of these now very valuable double-shells. The difficulty for the assembler lay not so much in meeting the assembly specifications for the target, which were not overly difficult, but rather in being aware that the targets were virtually irreplaceable, at least in regard to being ready anywhere near the experimenter’s timeframe. The LLNL machinist who described the fabrication of this capsule in a talk during the latest Target Fabrication Conference related how fixturing had been put in place such that the capsule in progress would be under the total physical control of the machinist at all times so as to negate, for all practical purposes, the possibility of losing it. No such fixturing had been put in place for the use of the microassembler during the tenting and placing into the hohlraum of these precious objects! While not many capsules have been lost or damaged during these processes, enough have been that the assembler could not but have fearful visions of the capsule trampolining into space off a taut plane of formvar film or pinging sideways into the unknown as attempts were being made to roll it slowly off a vacuum chuck or nudge it gently into its specified orientation. Fortunately, none of these mishaps occurred, and the targets were delivered on schedule. Just recently, it has been learned that the results from these targets gave pause to those within the program who had felt skeptical as to whether the double-shell model deserved any further consideration to the point where some of these now feel there might now be some possibility that it could point to some experimentally successful paths.

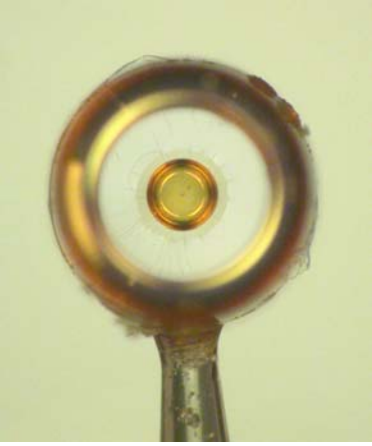

Fig. 3–111. The formvar-tented capsule at the center of the core-imaging target's split-case hohlraum (before addition of the LEH-facing pinhole array).

The "core-imaging" type of OMEGA target shown disassembled in Fig. 3–112 and assembled in two views in Fig. 3–113 can be thought of as exemplifying both the wide range of materials found in many of our targets and as another variant of the evolution of target types; specifically, how a single diagnostic element in an earlier version of a target tends to be "doubled" in later versions. The disassembled view exhibits components containing elements and materials ranging from argon to zinc. These include a germanium-doped PVA-GDP capsule enclosing a 0.05 atm of argon, two hohlraum halves machined from epoxy and coated with 2 μm of gold, support wires of copper, plastic shields doped with lead, two pinhole arrays in parylene-coated tantalum substrates, and a detecting disk made of zinc. The core of the assembled target consists of the capsule suspended at the plane of the center seam between the two halves of the split-case hohlraum by two thin layers of formvar film (Fig. 3–111). To capture the desired multiplicity of images of the capsule imploding during the target shot, two identical arrays of 61, 5-μm diameter pinholes in an 850 μm square tantalum substrate are placed such that one is paired with a diagnostic looking at the capsule directly through one of the LEHs, the other with a diagnostic observing the central seam area from the side of the hohlraum. For the LEH-facing array, the geometry of the chamber dictated that its optimum orientation would be to be rotated 36 deg clockwise in relation to the mounting stalk. This array directly faced an LEH which necessitated machining semi-circles out of the plastic holder along the perimeter so that it would not be hit by incoming beams (Fig. 3–114). The diameter and positioning of the array's support wire were determined by similar beam-avoiding considerations. As might be guessed, this target's embodying a "diagnostic-doubling" evolution stems from the fact that its design in the earliest series in which it appeared included only the LEH-facing array. The second, side-facing array has appeared only in later campaigns. Since avoiding incoming beams is not an issue for this second array, which is out of the line of fire, it can be supported by a simpler, rectangular holder and the precise placement of the support wire is not crucial. Still, the fact that the array needs to be rotated precisely in regard to the stalk (28.3 deg counterclockwise) and tilted towards the hohlraum at a difficult to measure 1.7 deg, ensures that the addition of this element adds a degree of difficulty to the target's assembly that is not insignificant.

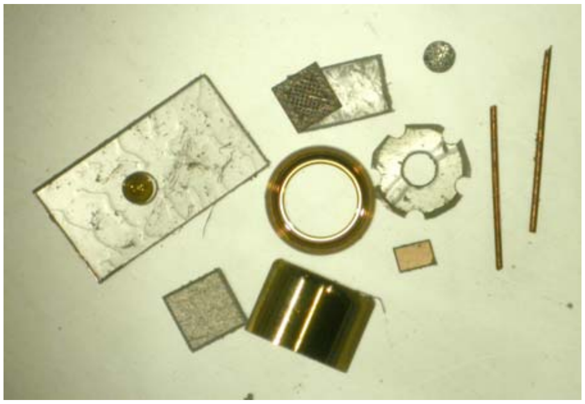

Fig. 3–112. The disassembled components of a "core-imaging" target display a considerable variety of shapes and materials.

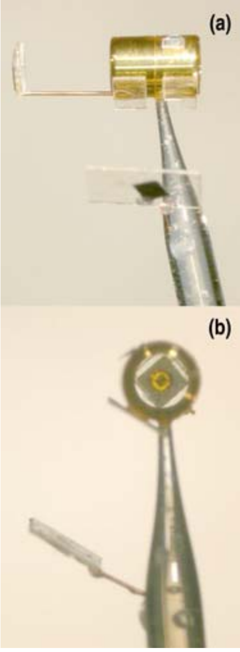

Fig. 3–113. (a) The counterclockwise rotation of the pinhole array with an LEH view, as well as a miniature image of the same array appearing in the fuel capsule, can be seen through the opposite LEH of this core-imaging target. (b) In this view, the side-viewing pinhole array can be seen attached at a certain rotation to its rectangular holder which is in turn glued to the target stalk at a slight tilt towards the hohlraum. The zinc detector disc named in the disassembled view can be seen at the far edge of the hohlraum, partially covered by a plastic shield.

The little "top hat" type target shown at the upper right of the size comparison in Fig. 3–108 is part of a series that has seen constant variations in size and thickness of the hohlraums since it was introduced in 2000, but, in this instance, what has evolved has been the experimenters' requests for greater stringency in certain specifications for their targets as their understanding of what their diagnostics require has become more refined. What has become less and less acceptable is any denting of the hohlraum or deviation from flatness on its top surface. The dimensions and thicknesses of these gold hohlraums range from 800 × 880 μm to 400 × 400 μm and from 25 to 3 μm, respectively. As might be expected, the smallest and thinnest of these are the most susceptible to being damaged in handling. During the etching and assembling process, they can be dented simply by being held by a vacuum chuck with too strong an intake or by having any wedging pressure exerted against them as might be caused by trapping them against the inside of a storage bottle from which one might be trying to remove them. For positioning or moving these smallest, thinnest hohlraums, very fine-tipped brushes with soft bristles have become the rule, with only the smallest diameter vacuum chucks at weakest power being used when absolutely necessary. Figure 3–115 shows a reject, whose top was dented by trying to push it up from within through the inner diameter of the plastic washer. The target shown in two views in Fig. 3–116 is the most recently made in this series, incorporating a 400 × 400 μm gold hohlraum having a 3 μm thick wall and an acceptable level of flatness.

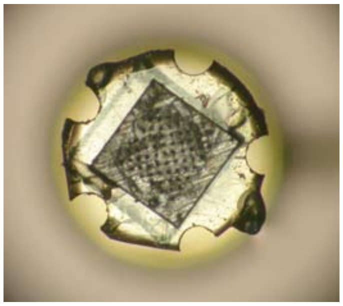

Fig. 3–114. A reverse-scalloping border has been machined into the LEH pinhole array's plastic holder to provide an unobstructed path for laser beams into the LEH below.

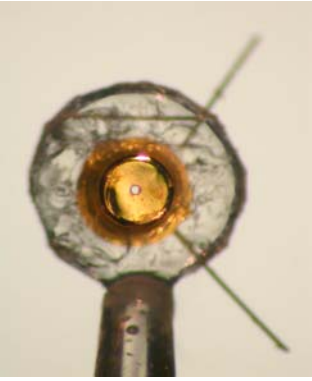

Fig. 3–115. A "hot hohlraum" target rejected for the dent in its top surface.

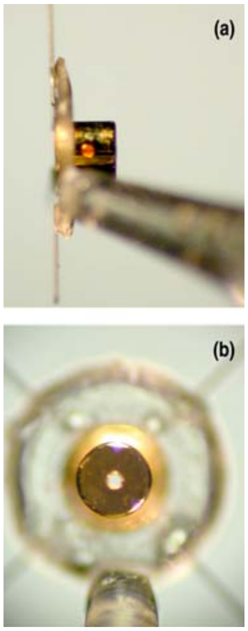

Fig. 3–116. A side and a top view of the most recent target produced for the hot hohlraum series incorporating a hohlraum with a 400 μm length and diameter and a 3 μm wall thickness.

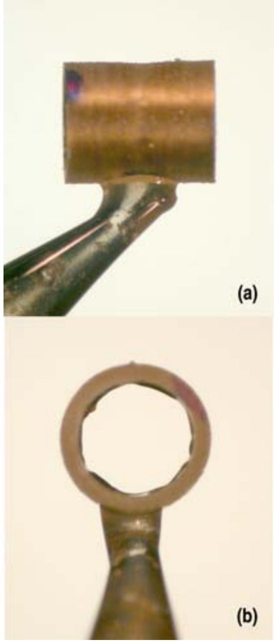

Fig. 3–117. Top and side views of a plastic hohlraum with an inner uranium coating.

An instance of how variations in materials can affect target assembly can be briefly noted in the plastic hohlraum with an interior coating of uranium shown in Fig. 3–117. While the production of plastic hohlraums with an interior coating of gold has become routine, certain types of uranium deposition produce highly stressed coatings which can cause flaking and rippling in the coating on the inside plastic surface. The machining and etching processes required to produce hohlraums then become very delicate, chancy, and often frustrating operations. When a hohlraum emerges that is acceptable for inclusion into a design such as the fairly simple one shown here, the target assembler is often faced with the task of having to trim off the sections of the stressed coating which have extruded beyond the hohlraum's LEHs (so that the end-capping gold washers can be laid on flat and without gaps) while avoiding generating cracks or flaking that could easily lead to areas inside the hohlraum being stripped of uranium.

Finally, while most of the targets to date have been fairly conventional in shape, Fig. 3–118 shows two views of a jet target that incorporates an unusually shaped conical parylene-coated copper shield that has grown so disproportionately large (over a centimeter in diameter) that an assembly complication was added to its design that had nothing to do with gathering data. To allay the fears at OMEGA over what havoc this shield might wreak in the target chamber if allowed to fly free at shot time, a "leash" of copper wire was threaded through a hole drilled near the shield's outer edge. The other end of the leash was glued to the target base. This was meant to keep the shield safely tethered to the base during and after the experimental shot. During the assembly process, due in part, probably, to the shield's parylene coating resisting the formation of a strong glue bond, bitter experience showed that a slight torquing of the not-so-flexible leash, as it was being threaded, could easily snap the shield, and the rest of the target with it, right off the target stalk.

At any rate, the members of the on-site GA-Schafer target support team at LLNL, in league with their lab counterparts, stand ready and eager to meet whatever challenges are presented by the evolutions of material, size, thickness, design, or stringency of specification as they occur in the fabrication of the ICF targets of the future.

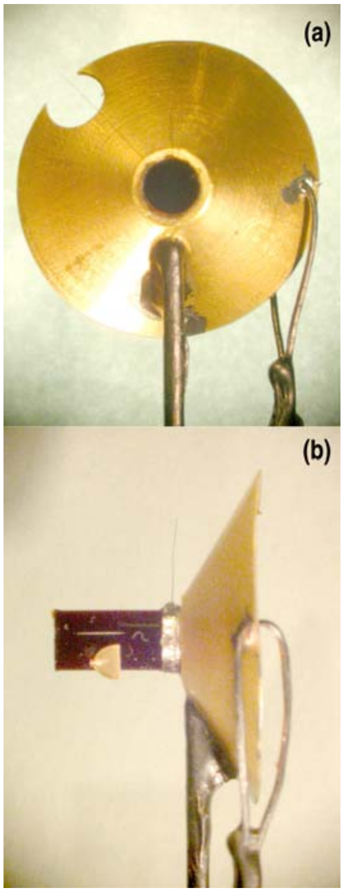

Fig. 3–118. Top and side views of foam-jet target showing copper leash attached to conical copper shield to hold it in place during and after target shot.

4. PUBLICATIONS

Items with GA/Schafer efforts supported by the contract for Target Component Fabrication and Technology Development Support are marked with an asterisk.

4.1. LIST OF PUBLICATIONS

Bittner, D., “Inertial Fusion Technology, Highlights: Redistribution Times of IR-Heated DT Layers,” General Atomics Report GA–A23813 (2003).

Brown, L.C., “High Efficiency Generation of Hydrogen Fuels Using Nuclear Power, Final Report for the Period August 1, 1999 through September 30, 2002,” General Atomics Report GA–A24285 (2003).

Brown, L.C., G.E. Besenbruch, K.R. Schultz, S.K. Showalter, A.C. Marshall, P.S. Pickard, J.F. Funk, “High Efficiency Generation of Hydrogen Fuels Using Thermochemical Cycles and Nuclear Power,” Proc. 2002 Spring Meeting of the American Institute of Chemical Engineers, March 10–14, 2002, New Orleans, Louisiana; General Atomics Report GA–A24326 (2002).

Brown, L.C., R.D. Lentsch, G.E. Besenbruch, K.R. Schultz, J.E. Funk, “Alternative Flowsheets for the Sulfur-Iodine Thermochemical Hydrogen Cycle,” Proc. 2003 Spring National Meeting of AlChE, New Orleans, Louisiana, March 30 through April 3, 2003; General Atomics Report GA–A24266 (2003).

Cowan, T.E., R. Stephens, P. Parks, M. Rosenbluth, Y. Omelchenko, J. Dahlburg, M.D. Perry, and E.M. Campbell, “Fast Ignition and Ultra-intense Laser Research at General Atomics,” 2nd Int. Conf. on Inertial Fusion Science and Applications, September 9–14, 2001, Kyoto, Japan, to be published in Fusion Technology.

Giraldez, E., and J.L. Kaae, “Fabrication of Window Saddles for NIF Cryogenic Hohlraums,” presented at the 15th Target Fabrication Specialists Meeting, June 1–5, 2003, Gleneden Beach, Oregon, to be published in Fusion Sci. Technol.; General Atomics Report GA–A24505 (2003).

Goodin, D.T., N.B. Alexander, G.E. Besenbruch, L.C. Brown, A. Nobile, R.W. Petzoldt, W.S. Rickman, D. Schroen, B. Vermillion, “Demonstrating a Cost-Effective Target Supply for Inertial Fusion Energy,” Proc. 15th Top. Mtg. on the Technology of Fusion Energy, Washington, DC, 2002, to be published in Fusion Sci. Technol.; General Atomics Report GA–A24199 (2002).

Goodin, D.T., A. Nobile, N.B. Alexander, L.C. Brown, J.L. Maxwell, J. Pulsifer, A.M. Schwendt, M.S. Tillack, R.S. Willms, “A Credible Pathway for Heavy Ion Driven Target Fabrication and Injection,” Proc. 14th Int. Symp. on Heavy Ion Inertial Fusion, May 26–32, 2002, Moscow, Russia, in Laser and Particle Beams **20**, 515 (2002); General Atomics Report GA–A23969 (2002).

Goodin, D.T., A. Nobile, D.G. Schroen, J.L. Maxwell, and W.S. Rickman, “Cost-Effective Target Fabrication for Inertial Fusion Energy,” presented at the 3rd Int. Conf. on Inertial Fusion Sciences and Applications, September 7–12, 2003, Monterey, California, to be published in Fusion Sci. Technol.; General Atomics Report GA–A24429 (2003).

Goodin, D.T., A. Nobile, J. Hoffer, A. Nikroo, G.E. Besenbruch, L.C. Brown, J.L. Maxwell, W.R. Meier, T. Norimatsu, J. Pulsifer, W.S. Rickman, W. Steckle, E.H. Stephens, M. Tilack, “Addressing the Issues of Target Fabrication and Injection for Inertial Fusion Energy,” Fusion Engin. Design **69**, 803 (2003); General Atomics Report GA–A24086 (2002).

Hill, D.W., E. Castillo, K.C. Chen, S.E. Grant, A.L. Greenwood, J.L. Kaae, A. Nikroo, S.P. Paguio, C. Shearer, J.N, Smith, Jr., R.B. Stephens, D.A. Steinman, J. Wall, “Fabrication and Characterization of Fast Ignition Targets,” presented at the 15th Target Fabrication Specialists Meeting, June 1–5, 2003, Gleneden Beach, Oregon, to be published in Fusion Sci. Technol.; General Atomics Report GA–A24443 (2003).

Huang, H., R.B. Stephens, D.W. Hill, C. Lyon, A. Nikroo, D.A. Steinman, “Automated Batch Characterization of ICF Shells with Vision-Enabled Optical Microscope System,” presented at the 15th Target Fabrication Specialists Meeting, June 1–5, 2003, Gleneden Beach, Oregon, to be published in Fusion Sci. Technol.; General Atomics Report GA–A24442 (2003).

Meier, W.R., B.G. Logan, W.L. Waldron, G-L. Sabbi, D.A. Callahan-Miller, P.F. Peterson, D.T. Goodin, “Progress Toward Heavy Ion IFE,” Proc. 6th Int. Symp. on Fusion Nucl. Technology, April 7–12, 2002, San Diego, California, to be published in Fusion Engin. Design.

Nikroo, A., D. Czechowicz, R. Paguio, A.L. Greenwood, M. Takagi, “Fabrication and Properties of Overcoated Resorcinol-Formaldehyde Shells for OMEGA Experiments,” presented at the 15th Target Fabrication Specialists Meeting, June 1–5, 2003, Gleneden Beach, Oregon, to be published in Fusion Sci. Technol.; General Atomics Report GA–A24451 (2003).

Nikroo, A., E. Castillo, D.W. Hill, A.L. Greenwood, “Preparation of Cu-Doped Glow Discharge Polymer Coatings for ICF Applications,” presented at the 15th Target Fabrication Specialists Meeting, June 1–5, 2003, Gleneden Beach, Oregon, to be published in Fusion Sci. Technol.; General Atomics Report GA–A24453 (2003).

Nikroo, A., D. Czechowicz, K.C. Chen, M. Dicken, C. Morris, R. Andrews, A.L. Greenwood, E. Castillo, "Mechanical Properties of Thin GDP Shells Used as Cryogenic Direct Drive Targets at OMEGA," presented at the 15th Target Fabrication Specialists Meeting, June 1–5, 2003, Gleneden Beach, Oregon, to be published in Fusion Sci. Technol.; General Atomics Report GA–A24457 (2003).

Nikroo, A., W. Baugh, and D.A. Steinman, "Fabrication of Gas-Filled Tungsten-Coated Glass Shells," presented at the 15th Target Fabrication Specialists Meeting, June 1–5, 2003, Gleneden Beach, Oregon, to be published in Fusion Sci. Technol.; General Atomics Report GA–A24458 (2003).

Nikroo, A., J. Bousquet, R. Cook, B.W. McQuillan, R. Paguio, M. Takagi, "Progress in 2 mm Glow Discharge Polymer Mandrel Development for NIF," presented at the 15th Target Fabrication Specialists Meeting, June 1–5, 2003, Gleneden Beach, Oregon, to be published in Fusion Sci. Technol.; General Atomics Report GA–A24483 (2003).

Olson, R.E., R.J. Leeper, S.C. Dropinski, L.P. Mix, G.A. Rochau, S.H. Glenzer, O.S. Jones, L.J. Suter, J.L. Kaae, C.H. Shearer, J.N. Smith, "Time and Spatially Resolved Measurements of X-ray Burnthrough and Re-emission in Au and Au:Dy:Nd Foils," submitted to 14th Top. Conf. on High Temperature Plasma Diagnostics, July 8, 2002, Madison, Wisconsin.

Petzoldt, R.W., N.B. Alexander, T.J. Drake, D.T. Goodin, K. Jonestrack, B.A. Vermillion, "Experimental Target Injection and Tracking System Construction and Single Shot Testing," presented at the 3rd Int. Conf. on Inertial Fusion Sciences and Applications, September 7–12, 2003, Monterey, California, and to be published in Fusion Sci. Technol.; General Atomics Report GA–A24432 (2003).

Project Staff, "Target Fabrication and Characterization Development in Support of NRL Laser-Plasma Program Annual Report to the U.S. Department of Navy, January 14, 2002 through March 5, 2003," General Atomics Report GA–A24421 (2003).

Project Staff, "Target Injection and Tracking Development in Support of NRL Laser-Plasma Program Annual Report to the U.S. Department of Navy, January 14, 2002 through March 5, 2003," General Atomics Report GA–A24369 (2003).

Rickman, W.S., D.T. Goodin, "Cost Modeling for Fabrication of IFE Targets," Proc. 2nd IAEA Tech. Mtg on Phys. and Tech. of Inertial Fusion Energy Targets and Chambers, San Diego, California, 2002, to be published in Fusion Sci. Technol.; General Atomics Report GA–A24074 (2002).

Schultz, K.R., "Use of the Modular Helium Reactor for Hydrogen Production," 2003 World Nuclear Association Symposium, September 3–5, 2003, London, United Kingdom, CD-ROM; General Atomics Report GA–A24428 (2003).

Steinman, D.A., R. Wallace, S.E. Grant, M.L. Hoppe, J.N. Smith, Jr., "Fabrication of a New Type of Double-Shell Target Having a PVA Inner Layer," presented at the 15th Target Fabrication Specialists Meeting, June 1–5, 2003, Gleneden Beach, Oregon, to be published in Fusion Sci. Technol.; General Atomics Report GA–A24455 (2003).

Stephens, E.H., A. Nikroo, D.T. Goodin, R.W. Petzoldt, "Optimizing High Z Coatings for IFE Shells," Proc. 2nd IAEA Tech. Mtg. on Physics and Technology of Inertial Fusion Energy Targets and Chambers, San Diego, California, 2002, to be published in Fusion Sci. Technol.; General Atomics Report GA–A24057 (2002).

Stephens, R.B., "Implosion of Indirectly Driven Reentrant Cone Shell Target," submitted to Phys. Rev. Lett.; General Atomics Report GA–A24244 (2003).

Stephens, R.B., Y. Aglitskiy, C. Andersen, T.E. Cowan, R.R. Freeman, S.P. Hatchett, J.M. Hill, M.H. Key, J.A. King, J.A. Koch, A.J. MacKinnon, R.A. Snavely, "K_α Fluorescence Examination of Relativistic Electron Transport in the Context of Fast Ignition," submitted to Phys. Rev. Lett.; General Atomics Report GA–A24116 (2002).

Stephens, R.B., D. Olson, H. Huang, J.B. Gibson, "Complete Surface Mapping of ICF Shells," presented at the 15th Target Fabrication Specialists Meeting, June 1–5, 2003, Gleneden Beach, Oregon, to be published in Fusion Sci. Technol.; General Atomics Report GA–A24452 (2003).

Stephens, R.B., S.P. Hatchett, R. Turner, "Cone Dynamics in Fast Ignitor Cone Targets on OMEGA," Bull. Am. Phys. Soc. **48**, 298 (2003) abstract.

*Streit, J.E., D.G. Schroen, "Development of Divinylbenzene Shells for Use as Inertial Confinement Fusion Targets," submitted to Fusion Technol.

Vermillion, B.A., G.E. Besenbruch, L.C. Brown, D.T. Goodin, B.W. McQuillan, M. Takagi, "Microencapsulated Studies for Mass Production of IFE Targets," presented at the 3rd Int. Conf. on Inertial Fusion Sciences and Applications, September 7–12, 2003, Monterey, California, to be published in Fusion Sci. Technol.; General Atomics Report GA–A24431 (2003).

5. ACKNOWLEDGMENT

This report of work was prepared for the U.S. Department of Energy under Contract No. DE-AC03-01SF22260.